Equilibrium and stability properties of intense non-neutral electron flow

Ronald C. Davidson,* Hei-Wai Chan, Chiping Chen, and Steven Lund

Plasma Fusion Center, Massachusetts Institute of Technology, Cambridge, Massachusetts 02139

Non-neutral plasmas, like electrically neutral plasmas, exhibit a broad range of collective properties, such as plasma waves and instabilities, and the ability to support long-lived, large-amplitude coherent structures. This paper reviews the equilibrium and stability properties of intense non-neutral electron flow in crossed electric and magnetic fields. Following a description of equilibrium properties for magnetically insulated electron flow in planar geometry, extraordinary-mode stability properties are investigated for relativistic non-neutral electron flow between planar conductors. Particular emphasis is placed on the magnetron and diocotron instabilities, and detailed stability behavior is shown to exhibit a sensitive dependence on the self field intensity (as measured by the dimensionless parameter $s_e=\gamma_e^0\omega_{pe}^2/\omega_{ce}^2$) as well as on the shape of the equilibrium profiles. The influence of cylindrical effects (such as the centrifugal and Coriolis accelerations of an electron fluid element) on stability behavior is then investigated for rotating electron flow in cylindrical geometry. Finally, the properties of large-amplitude coherent structures in non-neutral plasmas with circulating electron flow are investigated. Topics covered in this area include particle-in-cell computer simulations of dense ($s_e\sim 1$) electron flow in relativistic magnetrons which show large-amplitude spoke formation in the circulating electron density, and application of a cold-fluid guiding-center model to investigate large-amplitude vortex structures in low-density ($s_e\ll 1$) non-neutral plasma. The accessibility and stability of such stationary structures (in the rotating frame) remain important topics for future investigation.

CONTENTS

I. INTRODUCTION

A non-neutral plasma is a many-body collection of charged particles in which there is no overall charge neutrality (Davidson, 1974, 1990). Such systems are characterized by intense self-electric fields, and, in high-current configurations, by intense self-magnetic fields. Non-neutral plasmas, like electrically neutral plasmas, exhibit a broad range of collective properties, such as plasma waves, instabilities, and Debye shielding. Moreover, the intense self fields in a non-neutral plasma can have a large influence on detailed plasma behavior and stability properties.

Since the early 1970s, interest in the physics of non-neutral plasmas has grown substantially in such diverse areas as investigations of basic equilibrium, stability, and transport properties (Roberson and Driscoll, 1988, and papers therein; Davidson, 1990); high-current electron induction accelerators (Kapetanakos and Sprangle, 1985; Humphries, 1986) and alternating-gradient accelerators (Keefe, 1987; Lawson, 1988); phase transitions in strongly coupled, two- and three-dimensional non-neutral plasmas (Malmberg and O'Neil, 1977; Grimes and Adams, 1979; Dubin and O'Neil, 1988; Gilbert, Bollinger, and Wineland, 1988); coherent electromagnetic wave generation by free electrons interacting with applied magnetic field structures (Marshall, 1985; Granatstein and Alexeff, 1987, and references therein; Roberson and Sprangle, 1989); astrophysical studies of large-scale isolated non-neutral plasma regions in the magnetospheres of rotating, magnetized neutron stars (Michael, 1985); and the development of positron (Surko *et al.*, 1986) and antiproton (Gabrielse *et al.*, 1986) ion sources. In addition to developing a basic physics understanding of many-body charged-particle systems in which there is no overall charge neutrality, there are many practical applications of non-neutral plasmas. These include coherent electromagnetic wave generation by intense electron beams, as in free-electron lasers (Marshall, 1985; Roberson and Sprangle, 1989), magnetrons, and cyclotron masers (Granatstein and Alexeff, 1987, and references therein); the development of advanced accelerator concepts (Ka-

*Permanent address: Plasma Physics Laboratory, Princeton University, Princeton, New Jersey 08543.

petanakos and Sprangle, 1985; Humphries, 1986), including high-current accelerators such as the modified betatron (Sprangle and Kapetanakos, 1978; Rostoker, 1980; Petillo and Davidson, 1987), and periodic focusing accelerators for heavy ions (Keefe, 1987; Lee and Hovingh, 1989); the equilibrium and stability of intense non-neutral electron and ion flow in high-voltage diodes (Antonsen and Ott, 1976; Miller, 1982; Desjarlais, 1987, 1989), with applications that include particle beam fusion (Miller, 1982; VanDevender and Cook, 1986), to mention a few examples.

The very early research on non-neutral plasma predated, by many decades, the common usage of the terms "plasma" or "non-neutral plasma" in the lexicon of modern-day physics. [The term "plasma" was introduced by Tonks and Langmuir (1929) to describe collective electron plasma oscillations in an ionized gas, although widespread use of this descriptor did not occur until the 1960s.] Indeed, the classic papers by Child (1911), Langmuir (1923), Lewellyn (1941), Brillouin (1945), MacFarlane and Hay (1950), Pierce (1956), Kyhl and Webster (1956), and Buneman (1957) represent some of the earliest efforts to investigate theoretically and experimentally the equilibrium and stability properties of non-neutral electron flow in planar diodes and in geometries with crossed electric and magnetic fields. This and other early research on non-neutral plasmas predated the major international development of the theoretical foundations of modern plasma physics, which occurred to a large extent during the 1960s. Moreover, advances in the understanding of non-neutral plasmas during this early period appear to have proceeded largely uninfluenced by the seminal works of Vlasov (1945), Landau (1946), and Bogoliubov (1946) on collective interactions in many-body charged-particle systems. This is due, in part, to the fact that the emphasis during this early period was mainly on the practical use and control of space-charge waves on non-neutral electron beams in microwave generation devices (such as klystrons, traveling-wave tubes, and magnetrons) and vacuum tube diodes. Excellent accounts of the early work on microwave devices and vacuum tube diodes are given by Slater (1969), Okress (1961), and Birdsall and Bridges (1966).

With the advent of modern plasma theory and improved instrumentation techniques in the late 1960s and early 1970s, our understanding of the fundamental properties of non-neutral plasmas received new impetus. Basic theoretical and experimental studies of one-component pure electron plasmas showed that many of the equilibrium, stability, and collective oscillation properties of non-neutral plasmas (Davidson and Krall, 1969, 1970; Trivelpiece, 1972), including Debye shielding (Davidson, 1971), are directly analogous to the collective properties of electrically neutral plasmas, appropriately modified by equilibrium self-field effects due to the space charge. In addition, rapid advances in pulsed power technology during this period, and the improved ability to produce and accelerate high-current electron beams (Hammer and Rostoker, 1970), led to increased research on non-neutral plasmas in several of the diverse areas enumerated in this section.

An extensive treatment of the basic equilibrium and stability properties and several applications of non-neutral plasmas is presented in *Physics of Nonneutral Plasmas* (Davidson, 1990). The present article has a considerably narrower focus. In particular, we review here the equilibrium and linear stability properties of intense non-neutral electron flow in crossed electric and magnetic fields (Secs. II–IV) and examine the properties of large-amplitude coherent structures in non-neutral plasmas with circulating electron flow (Secs. V and VI).

Typical crossed-field configurations are illustrated in Fig. 1 (planar geometry) and Fig. 15 (cylindrical geometry) below. Here, $B_z(x)\hat{\mathbf{e}}_z$ is the total equilibrium magnetic field (externally applied magnetic field plus self-magnetic field produced by the electron current $-en_e^0 V_{ye}^0)(x)\hat{\mathbf{e}}_y$, and $E_x(x)\hat{\mathbf{e}}_x$ is the equilibrium electric field produced by the electron space charge, $-en_e^0(x)$, as well as any externally applied potentials on the parallel conductors located at $x=0$ and $x=d$ in Fig. 1. These conductors are labeled, respectively, as the cathode ($x=0$), which emits electrons, and the anode ($x=d$), which is maintained at potential V relative to the cathode. (Similarly, in Fig. 15, the cathode and anode are located at $r=a$ and $r=b$, respectively.) It should be emphasized, however, that the equilibrium and stability analysis presented in Secs. II–IV applies equally well if the non-neutral electron plasma is created externally and then introduced (e.g., injected) into the region between the conductors in Fig. 1 (or Fig. 15). Indeed, the details of the formation of the non-neutral electron plasma are not treated in Secs. II–IV. Rather, the analysis in Secs. II–IV makes use of a macroscopic model based on the cold-fluid–Maxwell equations to investigate detailed equilibrium and stability behavior for extraordinary-mode flute perturbations ($\partial/\partial z=0$) about a *preformed* non-neutral electron plasma with equilibrium density profile $n_e^0(x)$ and relativistic flow velocity $V_{ye}^0(x)\hat{\mathbf{e}}_y$ in planar geometry (Fig. 1), or with equilibrium density profile

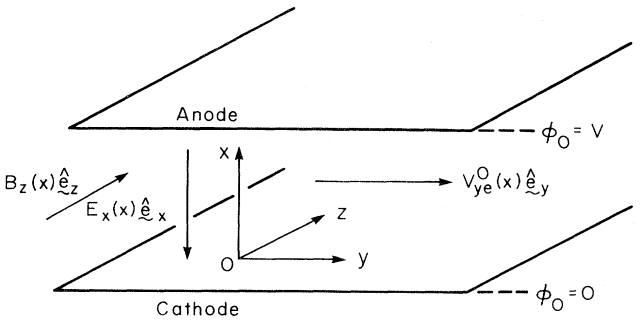

FIG. 1. Planar electron flow in the crossed electric and magnetic fields $E_x(x)\hat{\mathbf{e}}_x$ and $B_z(x)\hat{\mathbf{e}}_z$. Here, $V_{ye}^0(x) = -cE_x(x)/B_z(x)$ is the average flow velocity, and the cathode and anode are assumed to be perfect conductors maintained at a potential difference V.

$n_e^0(r)$ and azimuthal flow velocity $V_{\theta e}^0(r)\hat{\mathbf{e}}_\theta$ in cylindrical geometry (Fig. 15). The main boundary condition assumed regarding the equilibrium fluid motion corresponds to space-charge-limited flow (see, for example, Miller, 1982). Specifically, under quasi-steady-state conditions, it is assumed that the normal electric field at the cathode surface is equal to zero; i.e., $E_x(x=0)$ for the case of planar flow (Fig. 1), and $E_r(r=a)=0$ for the case of cylindrical flow (Fig. 15).

Referring to Fig. 1, macroscopic force balance on a cold-fluid element in planar geometry shows that the equilibrium flow velocity is $V_{ye}^0(x)=-cE_x(x)/B_z(x)$ in the region where the electron density $n_e^0(x)$ is nonzero. Denoting the relativistic mass factor by $\gamma_e^0(x)=[1-V_{ye}^{02}(x)/c^2]^{-1/2}$, it is convenient to introduce the quantity $s_e(x)$ defined by

$$s_e(x)=\frac{4\pi n_e^0(x)e^2/\gamma_e^0(x)m_e}{e^2B_z^2(x)/\gamma_e^{02}(x)m_e^2c^2}=\frac{\gamma_e^0(x)\omega_{pe}^2(x)}{\omega_{ce}^2(x)}\ , \tag{1.1}$$

which is a measure of the strength of the self-electric field produced by the electron space charge. Here, $\omega_{pe}^2(x)=4\pi n_e^0(x)e^2/m_e$ is the nonrelativistic electron plasma frequency-squared, and $\omega_{ce}(x)=eB_z(x)/m_ec$ is the nonrelativistic electron cyclotron frequency. Note that $s_e(x)$ is directly proportional to the electron density $n_e^0(x)$ and inversely proportional to $B_z^2(x)$. Therefore $s_e(x)$ is a dimensionless measure of the ratio of the (defocusing) force associated with the self-electric field to the (focusing) force associated with the confining magnetic field. A similar definition of the self-field parameter pertains in cylindrical geometry, with $s_e(r)=\gamma_e^0(r)\omega_{pe}^2(r)/\omega_{ce}^2(r)$ and $\gamma_e^0(r)=[1-V_{\theta e}^{02}(r)/c^2]^{-1/2}$. Not surprisingly, it is found (Secs. II–IV) that the equilibrium and linear stability properties of non-neutral electron flow exhibit a sensitive dependence on the self-field intensity as measured by s_e, as well as on the detailed shape of the equilibrium profiles for n_e^0, γ_e^0, etc.

A second important focus of the present article pertains to large-amplitude coherent structures in non-neutral plasmas with circulating electron flow (Secs. V and VI). In this regard, the formation and evolution of large-amplitude coherent structures play an important role in describing the nonlinear dynamics of non-neutral plasmas. This is true in systems ranging from low-density ($s_e \ll 1$) rotating non-neutral plasmas initially subject to the diocotron instability, to high-density ($s_e \sim 1$) circulating non-neutral electron layers in conventional and relativistic magnetrons. Use is made of a cold-fluid guiding-center model to investigate the properties of rotating, two-dimensional large-amplitude vortex structures in a low-density non-neutral plasma column (Sec. VI). In addition, particle-in-cell computer simulations are presented which describe the nonlinear evolution of a high-density non-neutral electron layer in a relativistic cylindrical magnetron, including the formation of a large-amplitude "spoke" structure in the circulating electron density (Sec. V).

To further orient the reader, it is convenient to provide additional background information. The study of intense non-neutral electron flow began with the classic works of Child (1911) and Langmuir (1923), who examined the steady flow of electrons between two parallel planar conductors in the absence of an applied magnetic field, treating one conductor as the cathode (which emits electrons) and the second conductor as the anode (maintained at a voltage V relative to the cathode). Investigations of the equilibrium and stability properties of non-neutral electron flow in such "conventional" diodes [with $B_z(x)=0$ in Fig. 1] have continued for more than three-quarters of a century. Areas of study have ranged from nonrelativistic electron flow at low voltages (Lewellyn, 1941; Birdsall and Bridges, 1966), to relativistic electron flow at high voltages (Jory and Trivelpiece, 1969), to analytical and numerical investigations of detailed stability behavior using both macroscopic (Antonsen *et al.*, 1984) and kinetic (Antonsen and Chang, 1989) models.

As indicated earlier, an important emphasis in this review article is on the equilibrium and stability properties of intense non-neutral electron flow in crossed electric and magnetic fields. Early work in this area was motivated in large part by the use of crossed-field electron devices such as magnetrons to generate coherent microwave radiation (Collins, 1948; Brillouin, 1951; Okress, 1961; Slater, 1969). Following Brillouin's classic paper (1945) on magnetically focused electron flow at high electron density ($s_e=1$), it was realized that low-density ($s_e \ll 1$) non-neutral electron layers with shear in the flow velocity are also subject to instability (the so-called diocotron or slipping-stream instability). The early treatments of the diocotron instability in planar geometry by MacFarlane and Hay (1950) and Buneman (1957) were followed by theoretical investigations of equilibrium and stability behavior in cylindrical geometry (Levy, 1965; Daugherty and Levy, 1967; Levy, 1968a, 1968b; Briggs, Daugherty, and Levy, 1970; Davidson and Tsang, 1984), investigations of quasilinear stabilization of the diocotron instability for multimode excitation (Davidson, 1985a), and inclusion of the (stabilizing) influence of relativistic and electromagnetic effects (Davidson, Tsang, and Uhm, 1988). In experimental investigations of the diocotron instability, one of the most ubiquitous properties of low-density non-neutral plasma initially subject to the diocotron instability is the development of long-lived, rotating vortex structures during the nonlinear evolution of the system (Prasad and Malmberg, 1986; Davidson *et al.*, 1990). This has been observed experimentally in annular electron layers (Kyhl and Webster, 1956; Pierce, 1956), in intense propagating annular electron beams (Kapetanakos *et al.*, 1973), in non-neutral plasma columns with a central conductor (Rosenthal, Dimonte, and Wong, 1987; Rosenthal and Wong, 1990) and without a central conductor (Malmberg *et al.*, 1988; Driscoll *et al.*, 1989; Fine, Driscoll, and Malmberg, 1989), and in computer simulation studies (Rosenthal and Wong, 1990).

For magnetically insulated electron flow in the planar

diode configuration illustrated in Fig. 1, the electrons are emitted from the cathode at $x=0$ and flow with average velocity $V_{ye}^0(x)=-cE_x(x)/B_z(x)$ parallel to the conductors at $x=0$ and $x=d$. For specified voltage V, provided the axial magnetic field $B_z(x)\hat{\mathbf{e}}_z$ is sufficiently strong, the outer edge of the electron layer will be insulated from contact with the anode at $x=d$ (Lovelace and Ott, 1974; Ott and Lovelace, 1975). Interest in the equilibrium and stability properties of magnetically insulated relativistic electron flow between parallel conductors received considerable impetus in the 1970s and 1980s. This was due in part to technological advances in the generation of intense relativistic electron beams by high-voltage diodes (see, for example, Miller, 1982 and Guenther and Kristiansen, 1987), the application of high-voltage diodes with magnetically insulated electron flow to generate high-power microwaves in relativistic magnetrons (Bekefi and Orzechowski, 1976; Orzechowski and Bekefi, 1979; Palevsky and Bekefi, 1979; Gleizer *et al.*, 1980; Benford, 1987; Nokonov *et al.*, 1987; Benford *et al.*, 1989), and the application of high-voltage diodes with magnetically insulated electron flow to generate intense ion beams originating from a thin plasma layer on the anode surface (Sudan and Lovelace, 1973; Humphries, Lee, and Sudan, 1974; Antonsen and Ott, 1976; Dreike *et al.*, 1976; Humphries *et al.*, 1976; Miller, 1982; Johnson *et al.*, 1983, 1985; Desjarlais, 1987, 1989). Early analyses of the magnetron instability for magnetically insulated electron flow between parallel conductors assumed nonrelativistic electron flow and validity of the electrostatic approximation (Buneman, Levy, and Linson, 1966). Stability behavior under Brillouin flow conditions with $s_e=\gamma_e^0\omega_{pe}^2/\omega_{ce}^2=1$ was examined at that time for the case of relativistic electron flow allowing for extraordinary-mode flute perturbations with $\partial/\partial z=0$ (Swegle and Ott, 1981a, 1981b; Swegle, 1983). Subsequently, extraordinary-mode stability properties were investigated for the general value of the self-field parameter s_e (Davidson, Tsang, and Swegle, 1984); the influence of the equilibrium profile shape on detailed stability behavior was examined (Davidson and Tsang, 1985); and stability properties for oblique propagation were investigated for electromagnetic perturbations with $\partial/\partial z\neq 0$ (Chang, Ott, and Antonsen, 1986).

Emphasis in Secs. II–IV of this review article is placed on the application of a macroscopic model based on the cold-fluid–Maxwell equations to investigate the equilibrium and stability properties of intense non-neutral electron flow in crossed electric and magnetic fields. It should be pointed out, however, that a kinetic model based on the Vlasov-Maxwell equations can also be used to investigate detailed equilibrium and stability behavior in circumstances where the momentum-space dependence (as well as the configuration-space dependence) of the equilibrium distribution function $f_b^0(\mathbf{x},\mathbf{p})$ plays an important role (Davidson, 1985b; Davidson and Uhm, 1985, 1989a, 1989b, Uhm and Davidson, 1985). Moreover, in high-power ion diodes with magnetically insulated electron flow, ion-driven instabilities that involve a coupling between the ion and electron components can also have a significant growth rates and can affect diode performance (Davidson, Tsang, and Uhm, 1985; Ott *et al.*, 1985; Chang, Chernin, *et al.*, 1986; Chang, Ott, and Antonsen, 1986).

The organization of this paper can be summarized briefly. Following a review of equilibrium properties for magnetically insulated electron flow in planar geometry (Sec. II), we investigate extraordinary-mode stability properties for relativistic non-neutral electron flow between planar conductors, placing particular emphasis on the magnetron and diocotron instabilities (Sec. III). The influence of cylindrical effects (such as the centrifugal and Coriolis accelerations of an electron fluid element) on stability behavior is then investigated for rotating electron flow in cylindrical geometry (Sec. IV). Finally, the properties of large-amplitude coherent structures in rotating non-neutral plasmas are investigated (Secs. V and VI). This includes particle-in-cell computer simulations of dense ($s_e\sim 1$) electron flow in relativistic magnetrons which shows large-amplitude spoke formation in the circulating electron density (Sec. V), and application of a cold-fluid guiding-center model to investigate large-amplitude vortex structures in low-density ($s_e\ll 1$) non-neutral plasma (Sec. VI).

II. EQUILIBRIUM PROPERTIES FOR PLANAR ELECTRON FLOW

A. Theoretical model and assumptions

For present purposes, we make use of a macroscopic cold-fluid model to describe intense non-neutral electron flow in the planar geometry illustrated in Figs. 1 and 2 (Davidson, Tsang, and Swegle, 1984; Davidson and Tsang, 1985; Davidson, 1990). Here, under steady-state conditions ($\partial/\partial t=0$), the electron motion occurs in the crossed electric and magnetic fields

$$\mathbf{E}^0(\mathbf{x})=E_x(x)\hat{\mathbf{e}}_x\ ,\qquad \mathbf{B}^0(\mathbf{x})=B_z(x)\hat{\mathbf{e}}_z\ . \tag{2.1}$$

The cathode (at $x=0$) and anode (at $x=d$) are assumed to be perfect conductors at a voltage difference V. Without loss of generality, the zero of potential is chosen such that

$$\phi_0(x=0)=0 \quad\text{and}\quad \phi_0(x=d)=V\ , \tag{2.2}$$

where $E_x(x)=-\partial\phi_0/\partial x$, and $\phi_0(x)$ is the electrostatic potential. In addition, space-charge-limit flow (Miller, 1982) is assumed with

$$E_x(x=0)=0\ , \tag{2.3}$$

which corresponds to zero normal electric field at the cathode.

For $\partial/\partial t=0$, the electron density profile in the anode-cathode region is denoted by $n_e^0(x)$, and the average flow

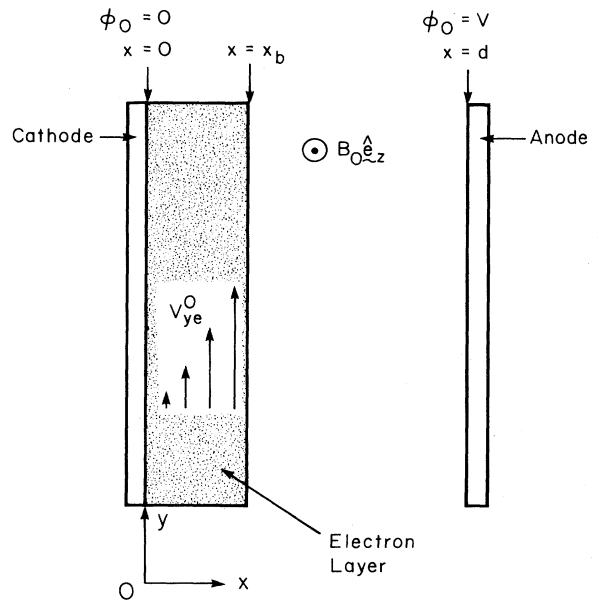

FIG. 2. Electron layer extends from $x=0$ to $x=x_b<d$, and $B_0\hat{\mathbf{e}}_z$ is the axial magnetic field in the vacuum region $(x_b<x\le d)$.

velocity of the electrons is $\mathbf{V}_e^0(\mathbf{x})=V_{ye}^0(x)\hat{\mathbf{e}}_y$. Treating the electrons as a cold fluid, it follows that equilibrium force balance on a fluid element in the x direction can be expressed as

$$0=-en_e^0(x)[E_x(x)+(1/c)V_{ye}^0(x)B_z(x)]\ , \tag{2.4}$$

where $-e$ is the electron charge and c is the speed of light *in vacuo*. Solving Eq. (2.4) in the region where the electron density is nonzero gives

$$V_{ye}^0(x)=-cE_x(x)/B_z(x)\ , \tag{2.5}$$

which corresponds to $\mathbf{E}^0\times\mathbf{B}^0$ flow in the crossed electric and magnetic fields. As illustrated in Fig. 2, the electron density profile $n_e^0(x)$ extends from $x=0$ to $x=x_b<d$, and the magnetic field in the vacuum region $(x_b<x\le d)$ is denoted by $B_0\hat{\mathbf{e}}_z$. For specified voltage V, a sufficiently strong magnetic field B_0 is required in order to ensure that the electron flow is insulated from contact with the anode $(x_b<d)$.

The equilibrium electric and magnetic fields, $E_x(x)$ and $B_z(x)$, are determined from the steady-state Maxwell equations

$$\frac{\partial}{\partial x}E_x(x)=-4\pi en_e^0(x) \tag{2.6}$$

and

$$\frac{\partial}{\partial x}B_z(x)=\frac{1}{c}4\pi en_e^0(x)V_{ye}^0(x)=-\frac{4\pi en_e^0(x)E_x(x)}{B_z(x)}\ . \tag{2.7}$$

Of course, Eqs. (2.6) and (2.7) are to be solved subject to the boundary conditions in Eqs. (2.2) and (2.3), as well as $B_z(x)=B_0=$const in the vacuum region $(x_b<x\le d)$. Equations (2.6) and (2.7) constitute two equations relating the three equilibrium profiles $E_x(x)$, $B_z(x)$, and $n_e^0(x)$. Therefore, generally speaking, there is considerable latitude in describing equilibrium properties within the framework of a macroscopic cold-fluid model (Davidson, Tsang, and Swegle, 1984; Davidson and Tsang, 1985; Davidson, 1990). For example, the functional form of the electron density profile $n_e^0(x)$ can be specified arbitrarily over the layer cross section, and the corresponding field profiles, $E_x(x)$ and $B_z(x)$, calculated self-consistently from Eqs. (2.6) and (2.7). Alternatively, Eqs. (2.6) and (2.7) can be solved subject to some additional constraint condition, and all of the equilibrium profiles calculated self-consistently from Eqs. (2.6) and (2.7). An example is the case of Brillouin flow considered in Sec. II.B, where Eqs. (2.6) and (2.7) are solved subject to the assumption that the total electron energy is uniform, $[\gamma_e^0(x)-1]mc^2-e\phi_0(x)=$const, in the region $0\le x<x_b$.

In any case, Eqs. (2.6) and (2.7) can be integrated once to give a relation between the field profiles, $B_z(x)$ and $E_x(x)$, for general density profile $n_e^0(x)$. In this regard, we eliminate $n_e^0(x)$ in Eq. (2.7) by means of Poisson's equation (2.6). Integrating (2.7) with respect to x then gives

$$B_z^2(x)-E_x^2(x)=\text{const} \tag{2.8}$$

within the electron layer $(0\le x<x_b)$. As expected, it follows from Eq. (2.8) that the depression in the magnetic field $B_z(x)$ is largest at the cathode $(x=0)$ where $E_x(x=0)=0$. Moreover, $B_z(x)$ increases monotonically from $x=0$ to the value $B_z(x=x_b)=B_0$ at the outer edge of the electron layer $(x=x_b)$, where $E_x^2(x)$ assumes its maximum value determined from $E_x(x=x_b)=-4\pi e\int_0^{x_b}dx\,n_e^0(x)$. Introducing the relativistic mass factor $\gamma_e^0(x)$ defined by

$$\gamma_e^0(x)=[1-V_{ye}^{02}(x)/c^2]^{-1/2}=[1-E_x^2(x)/B_z^2(x)]^{-1/2}\ , \tag{2.9}$$

it also follows from Eq. (2.8) that

$$B_z(x)/\gamma_e^0(x)=\text{const} \tag{2.10}$$

within the electron layer $(0\le x<x_b)$. That is, whatever the equilibrium profiles, the functional forms of $B_z(x)$ and $\gamma_e^0(x)$ are identical in the region $0\le x<x_b$.

B. Relativistic Brillouin flow

For relativistic Brillouin flow (Brillouin, 1945, 1951; Lovelace and Ott, 1974; Ott and Lovelace, 1975; Antonsen and Ott, 1976; Swegle and Ott, 1981a, 1981b), the condition is imposed that the total energy of an electron fluid element is uniform across the electron layer. This condition can be expressed as

$$[\gamma_e^0(x)-1]m_e c^2-e\phi_0(x)=\text{const} , \tag{2.11}$$

where $\gamma_e^0(x)=[1-E_x^2(x)/B_z^2(x)]^{-1/2}$ is the relativistic mass factor and m_e is the electron rest mass. Here, $\phi_0(x=0)=0$ and $\gamma_e^0(x=0)=1$, so that the value of the constant in Eq. (2.11) is equal to zero. Taking the derivative of Eq. (2.11) with respect to x gives $\partial\gamma_e^0/\partial x=(e/m_e c^2)\partial\phi_0/\partial x$, which can also be expressed as

$$\gamma_e^{03}(x)\frac{E_x(x)}{B_z(x)}\frac{\partial}{\partial x}\left[\frac{E_x(x)}{B_z(x)}\right]=-\frac{eE_x(x)}{m_e c^2} , \tag{2.12}$$

where $E_x(x)=-\partial\phi_0(x)/\partial x$. Using Eqs. (2.6) and (2.7) to eliminate $\partial B_z/\partial x$ and $\partial E_x/\partial x$ in Eq. (2.12), we obtain the relativistic Brillouin flow condition

$$\left[\frac{eB_z(x)}{\gamma_e^0(x)m_e c}\right]^2=\frac{4\pi n_e^0(x)e^2}{\gamma_e^0(x)m_e} . \tag{2.13}$$

Note that Eq. (2.13) corresponds to the condition that the relativistic electron cyclotron frequency, $eB_z(x)/\gamma_e^0(x)mc$, is equal to the relativistic electron plasma frequency, $[4\pi n_e^0(x)e^2/\gamma_e^0(x)m_e]^{1/2}$, *locally* (at every x) within the electron layer. Because $B_z(x)/\gamma_e^0(x)=\text{const}$ [Eq. (2.10)], it follows from Eq. (2.13) that $n_e^0(x)/\gamma_e^0(x)=\text{const}$ within the electron layer $(0\le x<x_b)$. Therefore the profiles for $B_z(x)$, $\gamma_e^0(x)$, and $n_e^0(x)$ have identical spatial dependences in the interval $0\le x<x_b$.

Taking the derivative of Eq. (2.7) with respect to x, and making use of $n_e^0(x)/B_z(x)=\text{const}$ and $\partial E_x/\partial x=-4\pi e n_e^0$, we obtain

$$\frac{\partial^2}{\partial x^2}B_z(x)-\kappa^2 B_z(x)=0 , \tag{2.14}$$

where κ is defined by

$$\kappa\equiv 4\pi e n_e^0(x)/B_z(x)=\text{const}. \tag{2.15}$$

The solution to Eq. (2.14) is

$$B_z(x)=\begin{cases} B_0\dfrac{\cosh(\kappa x)}{\cosh(\kappa x_b)} , & 0\le x<x_b , \\ B_0 , & x_b<x\le d , \end{cases} \tag{2.16}$$

where $B_0=\text{const}$ denotes the uniform value of the axial magnetic field in the vacuum region $(x_b<x\le d)$. Similarly, the electron density $n_e^0(x)$, the relativistic mass factor $\gamma_e^0(x)$, the flow velocity $V_{ye}^0(x)$, and the electric field $E_x(x)$ can be expressed as

$$n_e^0(x)=\hat{n}_e\frac{\cosh(\kappa x)}{\cosh(\kappa x_b)} , \tag{2.17}$$

$$\gamma_e^0(x)=\cosh(\kappa x) , \tag{2.18}$$

$$V_{ye}^0(x)=c\tanh(\kappa x) , \tag{2.19}$$

$$E_x(x)=-B_0\frac{\sinh(\kappa x)}{\cosh(\kappa x_b)} , \tag{2.20}$$

within the electron layer $(0\le x<x_b)$. Note from Eq. (2.17) that the electron density $n_e^0(x)$ increases monotonically from the value $\hat{n}_e/\cosh(\kappa x_b)$ at the cathode $(x=0)$ to the value $\hat{n}_e=\text{const}$ at the outer edge of the electron layer $(x=x_b)$. Similarly, from Eq. (2.19), the equilibrium flow velocity $V_{ye}^0(x)$ increases monotonically from zero at $x=0$ to the value $c\tanh(\kappa x_b)$ at $x=x_b$. The profile functions $\cosh(\kappa x)$ and $\tanh(\kappa x)$ occurring in Eqs. (2.16)–(2.19) are plotted versus x/x_b in Fig. 3 for the case $\kappa x_b=1.317$ and $\hat{\gamma}_e\equiv\gamma_e^0(x=x_b)=2$.

The electrostatic potential $\phi_0(x)$ can be determined from $[\gamma_e^0(x)-1]m_e c^2-e\phi_0(x)=0$ within the electron layer $(0\le x<x_b)$, and from $\partial^2\phi_0/\partial x^2=0$ in the vacuum region $(x_b<x\le d)$. Making use of Eq. (2.18), and enforcing continuity of $\phi_0(x)$ and $\partial\phi_0(x)/\partial x$ at $x=x_b$, we obtain

$$\frac{e\phi_0(x)}{m_e c^2}=\begin{cases} [\cosh(\kappa x)-1], & 0\le x<x_b , \\ [\cosh(\kappa x_b)-1]+\kappa(x-x_b)\sinh(\kappa x_b), & x_b<x\le d . \end{cases} \tag{2.21}$$

Evaluating Eq. (2.21) at the anode $(x=d)$ where $\phi_0(x=d)=V$ gives

$$\frac{eV}{m_e c^2}=[\cosh(\kappa x_b)-1]+\kappa(d-x_b)\sinh(\kappa x_b) , \tag{2.22}$$

which relates the normalized voltage $eV/m_e c^2$ to κx_b and $\kappa(d-x_b)$.

It is useful to relate the vacuum field B_0 in Eq. (2.16) to the initial fill field B_f (assumed uniform in the region $0\le x\le d$) prior to the formation of the electron layer. Assuming magnetic-flux conservation with $\int_0^d dx\, B_z=\text{const}$, we obtain

$$B_f d=(B_0/\kappa)\tanh(\kappa x_b)+B_0(d-x_b) . \tag{2.23}$$

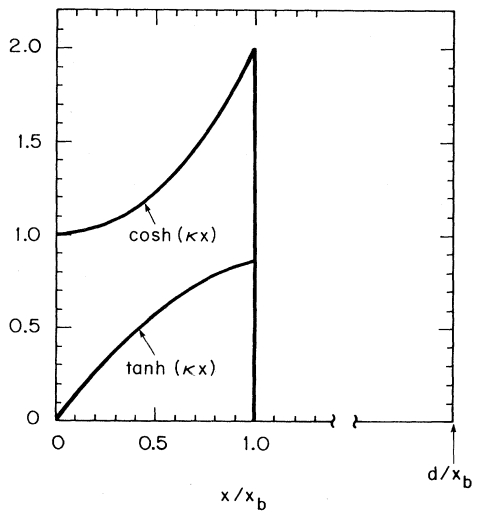

FIG. 3. Plots vs x/x_b of the profile functions $\cosh(\kappa x)$ and $\tanh(\kappa x)$ occurring in Eqs. (2.16)–(2.19) for $\kappa x_b=1.317$ and $\gamma_e=\gamma_e^0(x=x_b)=2$.

In terms of $B_z(x=0)=B_0/\cosh(\kappa x_b)$ at the cathode, Eq. (2.16) can be expressed in the equivalent form

$$\frac{eB_f d}{m_e c^2}=\frac{eB_z(x=0)}{m_e c^2\kappa}[\sinh(\kappa x_b)+\kappa(d-x_b)\cosh(\kappa x_b)] . \tag{2.24}$$

The coefficient $eB_z(x=0)/m_e c^2\kappa$ in Eq. (2.24) can be further simplified. In terms of the nonrelativistic frequencies $\omega_{ce}(x)=eB_z(x)/m_e c$ and $\omega_{pe}^2(x)=4\pi n_e^0(x)e^2/m_e$, the Brillouin flow condition in Eq. (2.13) can be expressed at the cathode [where $\gamma_e^0(x=0)=1$] as $\omega_{pe}^2(x=0)=\omega_{ce}^2(x=0)$. Equation (2.15) then gives $\kappa c=\omega_{pe}^2(x=0)/\omega_{ce}(x=0)$ or, equivalently,

$$\kappa c=\omega_{pe}(x=0)=\omega_{ce}(x=0) . \tag{2.25}$$

Therefore $eB_z(x=0)/m_e c^2\kappa=1$, and Eq. (2.24) reduces to

$$eB_f d/m_e c^2=\sinh(\kappa x_b)+\kappa(d-x_b)\cosh(\kappa x_b) . \tag{2.26}$$

For specified values of the normalized voltage $eV/m_e c^2$ and fill field $eB_f d/m_e c^2$, Eqs. (2.22) and (2.26) can be solved numerically to determine the self-consistent values of the normalized layer thickness x_b/d and electron density $\kappa^2 d^2=\omega_{pe}^2(x=0)d^2/c^2$. Typical numerical results are illustrated in Fig. 4, where x_b/d is plotted versus $eV/m_e c^2$ for several values of the magnetic fill field ranging from $eB_f d/m_e c^2=0.25$ to 8 (Davidson, 1990). As the electron flow become increasingly relativistic, we note from Fig. 4 that the curves asymptote abruptly to $x_b/d=1$ as the voltage V approaches the relativistic Hull cutoff voltage V_H (Hull, 1921; Lau, 1987). To calculate V_H, we set $x_b=d$ in Eqs. (2.22) and (2.26) and make use of $\cosh^2(\kappa x_b)-\sinh^2(\kappa x_b)=1$. This readily gives

$$eV_H/m_e c^2=(1+e^2B_f^2d^2/m_e^2c^4)^{1/2}-1 . \tag{2.27}$$

In the nonrelativistic regime with $e^2B_f^2d^2/m_e^2c^4\ll 1$ and $eV_H/m_e c^2\ll 1$, Eq. (2.27) reduces to $eV_H/m_e c^2=e^2B_f^2d^2/2m_e^2c^4$.

Shown in Fig. 5 is a plot of $eV_H/m_e c^2$ versus the normalized fill field $eB_f d/m_e c^2$. Magnetically insulated equilibria with $x_b<d$ exist provided the applied voltage satisfies

$$V<V_H . \tag{2.28}$$

For $V\ll V_H$, it is evident from Fig. 4 that the layer is thin ($x_b\ll d$). However, as the voltage is increased to $V=V_H$, the layer thickness increases to $x_b=d$.

For effective interaction between the layer electrons in a relativistic magnetron (Sec. IV), the layer thickness x_b should be at least large enough that the (fastest) electrons at $x=x_b$ resonate with the excited wave with phase velocity $v_p=\omega/k_y\equiv\beta_p c$. This requires that the voltage V exceed a value known as the Buneman-Hartree threshold voltage V_{BH} (Buneman, 1961; Lau, 1987). Eliminating

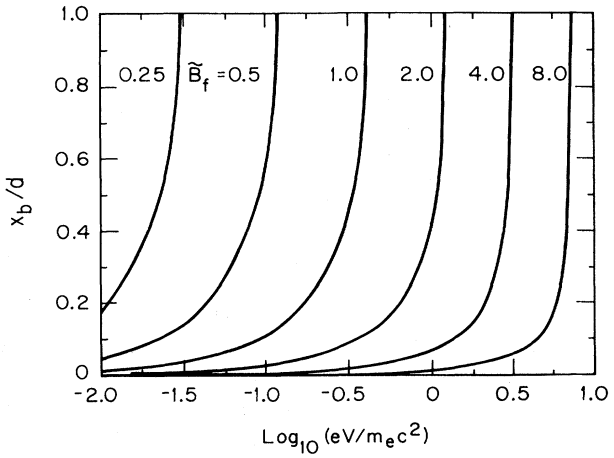

FIG. 4. Plots of the normalized layer thickness x_b/d vs $eV/m_e c^2$ obtained numerically from Eqs. (2.22) and (2.26) for several values of the normalized fill field ranging from $\tilde{B}_f\equiv eB_f d/m_e c^2=0.25$ to 8.

$\kappa(d-x_b)$, we combine Eqs. (2.22) and (2.26) to give

$$\frac{eV}{m_e c^2}=\frac{eB_f d}{m_e c^2}\tanh(\kappa x_b)-\left[1-\frac{1}{\cosh(\kappa x_b)}\right] . \tag{2.29}$$

Setting $V_{pe}^0(x=x_b)=c\tanh(\kappa x_b)=\omega/k_y\equiv\beta_p c$, and $\gamma_e^0(x=x_b)=\cosh(\kappa x_b)=(1-\beta_p^2)^{-1/2}$, it is readily shown from Eq. (2.29) that the Buneman-Hartree threshold voltage V_{BH} is given relativistically by

$$\frac{eV_{BH}}{m_e c^2}=\frac{eB_f d}{m_e c^2}\beta_p-[1-(1-\beta_p^2)^{1/2}] . \tag{2.30}$$

For phase velocity in the range $0<\beta_p<1$, it readily follows from Eqs. (2.27) and (2.30) that $V_H(B_f)\geq V_{BH}(B_f)$, where the equality holds when $eB_f d/m_e c^2=\beta_p/(1-\beta_p^2)^{1/2}$. For purposes of illustration, Fig. 5 also

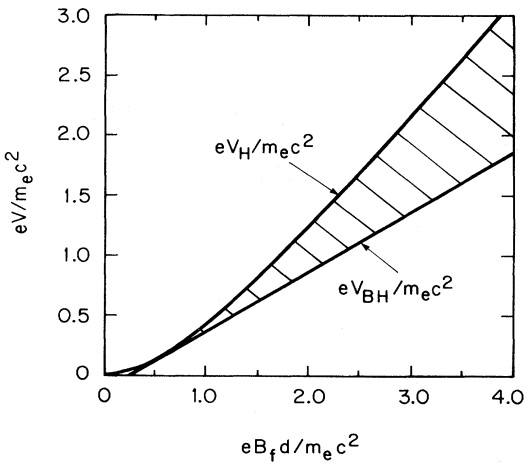

FIG. 5. Plots vs the normalized fill field $eB_f d/m_e c^2$ of the Hull cutoff voltage $eV_H/m_e c^2$ [Eq. (2.27)] and the Buneman-Hartree threshold voltage $eV_{BH}/m_e c^2$ [Eq. (2.30)] for $\beta_p=\omega/ck_y=0.5$.

shows a plot of eV_{BH}/m_ec^2 versus the normalized fill field eB_fd/m_ec^2 obtained from Eq. (2.30) for the choice of phase velocity $\beta_p=\omega/ck_y=0.5$. The allowed region of magnetron operation ($V_{BH}<V<V_H$) for $\beta_p=0.5$ then corresponds to the shaded region in Fig. 5.

C. General equilibrium profiles

As indicated in Sec. II.A, there is considerable latitude in making use of Eqs. (2.6) and (2.7) to describe equilibrium properties within the framework of a macroscopic cold-fluid model (Davidson, Tsang, and Swegle, 1984; Davidson and Tsang, 1985). For example, if the functional form of the equilibrium density profile $n_e^0(x)$ is specified, then Eq. (2.6) can be integrated to give

$$E_x(x)=-4\pi e\int_0^x dx\, n_e^0(x)\ . \tag{2.31}$$

Here, use has been made of the boundary condition $E_x(x=0)=0$ at the cathode [Eq. (2.3)]. In this case, the axial magnetic field $B_z(x)$ obtained from Eq. (2.7) [or Eq. (2.8)] is given by

$$B_z(x)=B_0\left[1-\frac{[E_x^2(x_b)-E_x^2(x)]}{B_0^2}\right]^{1/2} \tag{2.32}$$

in the interval $0\le x<x_b$. Here, $E_x(x)$ is defined in Eq. (2.31), and $\gamma_e^0(x)$ has the same spatial dependence as $B_z(x)$ within the electron layer [Eq. (2.10)].

As a second example, let us assume that the functional form of the relativistic mass factor $\gamma_e^0(x)=[1-E_x^2(x)/B_z^2(x)]^{-1/2}$ is specified within the electron layer, with $\gamma_e^0(x)$ increasing monotonically from $\gamma_e^0(x=0)=1$ at the cathode to the value $\gamma_e^0(x=x_b)\equiv\gamma_e$ at the outer edge of the electron layer. It then follows from Eqs. (2.6), (2.7), and (2.10) that the remaining equilibrium profiles are given self-consistently by

$$B_z(x)=\begin{cases}B_0\dfrac{\gamma_e^0}{\hat\gamma_e}\ , & 0\le x<x_b\ ,\\ B_0, & x_b<x\le d\ ,\end{cases} \tag{2.33}$$

$$n_e^0(x)=\begin{cases}\dfrac{B_0}{4\pi e\hat\gamma_e}\left[\dfrac{\partial}{\partial x}[\gamma_e^{02}(x)-1]^{1/2}\right], & 0\le x<x_b\ ,\\ 0, & x_b<x\le d\ ,\end{cases} \tag{2.34}$$

and

$$E_x(x)=\begin{cases}-\dfrac{B_0}{\hat\gamma_e}[\gamma_e^{02}(x)-1]^{1/2}\ , & 0\le x<x_b\ ,\\ E_x(x_b)\ , & x_b<x\le d\ .\end{cases} \tag{2.35}$$

Here, $B_0=B_z(x_b)$ and $-[\gamma_e^2-1]^{1/2}B_0/\hat\gamma_e=E_x(x_b)$ are the fields in the vacuum region ($x_b<x\le d$), and $\hat\gamma_e=\gamma_e^0(x_b)=[1-E_x^2(x_b)/B_0^2]^{-1/2}$ is the relativistic mass factor at the outer edge of the electron layer ($x=x_b$). Equations (2.33)–(2.35) are valid for the general choice of the equilibrium profile $\gamma_e^0(x)$. For the special choice $\gamma_e^0(x)=\cosh(\kappa x)$, where $\kappa\equiv 4\pi e\hat n_e/B_0$ and $\hat n_e\equiv n_e^0(x_b)$, it can be shown that Eqs. (2.33)–(2.35) recover (exactly) the equilibrium Brillouin flow profiles in Eqs. (2.16), (2.17), and (2.20). For general profile $\gamma_e^0(x)$, we note from Eq. (2.34) that the *average* electron density, $\bar n_e=x_b^{-1}\int_0^{x_b}dx\, n_e^0(x)$, can be expressed as

$$\bar n_e=\frac{[\hat\gamma_e^2-1]^{1/2}B_0}{4\pi e x_b\hat\gamma_e}=-\frac{E_x(x_b)}{4\pi e x_b}\ , \tag{2.36}$$

which determines $\bar n_e$ explicitly in terms of $\hat\gamma_e$, B_0, and x_b. As a general remark, it follows from Eq. (2.10) that the relativistic electron cyclotron frequency $\omega_{ce}(x)/\gamma_e^0(x)=eB_z(x)/\gamma_e^0(x)m_ec$ is uniform over the layer cross section. On the other hand, from Eq. (2.34), the relativistic electron plasma frequency-squared, $\omega_{pe}^2(x)/\gamma_e^0(x)=4\pi n_e^0(x)e^2/\gamma_e^0(x)m_e$, generally varies with x over the layer cross section. The special equilibrium profile $\gamma_e^0(x)=\cosh(\kappa x)$ is the only exception to this, in which case $n_e^0(x)/\gamma_e^0(x)=B_0\kappa/4\pi e\hat\gamma_e=$const. For purposes of illustration, we choose $\gamma_e^0(x)$ to have the functional form

$$\gamma_e^0(x)=\lambda\cosh(\kappa_1 x)+(1-\lambda)\frac{[1-\kappa_2^2(x_b^2-x^2)]^{1/2}}{(1-\kappa_2^2x_b^2)^{1/2}} \tag{2.37}$$

over the interval $0\le x<x_b$. Here, κ_1^{-1} and κ_2^{-1} are constant scale lengths, and λ is a variable parameter in the range $0\le\lambda\le 1$ which can be used to alter the shape of the equilibrium profiles. [The special case $\lambda=1$ corresponds to $\gamma_e^0(x)=\cosh(\kappa_1 x)$.] Note from Eq. (2.37) that $\gamma_e^0(x)$ increases monotonically from $\gamma_e^0(x=0)=1$ at the cathode to $\gamma_e^0(x=x_b)=\hat\gamma_e$ at the outer edge of the electron layer ($x=x_b$), where

$$\hat\gamma_e=\lambda\cosh(\kappa_1 x_b)+\frac{(1-\lambda)}{[1-\kappa_2^2x_b^2]^{1/2}}\ . \tag{2.38}$$

The equilibrium profile for $n_e^0(x)/\gamma_e^0(x)$ calculated from Eqs. (2.34) and (2.37) is illustrated in Fig. 6 for three values of the shape parameter corresponding to $\lambda=1$, 0.5, and 0 and to fixed values of $\kappa_1x_b=1.317$, $\kappa_2x_b=0.866$, and $\hat\gamma_e=2$. Note from Fig. 6 that the profile for $n_e^0(x)/\gamma_e^0(x)$ exhibits a sensitive dependence on λ, ranging from a uniform profile when $\lambda=1$ (similar to the case of Brillouin flow) to a profile that decreases by a factor of 2 over the layer cross section when $\lambda=0$. We shall find in Sec. III that the growth rate of the magnetron instability exhibits a sensitive dependence on the shape of the equilibrium profile $n_e^0(x)/\gamma_e^0(x)$, as measured by λ.

III. EXTRAORDINARY-MODE STABILITY PROPERTIES FOR PLANAR ELECTRON FLOW

In this section, use is made of a macroscopic cold-fluid model to investigate stability properties for

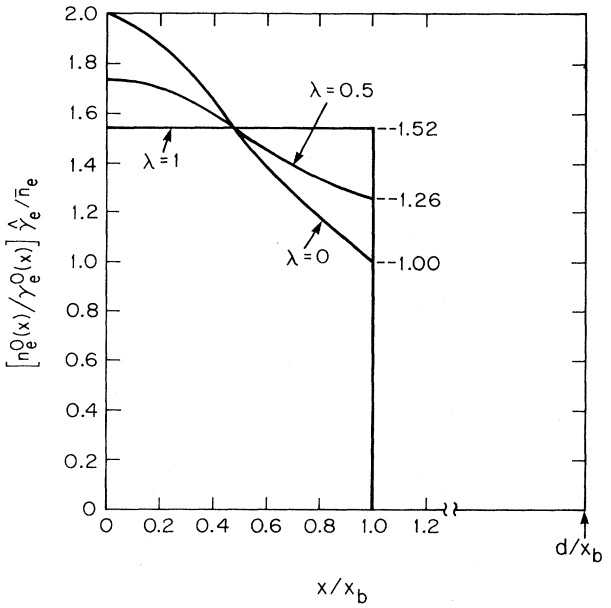

FIG. 6. Plot of the normalized profile $[n_e^0(x)/\gamma_e^0(x)]\hat{\gamma}_e/\bar{n}_e$ vs x/x_b calculated from Eqs. (2.34) and (2.37) for fixed values of $\kappa_1 x_b = 1.317$, $\kappa_2 x_b = 0.866$, and $\hat{\gamma}_e = 2$, and three values of the profile-shape parameter $\lambda = 1$, 0.5, and 0.

extraordinary-mode flute perturbations ($\partial/\partial z = 0$) about the general class of planar flow equilibria described in Sec. II (Davidson, Tsang, and Swegle, 1984; Davidson and Tsang, 1985; Davidson, 1990). Following a derivation of the eigenvalue equation (Sec. III.A), detailed properties of the magnetron instability are examined for nonrelativistic (Sec. III.B) and relativistic (Sec. III.C) electron flow. For low-frequency perturbations about a tenuous electron layer, it is then shown that relativistic and electromagnetic effects can have a strong stabilizing influence on the diocotron instability for sufficiently intense electron flow (Sec. III.D). Finally, for a tenuous electron layer, the influence of a periodic anode resonator on stability properties is discussed (Sec. III.E).

A. Extraordinary-mode eigenvalue equation

We make use of a macroscopic cold-fluid model to investigate the electromagnetic stability properties of magnetically insulated, relativistic electron flow in the planar geometry illustrated in Figs. 1 and 2. The present analysis assumes flute perturbations ($\partial/\partial z = 0$) about general equilibrium profiles $n_e^0(x)$, $E_x(x)$, and $B_z(x)$ consistent with Eqs. (2.6) and (2.7) and the boundary conditions in Eqs. (2.2) and (2.3). In addition, the electromagnetic field perturbations are assumed to have extraordinary-mode polarization with

$$\delta\mathbf{E}(\mathbf{x},t) = \delta E_x(x,y,t)\hat{\mathbf{e}}_x + \delta E_y(x,y,t)\hat{\mathbf{e}}_y ,$$
$$\delta\mathbf{B}(\mathbf{x},t) = \delta B_z(x,y,t)\hat{\mathbf{e}}_z . \tag{3.1}$$

The field components $\delta E_y(x,y,t)$, etc., are expressed as

$$\delta E_y(x,y,t) = \sum_{k=-\infty}^{\infty} \delta E_y(x,k)\exp(iky - i\omega t) . \tag{3.2}$$

Here, ω is the complex oscillation frequency with $\mathrm{Im}\omega > 0$ corresponding to instability (temporal growth); $k = 2\pi n/L$ is the wave number of the perturbation, where n is an integer; and L is the fundamental periodicity length in the y direction (the equilibrium flow direction).

The linearized, cold-fluid equations of continuity and momentum transfer give coupled equations for the perturbation amplitudes $\delta n_e(x,k)$, $\delta V_{xe}(x,k)$, $\delta V_{ye}(x,k)$, $\delta E_x(x,k)$, $\delta E_y(x,k)$, and $\delta B_z(x,k)$. We obtain

$$-i[\omega - kV_{ye}^0(x)]\delta n_e = -ikn_e^0(x)\delta V_{ye} - \frac{\partial}{\partial x}[n_e^0(x)\delta V_{xe}] , \tag{3.3}$$

$$-i[\omega - kV_{ye}^0(x)]\delta V_{xe} + [\omega_{ce}(x)/\gamma_e^0(x)]\delta V_{ye} = -\frac{e}{\gamma_e(x)m_e}\left[\delta E_x + \frac{1}{c}V_{ye}^0(x)\delta B_z\right] , \tag{3.4}$$

$$\left[-\frac{\omega_{ce}(x)}{\gamma_e^0(x)} + \frac{1}{\gamma_e^0(x)}\frac{\partial}{\partial x}[\gamma_e^0(x)V_{ye}^0(x)]\right]\delta V_{xe} - i[\omega - kV_{ye}^0(x)]\gamma_e^{02}(x)\delta V_{ye} = -\frac{e}{\gamma_e^0(x)m_e}\delta E_y , \tag{3.5}$$

where $V_{ye}^0(x) = -cE_x(x)/B_z(x)$, $\gamma_e^0(x) = [1 - E_x^2(x)/B_z^2(x)]^{-1/2}$, and $\delta\gamma_e(x,k) = \gamma_e^{03}(x)[V_{ye}^0(x)/c^2] \times \delta V_{ye}(x,k)$. Here, making use of the equilibrium Poisson equation (2.6), it is readily shown that

$$\frac{1}{\gamma_e^0}\frac{\partial}{\partial x}(\gamma_e^0 V_{ye}^0) = \gamma_e^{02}\frac{\partial V_{ye}^0}{\partial x} = \frac{\omega_{pe}^2(x)}{\omega_{ce}(x)} , \tag{3.6}$$

where $\omega_{ce}(x)$ and $\omega_{pe}(x)$ are the nonrelativistic electron cyclotron and plasma frequencies defined by

$$\omega_{ce}(x) = \frac{eB_z(x)}{m_e c} \quad \text{and} \quad \omega_{pe}^2(x) = \frac{4\pi n_e^0(x)e^2}{m_e} . \tag{3.7}$$

The perturbed field components δE_x, δE_y, and δB_z are related self-consistently to δn_e, δV_{xe}, and δV_{ye} by the linearized Maxwell equations. In this regard, it is convenient to introduce the effective potential $\Phi_k(x)$ defined by

$$\Phi_k(x) = (i/k)\delta E_y(x,k) . \tag{3.8}$$

After some straightforward algebra, the linearized Maxwell equations give

$$\delta E_x(x,k)=-\frac{1}{(1-\omega^2/c^2k^2)} \times\left[\frac{\partial}{\partial x}\Phi_k(x) +\frac{i\omega}{c^2k^2}4\pi e n_e^0(x)\delta V_{xe}(x,k)\right], \tag{3.9}$$

$$\delta B_z(x,k)=\frac{1}{(1-\omega^2/c^2k^2)} \times\left[\frac{\omega}{ck}\frac{\partial}{\partial x}\Phi_k(x)+\frac{i}{ck}4\pi e n_e^0(x)\delta V_{xe}(x,k)\right]. \tag{3.10}$$

In addition, the linearized Poisson equation becomes

$$\frac{\partial}{\partial x}\delta E_x(x,k)-k^2\Phi_k(x)=-4\pi e\,\delta n_e(x,k)\,. \tag{3.11}$$

Note from Eqs. (3.8)–(3.10) that the perturbations are electrostatic with $\delta E_x\simeq-\partial\Phi_k/\partial x$, $\delta E_y=-ik\Phi_k$, and $\delta B_z\simeq 0$, only in the limit where $|\omega/k|\ll c\to\infty$.

Substituting Eqs. (3.3) and (3.9) into Poisson's equation (3.11) gives

$$\left[\frac{\partial^2}{\partial x^2}-k^2\left[1-\frac{\omega^2}{c^2k^2}\right]\right]\Phi_k(x) =-\frac{4\pi e i}{[\omega-kV_{ye}^0(x)]} \times\left[\left[1-\frac{V_{ye}^0(x)}{c}\frac{\omega}{ck}\right]\frac{\partial}{\partial x}[n_e^0(x)\delta V_{xe}] +ik\left[1-\frac{\omega^2}{c^2k^2}\right][n_e^0(x)\delta V_{ye}]\right]. \tag{3.12}$$

Furthermore, substituting Eqs. (3.8)–(3.10) into Eqs. (3.4) and (3.5), we can express the perturbed fluid velocities $\delta V_{xe}(x,k)$ and $\delta V_{ye}(x,k)$ directly in terms of the effective potential $\Phi_k(x)$. Without presenting algebraic details (Davidson, Tsang, and Swegle, 1984), this gives the eigenvalue equation

$$\frac{\partial}{\partial x}\left[[1+\chi_\perp(x,k,\omega)]\frac{\partial}{\partial x}\Phi_k(x)\right]-k^2[1+\chi_\parallel(x,k,\omega)]\Phi_k(x) =\frac{k\Phi_k(x)}{[\omega-kV_{ye}^0(x)]}\left[1-\frac{V_{ye}^0(x)}{c}\frac{\omega}{ck}\right] \times\frac{\partial}{\partial x}\left[\frac{\omega_{pe}^2(x)\omega_{ce}(x)}{\gamma_e^{02}(x)\nu_e^2(x,k,\omega)}\right]. \tag{3.13}$$

Here, the susceptibilities occurring in Eq. (3.13) are defined by

$$\chi_\perp(x,k,\omega)=-\left[1-\frac{V_{ye}^0(x)}{c}\frac{\omega}{ck}\right]^2 \times\frac{\omega_{pe}^2(x)\gamma_e^0(x)}{(1-\omega^2/c^2k^2)\nu_e^2(x,k,\omega)}\,, \tag{3.14}$$

$$\chi_\parallel(x,k,\omega)=-\frac{\omega^2}{c^2k^2}-\frac{\omega_{pe}^2(x)}{\gamma_e^0(x)\nu_e^2(x,k,\omega)} \times\left[1-\frac{\omega^2}{c^2k^2}+\frac{\omega_{pe}^2(x)}{\gamma_e^0(x)c^2k^2}\right], \tag{3.15}$$

where

$$\nu_e^2(x,k,\omega) =\gamma_e^{02}(x)[\omega-kV_{ye}^0(x)]^2\left[1+\frac{\omega_{pe}^2(x)/\gamma_e^0(x)c^2k^2}{1-\omega^2/c^2k^2}\right] -[\omega_{ce}^2(x)/\gamma_e^{02}(x)-\omega_{pe}^2(x)/\gamma_e^0(x)]\,. \tag{3.16}$$

The eigenvalue equation (3.13) can be used to investigate detailed extraordinary-mode stability properties of the electron flow for a wide range of self-consistent equilibrium profiles $n_e^0(x)$, $E_x(x)$, and $B_z(x)$. In this regard, it should be emphasized that Eq. (3.13) includes the full influence of relativistic and electromagnetic effects on stability behavior in planar geometry. The complex eigenfunction $\Phi_k(x)=(i/k)\delta E_y(x,k)$ and the eigenfrequency ω are to be determined from Eq. (3.13) subject to the boundary conditions

$$\Phi_k(x=0)=0=\Phi_k(x=d)\,, \tag{3.17}$$

which correspond to zero tangential electric field ($\delta E_y=0$) at the cathode ($x=0$) and the anode ($x=d$). As a general remark, it is found that the eigenvalue equation (3.13) supports unstable solutions ($\mathrm{Im}\omega>0$) corresponding to the magnetron instability when the Doppler-shifted cyclotron resonance condition

$$\gamma_e^{02}(x_i)[\mathrm{Re}\omega-kV_{ye}^0(x_i)]^2\simeq\omega_{ce}^2(x_i)/\gamma_e^{02}(x_i) \tag{3.18}$$

is satisfied at some internal location ($x=x_i$) within the electron layer ($0<x_i<x_b$). Moreover, the growth rate depends on the strength of the self-fields (Davidson, Tsang, and Swegle, 1984) and the shape (Davidson and Tsang, 1985) of the equilibrium profiles.

B. Magnetron instability for nonrelativistic electron flow

Before making use of the eigenvalue equation (3.13) to investigate stability properties for relativistic electron flow, we summarize briefly the stability behavior calculated from Eq. (3.13) in the electrostatic regime, assuming nonrelativistic electron flow. Specifically, for $|\omega^2/c^2k^2|\ll 1$, $\omega_{pe}^2(x)/c^2k^2\ll 1$, $V_{ye}^{02}(x)/c^2\ll 1$, and $\gamma_e^0(x)\simeq 1$, it follows from Eqs. (3.13)–(3.16) that the eigenvalue equation can be approximated by (Davidson, 1990)

$$\frac{\partial}{\partial x}\left[\left[1-\frac{\omega_{pe}^2(x)}{[\omega-kV_{ye}^0(x)]^2-[\omega_{ce}^2-\omega_{pe}^2(x)]}\right]\frac{\partial}{\partial x}\Phi_k(x)\right]-k^2\left[1-\frac{\omega_{pe}^2(x)}{[\omega-kV_{ye}^0(x)]^2-[\omega_{ce}^2-\omega_{pe}^2(x)]}\right]\Phi_k(x)$$
$$=\frac{k\omega_{ce}\Phi_k(x)}{[\omega-kV_{ye}^0(x)]}\frac{\partial}{\partial x}\left[\frac{\omega_{pe}^2(x)}{[\omega-kV_{ye}^0(x)]^2-[\omega_{ce}^2-\omega_{pe}^2(x)]}\right] \quad (3.19)$$

in the nonrelativistic, electrostatic regime. Here, $\omega_{pe}^2(x)=4\pi n_e^0(x)e^2/m_e$ and $\omega_{ce}=eB_0/m_ec$, where $n_e^0(x)$ is the electron density profile, and the magnetic field $B_z(x)=B_0$ is taken to be uniform when $V_{ye}^{02}(x)/c^2\ll 1$. Similar to the case of relativistic electron flow (Sec. III.C), it is found from Eq. (3.19) that the electron cyclotron mode is subject to the magnetron instability for perturbations with sufficiently short wavelength (sufficiently large kx_b).

One interesting choice of equilibrium density profile in Eq. (3.19) corresponds to

$$n_e^0(x)=\begin{cases}\hat{n}_e=\text{const}, & 0\le x<x_b\ ,\\ 0, & x_b<x\le d\ .\end{cases} \quad (3.20)$$

That is, $\omega_{pe}^2(x)=\omega_{pe}^2=4\pi\hat{n}_e e^2/m_e=\text{const}$ within the electron layer, and the equilibrium flow velocity $V_{ye}^0(x)=-cE_x(x)/B_0$ is given by

$$V_{ye}^0(x)=s_e\omega_{ce}x \quad (3.21)$$

in the region $0\le x<x_b$. Here, s_e is the self-field parameter defined by

$$s_e=\frac{\omega_{pe}^2}{\omega_{ce}^2}=\frac{4\pi\hat{n}_e m_e c^2}{B_0}\ . \quad (3.22)$$

Note that s_e is a (dimensionless) measure of the strength of the equilibrium self-electric field. Because the electron layer is in contact with the cathode at $x=0$, the equilibrium described by Eqs. (3.20) and (3.21) is *not* subject to the classical diocotron instability (Levy, 1965). However, the cyclotron mode is subject to the magnetron instability (Buneman, Levy, and Linson, 1966).

For the choice of equilibrium profiles in Eqs. (3.20) and (3.21), Buneman, Levy, and Linson (1966) have performed an elegant analytical calculation (confirmed by numerical solution) of the asymptotic growth rate and real oscillation frequency of the magnetron instability for large values of $k^2x_b^2$. Without presenting algebraic details (Buneman, Levy, and Linson, 1966), it is found that

$$\begin{aligned}&\text{Re}\omega=\tfrac{1}{2}s_e(kx_b-1-\tfrac{1}{2}s_e)\omega_{ce}\ ,\\ &\text{Im}\omega=(\pi/2)s_e\omega_{ce}\exp(-2/s_e-1)\ ,\end{aligned} \quad (3.23)$$

for short-wavelength perturbations with $k^2x_b^2\gg 1/s_e^2$. Equation (3.23) has been derived for an arbitrary value of the self-field parameter s_e. Note that the real oscillation frequency $\text{Re}\omega$ scales linearly with the wave number k, which is consistent with the numerical results obtained in Sec. III.C for relativistic electron flow. Moreover, under Brillouin flow conditions ($s_e=\omega_{pe}^2/\omega_{ce}^2=1$), the maximum growth rate in Eq. (3.23) corresponds to $\text{Im}\omega/\omega_{ce}=\pi/2e^3=0.08$ for short-wavelength perturbations.

C. Magnetron instability for relativistic electron flow

We now make use of the eigenvalue equation (3.13) to investigate stability properties for relativistic electron flow. There is clearly a wide range of equilibrium profiles $n_e^0(x)$, $E_x(x)$, and $B_z(x)$, consistent with Eqs. (2.6) and (2.7), for which stability behavior can be examined. For present purposes, we specialize to the case where the relativistic mass factor $\gamma_e^0(x)$ has the functional form specified by Eq. (2.37), and the corresponding equilibrium profiles for $B_z(x)$, $n_e^0(x)$, and $E_x(x)$ are calculated self-consistently from Eqs. (2.33)–(2.35) (Davidson and Tsang, 1985). Here, keep in mind that the constant λ is a profile-shape parameter, where $\lambda=1$ corresponds to $\gamma_e^0(x)=\cosh(\kappa_1 x)$ in Eq. (2.37) and $n_e^0(x)=(B_0\kappa_1/4\pi e\hat{\gamma}_e)\cosh(\kappa_1 x)$ in Eq. (2.34), and $\lambda=0$ corresponds to a monotonically decreasing profile for $n_e^0(x)/\gamma_e^0(x)$ (Fig. 6).

Magnetron instability for $\lambda=1$. We first consider the case of strong magnetron instability corresponding to $\lambda=1$. In this regard, it is useful to introduce the self-field parameter s_e defined relativistically by

$$s_e=\frac{\omega_{pe}^2(x_b)/\hat{\gamma}_e}{\omega_{ce}^2(x_b)/\hat{\gamma}_e^2}=\frac{4\pi n_e\hat{\gamma}_e m_e c^2}{B_0^2}\ . \quad (3.24)$$

Here, $\hat{\gamma}_e=\gamma_e^0(x_b)=\cosh(\kappa_1 x_b)$, $\hat{n}_e=n_e^0(x_b)=B_0\kappa_1/4\pi e$, and $B_0=B_z(x_b)$ are evaluated at the outer edge of the electron layer ($x=x_b$). Indeed, for $\lambda=1$ and $\gamma_e^0(x)=\cosh(\kappa_1 x)$, it is readily shown from Eqs. (2.33) and (2.34) that the profiles for $n_e^0(x)$ and $B_z(x)$ are both proportional to $\cosh(\kappa_1 x)$. Therefore the local self-field parameter defined by $s_e(x)=[\omega_{pe}^2(x)/\gamma_e^0(x)]/[\omega_{ce}^2(x)/\gamma_e^{02}(x)]$ is uniform over the layer cross section and equal to the value of s_e defined in Eq. (3.24) at $x=x_b$. The condition $s_e=1$ corresponds exactly to the Brillouin flow condition (Swegle and Ott, 1981a, 1981b; Swegle, 1983) assumed in Sec. II.B, but is not required in the present stability analysis.

Typical numerical solutions (Davidson, Tsang, and Swegle, 1984) to the extraordinary-mode eigenvalue equation (3.13) are illustrated in Figs. 7 and 8 for the choice of system parameters corresponding to $\lambda=1$, $d=(3/2)x_b$, and $x_b=2c/\hat{\omega}_{ce}$. Here, $\hat{\omega}_{ce}\equiv\omega_{ce}(x_b)/\hat{\gamma}_e=eB_0/\hat{\gamma}_e m_e c$ is the relativistic cyclotron frequency at

the outer edge of the electron layer. Figure 7 shows the normalized growth rate $(\mathrm{Im}\omega)/\hat{\omega}_{ce}$ and the real oscillation frequency $(\mathrm{Re}\omega)/\hat{\omega}_{ce}$ of the magnetron instability plotted versus the normalized wave number $kc/\hat{\omega}_{ce}$ for the two cases corresponding to $s_e=1$ [Fig. 7(a)] and $s_e=0.5$ [Fig. 7(b)]. Several points are noteworthy from Fig. 7. First, the bandwidth of the magnetron instability is quite broad, with the maximum growth rate occurring for $kc/\hat{\omega}_{ce}\sim 3$ when $s_e=1$, and for $kc/\hat{\omega}_{ce}\sim 2$ when $s_e=0.5$. Second, the maximum growth rate decreases by about a factor of 4 when the self-field parameter s_e is reduced from $s_e=1$ to $s_e=0.5$. Finally, the real frequency $\mathrm{Re}\omega$ exceeds $\hat{\omega}_{ce}$ and scales approximately linearly with wave number k over the entire range of the instability, similar to the nonrelativistic case considered in Sec. III.B.

The strong dependence of stability properties on the strength of the equilibrium self-fields is further illustrated in Fig. 8(a), where $(\mathrm{Im}\omega)/\hat{\omega}_{ce}$ and $(\mathrm{Re}\omega)/\hat{\omega}_{ce}$ are plotted versus the self-field parameter s_e for fixed wave number $kc/\hat{\omega}_{ce}=2$, and system parameters otherwise identical to those in Fig. 7. Note from Fig. 8(a) that the growth rate of the magnetron instability is negligibly small for $s_e\leq 0.3$, but increases monotonically to $\mathrm{Im}\omega=0.0168\hat{\omega}_{ce}$ for $s_e=1$.

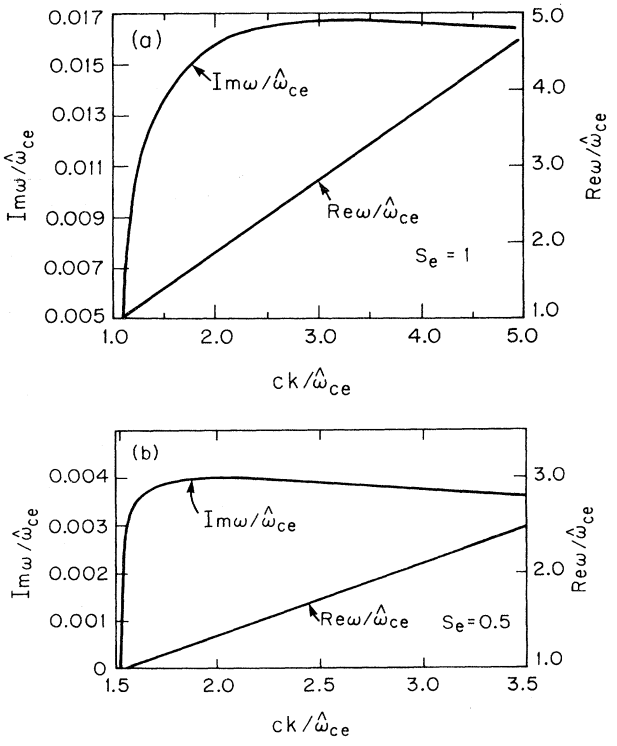

FIG. 7. Linear growth properties of the magnetron instability. The figures show plots vs $ck/\hat{\omega}_{ce}$ of the normalized growth rate $\mathrm{Im}\omega/\hat{\omega}_{ce}$ and the real oscillation frequency $\mathrm{Re}\omega/\hat{\omega}_{ce}$ obtained numerically from the eigenvalue equation (3.13). The choice of system parameters corresponds to $\lambda=1$, $d=(3/2)x_b$, and $x_b=2c/\hat{\omega}_{ce}$. The two values of the self-field parameter s_e correspond to (a) $s_e=1$ and (b) $s_e=0.5$.

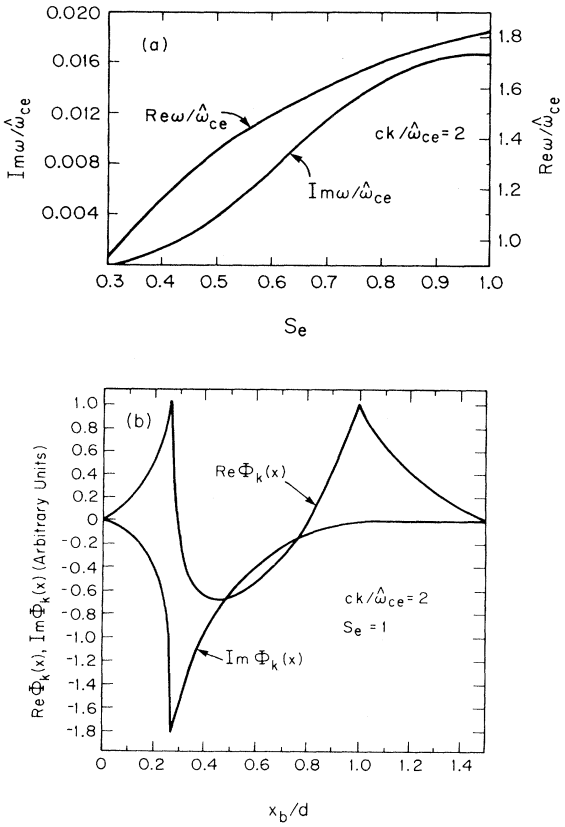

FIG. 8. Linear growth properties of the magnetron instability: (a) the normalized growth rate $\mathrm{Im}\omega/\hat{\omega}_{ce}$ and the real oscillation frequency $\mathrm{Re}\omega/\hat{\omega}_{ce}$ vs s_e; (b) the eigenfunction components $\mathrm{Re}\Phi_k(x)$ and $\mathrm{Im}\Phi_k(x)$ vs x/x_b for $s_e=1$, obtained numerically from the eigenvalue equation (3.13) for fixed wave number $ck/\hat{\omega}_{ce}=2$. The choice of system parameters is otherwise identical to Fig. 7.

Shown in Fig. 8(b) are eigenfunction plots of $\mathrm{Re}\Phi_k(x)$ and $\mathrm{Im}\Phi_k(x)$ vs x/x_b obtained from Eq. (3.13) for $s_e=1$ and fixed wave number $kc/\hat{\omega}_{ce}=2$. The corresponding complex oscillation frequency is $\omega=(1.83+0.0168i)\hat{\omega}_{ce}$. Note from Fig. 8(b) that the outer extremum of $\mathrm{Re}\Phi_k(x)$ occurs near the boundary of the electron layer $(x=x_b)$ where $\partial\omega_{pe}^2(x)/\partial x$ is large, corresponding to a large surface perturbation on the right-hand side of the eigenvalue equation (3.13). The strong peaking of $\mathrm{Re}\Phi_k(x)$ at $x=x_b$ is expected, since it is this large variation of $\omega_{pe}^2(x)$ at the plasma boundary that supports the surface wave which is driven unstable. Close examination of Eq. (3.13) and Fig. 8(b) shows that the inner extrema of $\mathrm{Re}\Phi_k(x)$ and $\mathrm{Im}\Phi_k(x)$ occur near the point $(x=x_i)$ where $1+\mathrm{Re}\chi_\perp(x_i,k,\omega)=0$. After some straightforward algebra that makes use of Eqs. (3.14) and (3.16), it can be shown that

$$1+\chi_\perp(x,k,\omega)=\frac{\gamma_e^{02}(x)[\omega-kV_{ye}^0(x)]^2-\omega_{ce}^2(x)/\gamma_e^{02}(x)}{\nu_e^2(x,k,\omega)}\ , \tag{3.25}$$

where $\omega_{ce}(x)=eB_z(x)/m_ec$. For small growth rate with $|\mathrm{Im}\omega| \ll |\mathrm{Re}\omega|$, the solution (x_i) to $1+\mathrm{Re}\chi_\perp(x_i,k,\omega)=0$ is determined approximately from the Doppler-shifted cyclotron resonance condition

$$\gamma_e^{02}(x_i)[\mathrm{Re}\omega - kV_{ye}^0(x_i)]^2=\hat{\omega}_{ce}^2 , \tag{3.26}$$

where use has been made of $\omega_{ce}(x)/\gamma_e^0(x)=\hat{\omega}_{ce}=$const across the electron layer. It is precisely the occurrence of this cyclotron resonance condition within the electron layers that leads to the magnetron instability.

As a final point, for $\lambda=1$ and $\gamma_e^0(x)=\cosh(\kappa_1 x)$, it is readily shown that $n_e^0(x)=\hat{n}_e\cosh(\kappa_1 x)/[\cosh(\kappa_1 x_b)]$, where $c\kappa_1=4\pi\hat{n}_e ec/B_0=s_e\hat{\omega}_{ce}$ and $\kappa_1 x_b=s_e(x_b\hat{\omega}_{ce}/c)$. Furthermore, solving Poisson's equation (2.6) for $\phi_0(x)$ and enforcing $\phi_0(x=d)=V$ gives

$$\frac{eV}{m_ec^2}=s_e\frac{\hat{\omega}_{ce}^2}{c^2\kappa_1^2}\{[\cosh(\kappa_1 x_b)-1] + \kappa_1(d-x_b)\sinh(\kappa_1 x_b)\} , \tag{3.27}$$

where $c\kappa_1/\hat{\omega}_{ce}=s_e$ and $\hat{\omega}_{ce}=eB_0/\hat{\gamma}_e m_e c$. For $s_e=1$ (and therefore $c\kappa_1=\hat{\omega}_{ce}$), Eq. (3.27) reduces to the familiar voltage relation (2.22), valid for Brillouin flow conditions. For the choice of parameters in Figs. 7 and 8, however, $x_b=2c/\hat{\omega}_{ce}$ so that $\kappa_1 x_b=2s_e$. Therefore the normalized voltage eV/m_ec^2 required to maintain $d=(3/2)x_b$ and $x_b=2c/\hat{\omega}_{ce}$ in Figs. 7 and 8 is different for each value of the self-field parameter s_e. For example, for $s_e=1$ in Figs. 7(a) and 8(b), the voltage relation (3.27) [or Eq. (2.22)] gives $eV/m_ec^2=6.39$, corresponding to $V=3.26$ MV.

Influence of profile shape on the magnetron instability. To illustrate the strong influence of profile shape on the magnetron instability, the eigenvalue equation (3.13) has been solved numerically (Davidson and Tsang, 1985) for the case in which $\gamma_e^0(x)$ is specified by Eq. (2.37) for several values of the shape parameter λ. The corresponding equilibrium profiles for $B_z(x)$, $n_e^0(x)$, and $E_x(x)$ are determined self-consistently from Eqs. (2.33)–(2.35). Typical numerical results are illustrated in Fig. 9, where $(\mathrm{Im}\omega)/\hat{\omega}_{ce}$ and $(\mathrm{Re}\omega)/\hat{\omega}_{ce}$ are plotted versus $kc/\hat{\omega}_{ce}$ for several values of λ. Here, the choice of system parameters corresponds to $d=3x_b$, $x_b=c/\hat{\omega}_{ce}$, $\kappa_1 x_b=1.319$, $\kappa_2 x_b=0.866$, and $\hat{\gamma}_e=\gamma_e^0(x_b)=2$. As before, $\hat{\omega}_{ce}=eB_0/\hat{\gamma}_e m_e c$ is the relativistic cyclotron frequency at $x=x_b$. Moreover, the average electron density $\bar{n}_e$ defined in Eq. (2.36) is the same for each value of λ in Fig. 9, and the value of the *average* self-field parameter is $\bar{s}_e=4\pi\bar{n}_e\hat{\gamma}_e m_e c^2/B_0^2=0.866$. For $\lambda=1$, it is evident from Fig. 9(a) that the growth rate of the magnetron instability is quite robust, with general features similar to those in Fig. 7(a). On the other hand, as λ is decreased from $\lambda=1$, and the profile for $n_e^0(x)/\gamma_e^0(x)$ decreases monotonically with increasing x (Fig. 6), it is evident from Fig. 9(a) that the instability growth rate $\mathrm{Im}\omega$ is reduced substantially, at least at longer wavelengths. Indeed, for the range of $kc/\hat{\omega}_{ce}$ shown in the figure

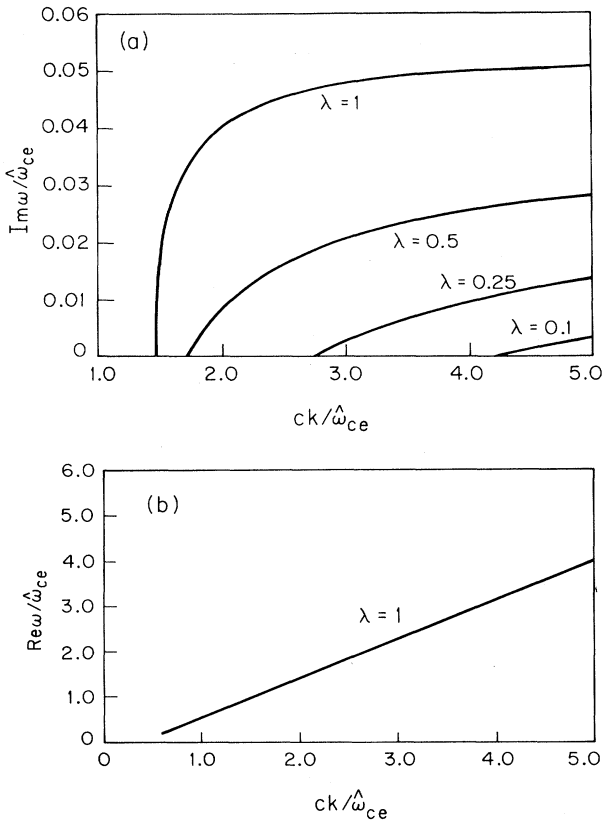

FIG. 9. Linear growth properties of the magnetron instability shown by plots vs $ck/\hat{\omega}_{ce}$ of (a) the normalized growth rate $\mathrm{Im}\omega/\hat{\omega}_{ce}$ and (b) the normalized real frequency $\mathrm{Re}\omega/\hat{\omega}_{ce}$ obtained numerically from the eigenvalue equation (3.13). The choice of system parameters corresponds to $d=3x_b$, $x_b=c/\hat{\omega}_{ce}$, $\kappa_1 x_b=1.319$, $\kappa_2 x_b=0.866$, $\hat{\gamma}_e=2$, and $\bar{s}_e=0.866$, and several values of the profile-shape parameter λ. The plots of $\mathrm{Re}\omega/\hat{\omega}_{ce}$ vs $ck/\hat{\omega}_{ce}$ for λ in the interval $0.06\le\lambda\le 1$ are virtually identical to the $\lambda=1$ curve in (b).

$(kc/\hat{\omega}_{ce}\le 5)$, instability ceases $(\mathrm{Im}\omega=0)$ for $\lambda\le 0.06$. On the other hand, the plots of $(\mathrm{Re}\omega)/\hat{\omega}_{ce}$ vs $ck/\hat{\omega}_{ce}$ for λ in the interval $0.06\le\lambda\le 1$ are virtually identical to the curve plotted in Fig. 9(b) for $\lambda=1$. That is, the real frequency of the magnetron mode is relatively insensitive to the profile shape.

It should be noted that the voltage V required to maintain $d=3x_b$ and $x_b=c/\hat{\omega}_{ce}$ in Fig. 9 is different for each value of λ. For example, for $\lambda=0$, Poisson's equation (2.6) can be integrated from $x=0$ to $x=d$ to give $eV/m_ec^2=4.33$, which corresponds to $V=2.2$ MV.

D. Diocotron instability for a tenuous relativistic electron layer

The diocotron instability (MacFarlane and Hay, 1950; Buneman, 1957; Levy, 1965; Davidson, 1990) is one of the most ubiquitous instabilities in low-density non-neutral plasmas with shear in the flow velocity. For ex-

ample, it can occur in a rotating non-neutral plasma column with off-axis density maximum (Rosenthal, Dimonte, and Wong, 1987; Fine, Driscoll, and Malmberg, 1989), in propagating non-neutral electron beams and layers (Kyhl and Webster, 1956; Pierce, 1956; Kapetanakos *et al.*, 1973), and in microwave generation devices such as magnetrons, traveling-wave tubes, and ubitrons (Lau, 1987). An important feature of the diocotron instability is that it can be completely stabilized by relativistic and electromagnetic effects (Davidson, Tsang, and Uhm, 1988) for sufficiently intense non-neutral electron flow. To illustrate this point, we now make use of the eigenvalue equation (3.13) to investigate linear properties of the diocotron instability for extraordinary-mode perturbations about a tenuous electron layer that is detached from the cathode in the planar geometry illustrated in Figs. 1 and 2.

For purposes of describing the diocotron instability, we specialize to the case of low-frequency perturbations about a tenuous electron layer satisfying

$$\begin{aligned} &\omega_{pe}^2(x) \ll \omega_{ce}^2(x)/\gamma_e^0(x) , \\ &\gamma_e^{02}(x)|\omega - kV_{ye}^0(x)|^2 \ll \omega_{ce}^2(x)/\gamma_e^{02}(x) . \end{aligned} \tag{3.28}$$

Here, $\omega_{pe}(x)=[4\pi n_e^0(x)e^2/m]^{1/2}$ and $\omega_{ce}(x)=eB_z(x)/m_e c$ are the nonrelativistic electron plasma frequency and cyclotron frequency, respectively; ω is the complex oscillation frequency; k is the perturbation wave number in the y direction; and $\gamma_e^0(x)=[1-(E_x/B_z)^2]^{-1/2}$ is the relativistic mass factor of an electron fluid element. In Eq. (2.10) it was shown that $B_z(x)/\gamma_e^0(x)=$const across the extent of the electron layer. Within the context of Eq. (3.28), the electrons are treated as a massless ($m_e \to 0$) guiding-center fluid in which $\omega_{pe}^2(x)/\omega_{ce}^2(x) \to 0$, but the ratio

$$\frac{\omega_{pe}^2(x)}{\omega_{ce}(x)} = \frac{4\pi n_e^0(x)ec}{B_z(x)} \equiv c\kappa(x) \tag{3.29}$$

remains finite.

Making use of Eq. (3.28) to simplify the extraordinary-mode eigenvalue equation (3.13) derived for arbitrary ω and $\omega_{pe}^2/\omega_{ce}^2$, we obtain (Davidson, Tsang, and Uhm, 1988)

$$\begin{aligned} &\frac{\partial^2}{\partial x^2}\Phi_k(x) - k^2\left[1 - \frac{\omega^2}{c^2k^2} + \frac{\omega_{pe}^4(x)}{c^2k^2\omega_{ce}^2(x)}\right]\Phi_k(x) \\ &\quad = -\frac{4\pi eck\Phi_k(x)}{[\omega - kV_{ye}^0(x)]}\left[1 - \frac{V_{ye}^0(x)}{c}\frac{\omega}{ck}\right]\frac{\partial}{\partial x}\left[\frac{n_e^0(x)}{B_z(x)}\right] , \end{aligned} \tag{3.30}$$

where $\Phi_k(x) \equiv (i/k)\delta E_y(x,k)$. Although a tenuous electron layer and $m_e \to 0$ have been assumed, the eigenvalue equation (3.30) is fully electromagnetic and valid for relativistic flow velocities. In this regard, Eq. (3.30) can be used to investigate the low-frequency stability properties of a low-density electron layer for a broad range of equilibrium profiles consistent with the steady-state Maxwell equations (2.6) and (2.7). For nonrelativistic electron flow with $V_{ye}^{02}/c^2 \ll 1$ and $B_z(x) \simeq B_0 =$const, and slow-wave perturbations with $|\omega^2/c^2k^2| \ll 1$, we note that Eq. (3.30) reduces to the familiar electrostatic eigenvalue equation (Davidson, 1990) used to investigate the diocotron instability for nonrelativistic flow in planar geometry.

As a particular example that is analytically tractable, we consider perturbations about the class of equilibrium profiles where $n_e^0(x)/\gamma_e^0(x)$ has the simple rectangular shape (Fig. 10)

$$\frac{n_e^0(x)}{\gamma_e^0(x)} = \begin{cases} 0, & 0 \le x < x_b^- , \\ \hat{n}_e/\hat{\gamma}_e = \text{const}, & x_b^- < x < x_b^+ , \\ 0, & x_b^+ < x \le d . \end{cases} \tag{3.31}$$

In Eq. (3.31), $\hat{n}_e \equiv n_e^0(x=x_b^+)$ and $\hat{\gamma}_e \equiv \gamma_e^0(x=x_b^+)$ denote the electron density and energy, respectively, at the outer edge ($x=x_b^+$) of the electron layer. Moreover, Eq. (3.31) generally allows for the inner edge of the electron layer ($x=x_b^-$) to be detached from the conducting wall at $x=0$, although the case $x_b^-=0$ is not excluded. A configuration like that illustrated in Fig. 10 or Eq. (3.31) could occur in a high-voltage diode if the magnetically insulated electron sheath becomes detached from the cathode (at $x=0$).

For $n_e^0(x)/\gamma_e^0(x)$ specified by Eq. (3.31), it can be shown from the steady-state Maxwell equations (2.6) and (2.7) that the self-consistent equilibrium profiles for the magnetic field $B_z(x)$, the electric field $E_x(x)$, the relativistic mass factor $\gamma_e^0(x)$, and the flow velocity $V_{ye}^0(x)$ can be expressed as

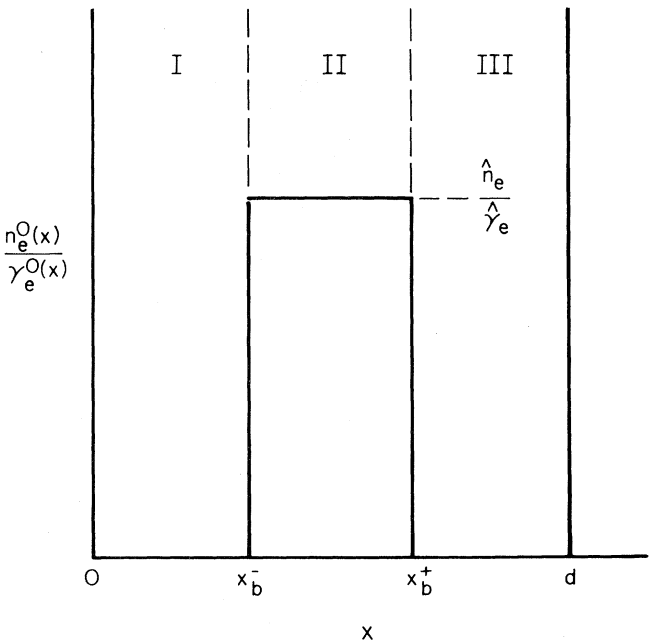

FIG. 10. Plot of $n_e^0(x)/\gamma_e^0(x)$ vs x for the rectangular profile in Eq. (3.31).

$$B_z(x)=B_0\frac{\cosh[\kappa(x-x_b^-)]}{\cosh[\kappa(x_b^+-x_b^-)]}\ , \tag{3.32}$$

$$E_x(x)=-B_0\frac{\sinh[\kappa(x-x_b^-)]}{\cosh[\kappa(x_b^+-x_b^-)]}\ , \tag{3.33}$$

$$\gamma_e^0(x)=\cosh[\kappa(x-x_b^-)]\ , \tag{3.34}$$

$$V_{ye}^0(x)=c\tanh[\kappa(x-x_b^-)]\ , \tag{3.35}$$

within the electron layer $(x_b^-<x<x_b^+)$. Here, $B_0\equiv B_z(x=x_b^+)$ is the applied magnetic field in the outer vacuum region $(x_b^+<x\le d)$ in Fig. 10. Moreover, the constant κ is defined by

$$c\kappa=\frac{\omega_{pe}^2(x=x_b^+)}{\omega_{ce}(x=x_b^+)}=\frac{4\pi\hat{n}_e ec}{B_0}\ , \tag{3.36}$$

where $\hat{n}_e$ and B_0 are the density and magnetic field at the outer edge of the electron layer $(x=x_b^+)$. Indeed, because $n_e^0(x)/B_z(x)=$const follows from Eqs. (3.31) and (3.32), it is readily shown that

$$c\kappa(x)\equiv\omega_{pe}^2(x)/\omega_{ce}(x)=c\kappa=\text{const} \tag{3.37}$$

throughout the cross section of the electron layer $(x_b^-<x<x_b^+)$. Here, κ is the constant defined in Eq. (3.36).

Making use of Eq. (3.37), it follows that $4\pi ec(\partial/\partial x)[n_e^0(x)/B_z(x)]=c\kappa[\delta(x-x_b^-)-\delta(x-x_b^+)]$ for the choice of equilibrium profiles in Eqs. (3.31) and (3.32). Therefore the eigenvalue equation (3.30) can be expressed as

$$\begin{aligned}\frac{\partial^2}{\partial x^2}\Phi_k(x)-\kappa^2(x,\omega)\Phi_k(x)&\\ =-\frac{ck}{\omega}\kappa\Phi_k(x_b^-)\delta(x-x_b^-)&\\ +\frac{ck\kappa\Phi_k(x_b^+)}{\omega-kV_d}\left[1-\frac{V_d}{c}\frac{\omega}{ck}\right]\delta(x-x_b^+)\ .&\end{aligned} \tag{3.38}$$

Here, $V_d\equiv V_{ye}^0(x=x_b^+)=c\tanh[\kappa(x_b^+-x_b^-)]$ is the flow velocity at the outer edge of the electron layer, and $\kappa^2(x,\omega)$ is defined by

$$\kappa^2(x,\omega)=\begin{cases}\kappa_v^2(\omega)=k^2\left[1-\dfrac{\omega^2}{c^2k^2}\right], & 0\le x<x_b^-\ ,\\ \kappa_b^2(\omega)=k^2\left[1-\dfrac{\omega^2}{c^2k^2}+\dfrac{\kappa^2}{k^2}\right], & x_b^-<x<x_b^+\ ,\\ \kappa_v^2(\omega)=k^2\left[1-\dfrac{\omega^2}{c^2k^2}\right], & x_b^+<x\le d\ .\end{cases} \tag{3.39}$$

Note that the right-hand side of Eq. (3.38) corresponds to surface perturbations on the outer $(x=x_b^+)$ and inner $(x=x_b^-)$ surfaces of the electron layer. Note also from Eq. (3.39) that $\kappa^2(x,\omega)$ is constant (independent of x) in each of the three regions. It is clear from the eigenvalue equation (3.38) that the relativistic flow parameter

$$\theta=\kappa(x_b^+-x_b^-)=\frac{4\pi\hat{n}_e e(x_b^+-x_b^-)}{B_0} \tag{3.40}$$

will play an important role in determining the detailed stability properties. For example, from Eq. (3.35), $V_d=V_{ye}^0(x=x_b^+)$ can be expressed as

$$V_d=c\tanh\theta\ . \tag{3.41}$$

The right-hand side of the eigenvalue equation (3.38) vanishes, except at the inner and outer surfaces of the electron layer at $x=x_b^-$ and $x=x_b^+$. We therefore solve Eq. (3.38) separately in each of the three regions in Fig. 10, enforcing the continuity of $\Phi_k(x)$ at $x=x_b^-$ and $x=x_b^+$, and setting $\Phi_k(x=0)=0=\Phi_k(x=d)$, which corresponds to zero tangential electric field, $\delta E_y=-ik\Phi_k=0$, at the conducting walls. The solutions to Eq. (3.38) in the three regions are given by

$$\Phi_k^{\rm I}(x)=B\frac{\sinh[\kappa_v(\omega)x]}{\sinh[\kappa_v(\omega)x_b^-]},\quad 0\le x<x_b^-\ , \tag{3.42}$$

$$\begin{aligned}\Phi_k^{\rm II}(x)=B\frac{\sinh[\kappa_b(\omega)(x_b^+-x)]}{\sinh[\kappa_b(\omega)(x_b^+-x_b^-)]}&\\ +C\frac{\sinh[\kappa_b(\omega)(x-x_b^-)]}{\sinh[\kappa_b(\omega)(x_b^+-x_b^-)]}\ ,x_b^-<x<x_b^+\ ,&\end{aligned} \tag{3.43}$$

$$\Phi_k^{\rm III}(x)=C\frac{\sinh[\kappa_v(\omega)(d-x)]}{\sinh[\kappa_v(\omega)(d-x_b^+)]},\quad x_b^+<x\le d\ . \tag{3.44}$$

The remaining boundary conditions are obtained by integrating the eigenvalue equation across the layer surfaces at $x=x_b^-$ and $x=x_b^+$. This gives

$$\left[\frac{\partial}{\partial x}\Phi_k^{\rm II}\right]_{x=x_b^-}-\left[\frac{\partial}{\partial x}\Phi_k^{\rm I}\right]_{x=x_b^-}=-\frac{ck\kappa}{\omega}\Phi_k(x_b^-) \tag{3.45}$$

and

$$\begin{aligned}\left[\frac{\partial}{\partial x}\Phi_k^{\rm III}\right]_{x=x_b^+}-\left[\frac{\partial}{\partial x}\Phi_k^{\rm II}\right]_{x=x_b^+}=\frac{ck\kappa\Phi_k(x_b^+)}{\omega-kV_d}&\\ \times\left[1-\frac{V_d}{c}\frac{\omega}{ck}\right],&\end{aligned} \tag{3.46}$$

where $V_d=c\tanh\theta$.

Substituting Eqs. (3.42)–(3.44) into Eqs. (3.45) and (3.46), we can eliminate the constants B and C to obtain a closed dispersion relation for the complex eigenfrequency ω. After some algebraic manipulation, we obtain (Davidson, Tsang, and Uhm, 1988)

$$\{\kappa_v(\omega)\coth[\kappa_v(\omega)(x_b^+-d)]-\kappa_b(\omega)\coth[\kappa_b(\omega)(x_b^+-x_b^-)]-\kappa_v(\omega)f^+(\omega)\}$$
$$\times\{\kappa_v(\omega)\coth[\kappa_v(\omega)x_b^-]+\kappa_b(\omega)\coth[\kappa_b(\omega)(x_b^+-x_b^-)]-\kappa_v(\omega)f^-(\omega)\}=-\frac{\kappa_b^2(\omega)}{\sinh^2[\kappa_b(\omega)(x_b^+-x_b^-)]}\ . \tag{3.47}$$

Here, $\kappa_v(\omega)$ and $\kappa_b(\omega)$ are the dielectric functions defined in Eq. (3.39), and $f^-(\omega)$ and $f^+(\omega)$ are the coupling coefficients at the surfaces of the electron layer defined by

$$f^-(\omega)=\frac{k}{\kappa_v(\omega)}\frac{c\kappa}{\omega}\ ,$$
$$f^+(\omega)=\frac{k}{\kappa_v(\omega)}\frac{c\kappa}{\omega-kV_d}\left[1-\frac{V_d}{c}\frac{\omega}{ck}\right]\ . \tag{3.48}$$

The dispersion relation (3.47) is a transcendental equation that determines the complex oscillation frequency ω in terms of the wave number k and equilibrium layer parameters such as κ, V_d, $x_b^+-x_b^-$, etc. In Eq. (3.47), we note that perturbations on the outer surface of the electron layer (the first factor on the left-hand side) are coupled to perturbations on the inner surface of the layer (the second factor on the left-hand side) through body-wave perturbations within the layer (the right-hand side). The dispersion relation (3.47) is fully electromagnetic and valid for relativistic electron flow in the limit where the electrons are treated as a massless, guiding-center fluid. In this regard, Eq. (3.47) can be used to investigate detailed stability properties for low-frequency perturbations about a tenuous electron layer [Eq. (3.28)] for the class of equilibrium profiles described by Fig. 10 and Eqs. (3.31)–(3.35).

As a limiting case that is analytically tractable, we first assume long-wavelength perturbations $k^2d^2\ll 1$. For $|\omega^2/c^2k^2|\lesssim 1$, it readily follows from Eq. (3.39) that $|\kappa_v(x_b^+-d)|\ll 1$, $|\kappa_v x_b^-|\ll 1$, and $|\kappa_b(x_b^+-x_b^-)|\simeq\kappa(x_b^+-x_b^-)=\theta$, when $k^2d^2\ll 1$. Examination of Eq. (3.47) in the long-wavelength regime shows that the dispersion relation can be approximated by the quadratic equation $\omega^2-b\omega+c=0$, where the coefficients b and c are independent of ω, but depend on $\theta=\kappa(x_b^+-x_b^-)/c$ and the dimensionless geometric factors

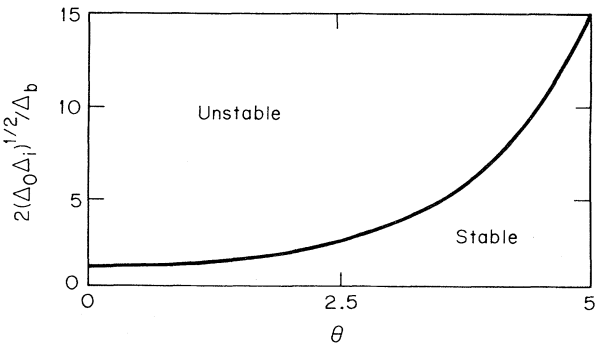

FIG. 11. For long-wavelength perturbations ($k^2d^2\ll 1$), the diocotron instability is stabilized by relativistic and electromagnetic effects whenever $2(\Delta_0\Delta_i)^{1/2}/\Delta_b<(\sinh\theta)/\theta$.

$$\Delta_i=x_b^-/d\ ,$$
$$\Delta_b=(x_b^+-x_b^-)/d\ , \tag{3.49}$$
$$\Delta_0=(d-x_b^+)/d\ .$$

It is found that the necessary and sufficient condition for instability ($4c-b^2>0$) in the long-wavelength regime ($k^2d^2\ll 1$) can be expressed as (Davidson, Tsang, and Uhm, 1988)

$$g\equiv 2(\Delta_0\Delta_i)^{1/2}/\Delta_b>(\sinh\theta)/\theta\ . \tag{3.50}$$

This is illustrated schematically in Fig. 11, where the solid curve corresponds to $2(\Delta_0\Delta_i)^{1/2}/\Delta_b=(\sinh\theta)/\theta$, which separates the unstable and stable regions. Moreover, for $k^2d^2\ll 1$, whenever the inequality in Eq. (3.50) is satisfied, the corresponding normalized growth rate $\mathrm{Im}\omega/c|k|$ and real oscillation frequency are given by

$$\frac{\mathrm{Im}\omega}{c|k|}=\frac{1}{2}\theta\left[g^2-\frac{\sinh^2\theta}{\theta^2}\right]^{1/2}\times\left[\cosh\theta+\frac{\theta}{\Delta_b\sinh\theta}(\Delta_i\cosh^2\theta+\Delta_0)\right]^{-1} \tag{3.51}$$

and

$$\frac{\mathrm{Re}\omega}{ck}=\frac{1}{2}\left[\sinh\theta+\frac{2\Delta_i}{\Delta_b}\theta\cosh\theta\right]\times\left[\cosh\theta+\frac{\theta}{\Delta_b\sinh\theta}(\Delta_i\cosh^2\theta+\Delta_0)\right]^{-1}\ , \tag{3.52}$$

where $g=2(\Delta_0\Delta_i)^{1/2}/\Delta_b$. It readily follows that $g=0$ for $\Delta_i=0$ or for $\Delta_0=0$. Because $g>(\sinh\theta)/\theta$ is a necessary and sufficient condition for instability ($\mathrm{Im}\omega>0$), we therefore conclude that the system is stable ($\mathrm{Im}\omega=0$) whenever the electron layer is in contact with the cathode ($\Delta_i=0$) or the anode ($\Delta_0=0$), as expected. In the nonrelativistic, electrostatic regime ($\theta\ll 1$), we further note that Eqs. (3.51) and (3.52) reduce to $\mathrm{Im}\omega/c|k|=(\theta/2)[4\Delta_i\Delta_0-\Delta_b^2]^{1/2}$ and $\mathrm{Re}\omega/ck=(\theta/2)(\Delta_b+2\Delta_i)$.

With the restriction $k^2d^2\ll 1$ removed, the full dispersion relation (3.47) has been solved numerically for $\mathrm{Im}\omega/c|k|$ and $\mathrm{Re}\omega/ck$ (Davidson, Tsang, and Uhm, 1988). Typical results are illustrated in Fig. 12 for $\Delta_i=x_b^-/d=0.3$ and $\Delta_0=(d-x_b^+)/d=0.6$. As a general remark, for increasing values of kd, it is found that there is a concomitant decrease in both the maximum normalized growth rate and the range of θ corresponding to instability. Moreover, the long-wavelength *stability criterion*, $2(\Delta_0\Delta_i)^{1/2}/\Delta_b<(\sinh\theta)/\theta$, is found to be a sufficient condition for the diocotron instability to be stabilized at all perturbation wavelengths.

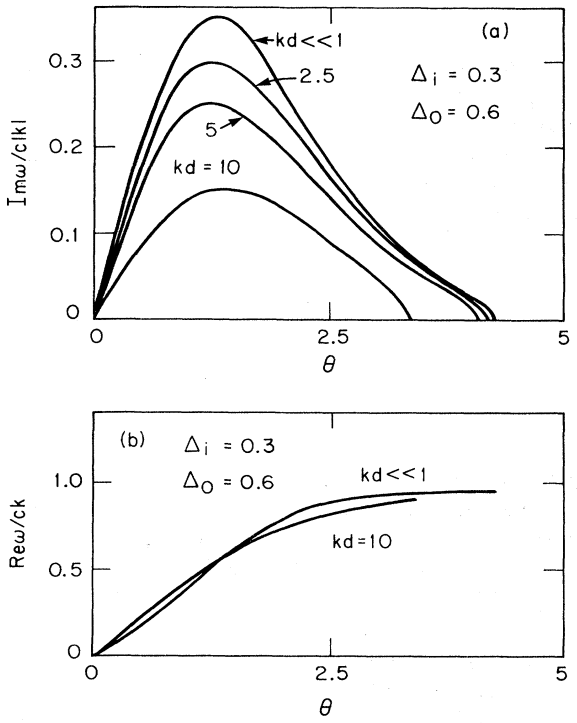

FIG. 12. Plots of (a) $\mathrm{Im}\omega/c|k|$ and (b) $\mathrm{Re}\omega/ck$ vs the relativistic flow parameter θ obtained numerically from Eq. (3.47) for $\Delta_i=0.3$, $\Delta_0=0.6$, and several values of kd.

The preceding analysis represents a rather striking example in which an instability that is highly ubiquitous in the nonrelativistic, electrostatic regime can be completely stabilized by relativistic and electromagnetic effects.

As a final point, for an electron layer in contact with the cathode ($x_b^-=0$), it readily follows that the general dispersion relation (3.47) reduces to

$$k\frac{c\kappa}{\omega-kV_d}\left[1-\frac{V_d}{c}\frac{\omega}{ck}\right]=-\kappa_v(\omega)\coth[\kappa_v(\omega)(d-x_b^+)]-\kappa_b(\omega)\coth[\kappa_b(\omega)x_b^+]\ . \tag{3.53}$$

Here, $c\kappa=4\pi\hat{n}_e ec/B_0$, $V_d=c\tanh\theta$, $\theta=\kappa x_b^+$, and $\kappa_v(\omega)$ and $\kappa_b(\omega)$ are defined in Eq. (3.39). As expected, for an electron layer in contact with the cathode, the dispersion relation (3.53) supports solutions corresponding only to stable oscillations ($\mathrm{Im}\omega=0$). That is, for $x_b^-=0$, the surface perturbation excited on the electron layer at $x=x_b^+$ does not experience an unstable coupling to the electromagnetic wave in the vacuum region ($x_b^+<x\le d$). This behavior is different from the case in which the planar anode surface in Figs. 1 and 2 is replaced by a periodic series of resonators (so-called vanes) that correspond to a corrugated anode surface (Sec. III.E).

E. Influence of periodic anode resonator on stability properties

As indicated in Sec. III.D, for low-frequency perturbations about a tenuous electron layer with equilibrium profiles described by Eqs. (3.31)–(3.35), the extraordinary-mode eigenvalue equation (3.30) supports only stable oscillations when the electron layer is in contact with the cathode ($x_b^-=0$) and the anode is a smooth planar surface (Figs. 1 and 2). In this case, the dispersion relation (3.47) reduces to Eq. (3.53), which generally supports solutions with $\mathrm{Im}\omega=0$. In contrast, the possibility of instability exists when the planar anode is replaced by the periodic anode resonator illustrated in Fig. 13. Here, the electron layer is assumed to be in contact with the cathode ($x_b^-=0$); the outer edge of the electron layer is located at $x=x_b^+$; the anode surface closest to the cathode is located at $x=d$; the depth of each resonator vane is d_v; the vertical height (in the y direction) of each resonator is h_v; and the periodicity of the resonator structure in the y direction is L. In the presence of the periodic anode resonator in Fig. 13, the surface perturbation excited on the electron layer can experience an unstable coupling to the vacuum electromagnetic wave whose phase velocity is slowed by the resonator structure.

The eigenvalue equation (3.30) has been analyzed by Uhm *et al.* (1989) for the choice of equilibrium profiles in Eqs. (3.31)–(3.35) (with $x_b^-=0$), including the effects of the periodic anode resonator in Fig. 13. Specifically, the analysis assumes that the electromagnetic field amplitude within each resonator can be represented by the lowest-

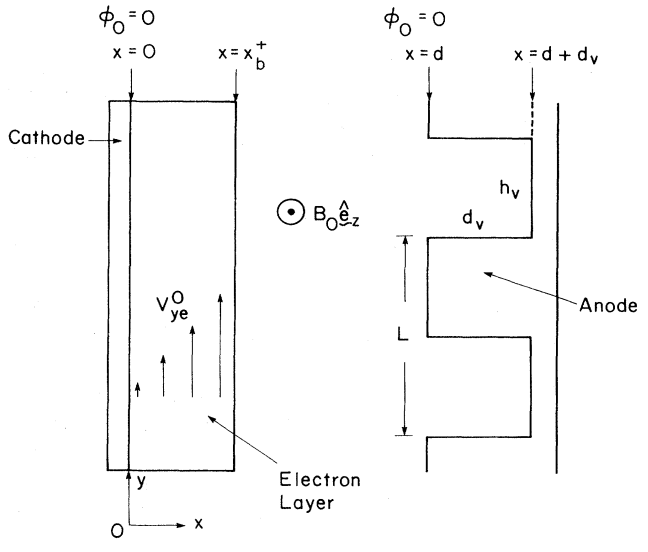

FIG. 13. Planar anode surface in Fig. 2, replaced with a periodic anode resonator. Here, the depth of each resonator vane is d_v, the vertical height (in the y direction) is h_v, and the periodicity of the resonator structure in the y direction is L.

order field pattern (Uhm *et al.*, 1989)

$$\delta E_y(x,y)=iB\sin[(\omega/c)(x-d-d_v)]\ ,$$
$$\delta B_z(x,y)=B\cos[(\omega/c)(x-d-d_v)]\ , \tag{3.54}$$

and $\delta E_x\simeq 0$ in the resonator regions $d<x<d+d_v$ and $nL-h_v/2<y<nL+h_v/2$, $n=0,\pm1,\pm2,\ldots$. Here, B is a constant amplitude. The eigenvalue equation (3.30) is then solved within the electron layer ($0\le x<x_b^+$) and in the vacuum region between the layer and closest anode surface ($x_b^+<x\le d$); the solution obtained in the region $x_b^+<x\le d$ is matched to the field pattern in Eq. (3.54) across the resonator openings at $x=d$. Without presenting algebraic details (Uhm *et al.*, 1989), the resulting dispersion relation can be expressed in the diagonal approximation as

$$k\frac{c\kappa}{\omega-kV_d}\left[1-\frac{V_d}{c}\frac{\omega}{ck}\right]=-\kappa_v(\omega)\frac{\cosh[\kappa_v(\omega)(d-x_b^+)]-g_v(\omega)\sinh[\kappa_v(\omega)d]\sinh[\kappa_v(\omega)x_b^+]}{\sinh[\kappa_v(\omega)(d-x_b^+)]+g_v(\omega)\sinh[\kappa_v(\omega)d]\cosh[\kappa_v(\omega)x_b^+]}-\kappa_b(\omega)\coth[\kappa_b(\omega)x_b^+]\ . \tag{3.55}$$

As in Sec. III.D, $\kappa_v(\omega)$ and $\kappa_b(\omega)$ are defined in Eq. (3.39), and $V_d=c\tanh\theta$, where $\theta=\kappa x_b^+$ and $\kappa=4\pi\hat{n}_e e/B_0$. Moreover, the effective admittance $g_v(\omega)$ of the resonator structure in Fig. 13 is defined by

$$g_v(\omega)=\frac{N_v(\omega)}{D_v(\omega)-N_v(\omega)}\ , \tag{3.56}$$

where

$$N_v(\omega)=-\frac{2\omega/\kappa_v(\omega)c}{\sinh[2\kappa_v(\omega)d]}\frac{\sin^2(kh_v/2)}{(kh_v/2)^2} \tag{3.57}$$

and

$$D_v(\omega)=\frac{L}{h_v}\cot\left[\frac{\omega d_v}{c}\right]-\sum_{j=-\infty}^{\infty}\frac{\omega}{\kappa_j(\omega)c}\coth[\kappa_j(\omega)d]\times\frac{\sin^2(k_jh_v/2)}{(k_jh_v/2)^2}\ . \tag{3.58}$$

In Eq. (3.58), $k_j=k+2\pi j/L$, where j is an integer, and $\kappa_j(\omega)$ is defined by $\kappa_j^2(\omega)=k_j^2-\omega^2/c^2$.

In the limit where the resonator depth approaches zero ($d_v\to 0$), the anode structure in Fig. 13 becomes a planar surface similar to that in Fig. 2. For $d_v\to 0$, it follows that $\cot(\omega d_v/c)\to\infty$ and $D_v(\omega)\to\infty$ in Eq. (3.58). Therefore, in the limit of a planar anode with $d_v\to 0$, the admittance of the resonator defined in Eq. (3.56) approaches $g_v(\omega)=0$. As expected, Eq. (3.55) then reduces to the dispersion relation (3.53) derived *ab initio* for a planar anode surface, which supports only stable oscillations with $\mathrm{Im}\omega=0$.

The dispersion relation (3.55) can be used to investigate detailed stability behavior for a wide range of values of the geometric parameters x_b^+/d, d_v/d, L/d, and h_v/L, and the flow parameter $\theta=\kappa x_b^+$, which measures the intensity of the electron layer. Generally speaking, for $g_v(\omega)\neq 0$, the dispersion relation (3.55) can support unstable solutions in which the surface perturbation on the electron layer couples to the vacuum electromagnetic wave whose phase velocity is slowed by the anode resonator structure in Fig. 13. Typical numerical solutions to Eq. (3.55) are illustrated in Fig. 14 (Uhm *et al.*, 1989). Here, the normalized real oscillation frequency $(\mathrm{Re}\omega)d/c$ and growth rate $(\mathrm{Im}\omega)d/c$ are plotted versus the normalized wave number kd, for the choice of system parameters $x_b^+/d=0.75$, $h_v/L=0.624$, $L/d=1.25$, several values of $\theta=\kappa x_b^+$, and two choices of the depth parameter d_v/d corresponding to $d_v/d=1.75$ [Fig. 14(a)] and $d_v/d=2.25$ [Fig. 14(b)]. Several points are noteworthy from Fig. 14. First, the bandwidth (in k space) of the instability increases significantly as θ is increased from $\theta=0.15$ to $\theta=0.45$. Second, the wave number corre-

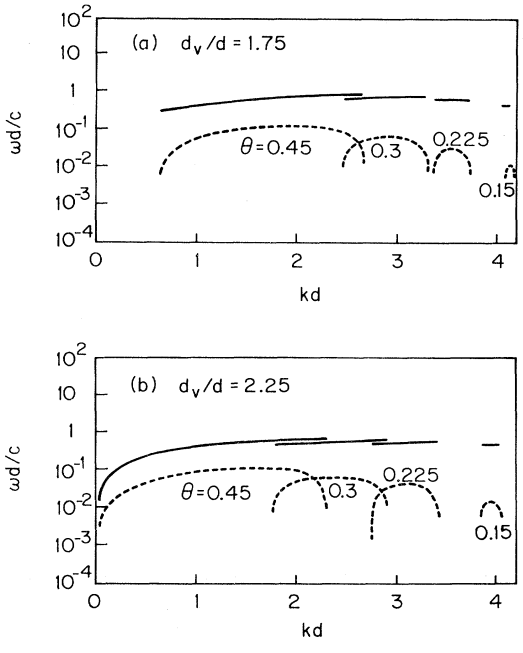

FIG. 14. Plots of the normalized real oscillation frequency $(\mathrm{Re}\omega)d/c$ (solid curves) and growth rate $(\mathrm{Im}\omega)d/c$ (dashed curves) vs the normalized wave number kd obtained numerically from the dispersion relation (3.55) for the choice of system parameters $x_b^+/d=0.75$, $h_v/L=0.624$, $L/d=1.25$, and several values of the flow parameter $\theta=\kappa x_b^+$. The two cases correspond to (a) $d_v/d=1.75$ and (b) $d_v/d=2.25$.

sponding to maximum growth rate shifts to smaller values as θ is increased and/or d_v/d is increased. As a final point (not illustrated in Fig. 14), the growth rate calculated numerically from Eq. (3.55) decreases to zero as the resonator depth $d_v \to 0$.

IV. EQUILIBRIUM AND STABILITY PROPERTIES FOR CYLINDRICAL ELECTRON FLOW

The equilibrium and stability analysis presented in Secs. II and III for planar electron flow (Figs. 1 and 2) can be extended in a relatively straightforward manner to cylindrical geometry (Fig. 15), including the full influence of cylindrical effects, such as finite diode and layer aspect ratios, Coriolis and centrifugal acceleration effects, discrete azimuthal mode numbers l, etc. (Chernin and Lau, 1984; Lau and Chernin, 1984; Davidson and Tsang, 1986). As a general remark, detailed properties of the magnetron and diocotron instabilities can exhibit a strong dependence on cylindrical effects, particularly at moderate values of $(r_b-a)/(b+a)$ and $(b-a)/(b+a)$. As illustrated in Fig. 15, the cathode and anode surfaces (assumed to be perfectly conducting cylinders) are located at $r=a$ and $r=b$, respectively; $r=r_b$ denotes the outer radius of the electron layer. In this section, we summarize briefly some of the key results obtained in cylindrical geometry, with particular emphasis on extending the planar treatment of the magnetron instability.

A. Equilibrium model

In cylindrical geometry (Fig. 15), we introduce cylindrical polar coordinates (r,θ,z) and unit vectors $\hat{\mathbf{e}}_r, \hat{\mathbf{e}}_\theta$, and $\hat{\mathbf{e}}_z$ in the radial, azimuthal, and axial directions, respectively. Under steady-state conditions ($\partial/\partial t=0$), it is assumed that $\partial/\partial\theta=0$ and $\partial/\partial z=0$, and that the equilibrium electron density profile $n_e^0(r)$ extends from the cathode ($r=a$) to some outer radius ($r=r_b<b$), where $r=(x^2+y^2)^{1/2}$ is the radial distance from the axis of symmetry in Fig. 15. In addition, the average flow velocity in the crossed electric and magnetic fields, $E_r(r)\hat{\mathbf{e}}_r$ and $B_z(r)\hat{\mathbf{e}}_z$, is in the azimuthal direction with $\mathbf{V}_e^0(\mathbf{x}) = V_{\theta e}^0(r)\hat{\mathbf{e}}_\theta$. Similar to Eqs. (2.2) and (2.3), space-charge-limited flow is assumed with boundary conditions

$$\phi_0(r=a)=0 \quad \text{and} \quad \phi_0(r=b)=V \ , \qquad E_r(r=a)=0 \ . \tag{4.1}$$

Here, $E_r(r)=-\partial\phi_0(r)/\partial r$ is the equilibrium radial electric field, and V is the applied voltage at the anode ($r=b$).

It is convenient to introduce the angular velocity of an electron fluid element defined by $\omega_{re}(r)=V_{\theta e}^0(r)/r$. Within the framework of a macroscopic cold-fluid model, radial force balance on a fluid element can then be expressed as

$$-\gamma_e^0(r)m_e\omega_{re}^2(r)r=-e\left[E_r(r)+\frac{\omega_{re}(r)r}{c}B_z(r)\right] \tag{4.2}$$

in the region where the electron density $n_e^0(r)$ is nonzero ($a\le r<r_b$). Here, $\gamma_e^0(r)$ is the relativistic mass factor defined by

$$\gamma_e^0(r)=[1-r^2\omega_{re}^2(r)/c^2]^{-1/2} \ . \tag{4.3}$$

Note that Eq. (4.2) is a statement of radial force balance on a fluid element between the (outward) centrifugal and electric forces and the (inward) magnetic force. Of course, Eq. (4.2) contains a centrifugal force term that is absent in the planar limit [compare with Eq. (2.4)]. For present purposes, we consider solutions to Eq. (4.2) with

$$\omega_{re}(r=a)=0 \tag{4.4}$$

at the cathode, which is consistent with $E_r(r=a)=0$ in Eq. (4.1). Therefore the centrifugal force term in Eq. (4.2) is expected to be largest at the outer edge of the selection layer ($r=r_b$). Evidently, the centrifugal force term in Eq. (4.2) can be neglected only in circumstances where $|\omega_{re}(r_b)| \ll eB_0/\gamma_e^0(r_b)m_ec$. Here, $B_0\hat{\mathbf{e}}_z$ is the axial magnetic field in the vacuum region ($r_b<r\le b$).

For axiumuthally symmetric equilibria, the steady-state Maxwell equations can be expressed as

$$\frac{1}{r}\frac{\partial}{\partial r}rE_r(r)=-4\pi en_e^0(r) \tag{4.5}$$

and

$$\frac{\partial}{\partial r}B_z(r)=\frac{1}{c}4\pi en_e^0(r)\omega_{re}(r)r \ . \tag{4.6}$$

Equations (4.5) and (4.6) are to be solved subject to the boundary conditions in Eqs. (4.1), as well as $B_z(r)=B_0=\text{const}$ in the vacuum region ($r_b<r\le b$).

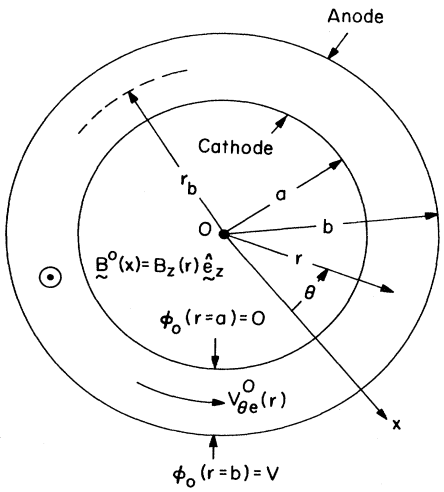

FIG. 15. Cylindrical cathode at $r=a$ and anode at $r=b$, assumed to be perfect conductors maintained at a potential difference V. The average electron flow velocity is $V_{\theta e}^0(r)\hat{\mathbf{e}}_\theta$ in the crossed electric and magnetic fields $E_r(r)\hat{\mathbf{e}}_r$ and $B_z(r)\hat{\mathbf{e}}_z$. The electron layer extends from $r=a$ to $r=r_b<b$.

Note that Eqs. (4.2), (4.5), and (4.6) constitute three coupled equations relating the four equilibrium profiles $\omega_{re}(r)$, $E_r(r)$, $B_z(r)$, and $n_e^0(r)$. Therefore the functional form of any one of the equilibrium profiles can be specified and the remaining three profiles calculated self-consistently from Eqs. (4.2), (4.5), and (4.6).

As a general remark, the centrifugal force term in Eq. (4.2) makes an equilibrium analysis of Eqs. (4.2), (4.5), and (4.6) for the case of cylindrical electron flow more difficult than an analysis of Eqs. (2.4), (2.6), and (2.7) for planar electron flow. In this regard, Eqs. (4.2), (4.5), and (4.6) have been solved numerically for a wide range of self-consistent equilibrium profiles (Davidson and Tsang, 1986; Tsang and Davidson, 1986), although the details will not be presented here. To illustrate the increased complexity in cylindrical geometry, let us assume that the functional form of the equilibrium density profile $n_e^0(r)$ is specified. Then, integrating Eqs. (4.5) and (4.6) for the field profiles $E_r(r)$ and $B_z(r)$, and substituting into the force balance equation (4.2) gives

$$-\frac{\omega_{re}^2(r)r}{[1-\omega_{re}^2(r)r^2/c^2]^{1/2}}=\frac{4\pi e^2}{m_e r}\int_a^r dr\, r n_e^0(r)-\frac{e\omega_{re}(r)r}{m_e c}\left[B_0-\frac{4\pi e}{c}\int_r^{r_b} dr\, r\omega_{re}(r)n_e^0(r)\right], \tag{4.7}$$

within the electron layer ($a \le r < r_b$). For specified density profile $n_e^0(r)$, Eq. (4.7) is a transcendental integral equation for the angular velocity profile $\omega_{re}(r)$, which must generally be solved numerically.

B. Extraordinary-mode eigenvalue equation

Similar to Sec. II.A, we make use of a macroscopic cold-fluid model to investigate the electromagnetic stability properties of magnetically insulated electron flow in the cylindrical geometry illustrated in Fig. 15. The present analysis assumes electromagnetic flute perturbations ($\partial/\partial z=0$) about general equilibrium profiles $\omega_{re}(r)$, $E_r(r)$, $B_z(r)$, and $n_e^0(r)$ consistent with Eqs. (4.2), (4.5), and (4.6) and the boundary conditions in Eqs. (4.1) and (4.4). In addition, the field perturbations are assumed to have extraordinary-mode polarization with

$$\begin{aligned}&\delta E(\mathbf{x},t)=\delta E_r(r,\theta,t)\hat{\mathbf{e}}_r+\delta E_\theta(r,\theta,t)\hat{\mathbf{e}}_\theta\ ,\\ &\delta B(\mathbf{x},t)=\delta B_z(r,\theta,t)\hat{\mathbf{e}}_z\ .\end{aligned} \tag{4.8}$$

The perturbed field components $\delta E_\theta(r,\theta,t)$, etc., are expressed as

$$\delta E_\theta(r,\theta,t)=\sum_{l=-\infty}^{\infty}\delta E_\theta^l(r)\exp(il\theta-i\omega t)\ , \tag{4.9}$$

where l is the azimuthal mode number and ω is the complex oscillation frequency, with $\mathrm{Im}\omega>0$ corresponding to instability.

The linearized Maxwell equations, together with the linearized cold-fluid equations of continuity and momentum transfer, give coupled equations for the perturbation amplitudes $\delta E_\theta^l(r)$, $\delta E_r^l(r)$, $\delta B_z^l(r)$, $\delta n_e^l(r)$, $\delta V_{re}^l(r)$, and $\delta V_{\theta e}^l(r)$. It is convenient to introduce the effective potential $\Phi_l(r)$ defined by

$$\Phi_l(r)=(ir/l)\delta E_\theta^l(r)\ , \tag{4.10}$$

which is the cylindrical generalization of Eq. (3.8). The linearized cold-fluid–Maxwell equations can be reduced to a single eigenvalue equation for $\Phi_l(r)$. Without presenting algebraic details (Davidson and Tsang, 1986), we obtain

$$\begin{aligned}&\frac{1}{r}\frac{\partial}{\partial r}\left[\frac{r}{[1-(\omega r/lc)^2]}[1+\chi_r(r,\omega)]\frac{\partial}{\partial r}\Phi_l(r)\right]-\frac{l^2}{r^2}[1+\chi_\theta(r,\omega)]\Phi_l(r)\\ &\quad=\frac{\Phi_l(r)}{(\omega-l\omega_{re})}\frac{l}{r}\frac{[1-(\omega_{re}r/c)(\omega r/lc)]}{[1-(\omega r/lc)^2]}\frac{\partial}{\partial r}\left[\frac{\omega_{pe}^2(r)[\omega_{ce}(r)-2\Omega_c(r)]}{\gamma_e^{02}(r)\nu_e^2(r,\omega)}\right].\end{aligned} \tag{4.11}$$

Here, $\omega_{ce}(r)$ and $\omega_{pe}(r)$ are the nonrelativistic electron cyclotron and plasma frequencies

$$\omega_{ce}(r)=\frac{eB_z(r)}{m_e c}\quad\text{and}\quad\omega_{pe}^2(r)=\frac{4\pi n_e^0(r)e^2}{m_e}\ ; \tag{4.12}$$

the effective Coriolis frequency $\Omega_c(r)$ is defined by

$$\Omega_c(r)=\tfrac{1}{2}\gamma_e^0(r)\omega_{re}(r)[1+\gamma_e^{02}(r)]\ . \tag{4.13}$$

Moreover, the radial and azimuthal susceptibilities occurring in Eq. (4.11) are defined by

$$\chi_r(r,\omega)=-\left[1-\left[\frac{\omega_{re}r}{c}\right]\left[\frac{\omega r}{lc}\right]\right]\frac{\omega_{pe}^2(r)\gamma_e^0(r)}{[1-(\omega r/lc)^2]\nu_e^2(r,\omega)}, \tag{4.14}$$

$$\begin{aligned}\chi_\theta(r,\omega)=&-\frac{\omega_{pe}^2(r)}{\gamma_e^0(r)\nu_e^2(r,\omega)}\left[1+\frac{\omega_{pe}^2(r)r^2/\gamma_e^0(r)l^2c^2}{1-(\omega r/lc)^2}\right]\\ &+\frac{[\omega_{ce}(r)-2\Omega_c(r)]}{l\omega}\\ &\times\frac{\omega_{pe}^2(r)}{\gamma_e^{02}(r)\nu_e^2(r,\omega)}\frac{2(\omega r/lc)^2}{[1-(\omega r/lc)^2]^2}\ ,\end{aligned} \tag{4.15}$$

where

$$\nu_e^2(r,\omega)=\gamma_e^{02}(r)(\omega-l\omega_{re})^2\left[1+\frac{\omega_{pe}^2(r)r^2/\gamma_e^0(r)l^2c^2}{1-(\omega r/lc)^2}\right] - \frac{[\omega_{ce}(r)-2\Omega_c(r)]}{\gamma_e^{02}(r)} \times\left[\omega_{ce}(r)-\frac{1}{r}\frac{\partial}{\partial r}(\gamma_e^0 r^2\omega_{re})\right] . \quad (4.16)$$

The eigenvalue equation (4.11) is to be solved subject to the boundary conditions $\delta E_\theta^l(r=a)=0=\delta E_\theta^l(r=b)$ at the cathode and anode, or equivalently,

$$\Phi_l(r=a)=0=\Phi_l(r=b) . \quad (4.17)$$

To summarize, the eigenvalue equation (4.11) can be used to determine (numerically) the eigenfunction $\Phi_l(r)$ and the complex oscillation frequency ω for a wide range of cylindrical equilibrium profiles $E_r(r)$, $B_z(r)$, $n_e^0(r)$, and $\omega_{re}(r)$ consistent with Eqs. (4.2), (4.5), and (4.6). In addition, it is straightforward to show that the cylindrical results in Eq. (4.11) and Eqs. (4.14)–(4.16) reduce directly to Eqs. (3.13)–(3.16) in the appropriate planar limit with

$$\frac{l}{r}\to k,\ \frac{\omega r}{lc}\to\frac{\omega}{ck},\ \frac{\omega_{pe}^2 r^2}{l^2c^2}\to\frac{\omega_{pe}^2}{c^2k^2} , \quad (4.18)$$

$$\frac{\omega_{re}r}{c}\to\frac{V_{ye}^0(x)}{c},\ l\omega_{re}\to kV_{ye}^0(x),\ \omega_{re}\to\frac{V_{ye}^0(x)}{r}\to 0 .$$

A planar description is expected to provide a good approximation whenever $(b+a)/(b-a)\gg 1$ in Fig. 15.

C. Influence of cylindrical effects on the magnetron instability

For present purposes, we illustrate the influence of cylindrical effects on the magnetron instability for the case in which the equilibrium radial electric field $E_r(r)$ is assumed to have the form

$$E_r(r)=\begin{cases} -B_0\dfrac{\sinh[\kappa(r-a)]}{\cosh[\kappa(r_b-a)]}, & a\le r<r_b , \\ -B_0\tanh[\kappa(r_b-a)]\dfrac{r_b}{r}, & r_b<r\le b . \end{cases} \quad (4.19)$$

Here, κ is a constant and $B_0=B_z(r=r_b)$ is the axial magnetic field in the vacuum region outside the electron layer $(r_b<r\le b)$. The corresponding profiles for $n_e^0(r)$, $B_z(r)$, and $\omega_{re}(r)$ can be calculated self-consistently from Eqs. (4.2), (4.5), and (4.6). In addition, we make use of $E_r(r)=-\partial\phi_0/\partial r$ and integrate Eq. (4.19) from $r=a$ to $r=b$. Enforcing $\phi_0(r=b)=V$ then gives

$$\frac{eV}{m_ec^2}=\frac{\omega_{p0}^2}{c^2\kappa^2}\left[\cosh[\kappa(r_b-a)]-1+(1+A)\kappa(r_b-a) \times\sinh[\kappa(r_b-a)]\ln\left[\frac{bA}{a(1+A)}\right]\right] . \quad (4.20)$$

In Eq. (4.20), V is the applied voltage, $\omega_{p0}\equiv[4\pi n_e^0(r=a)e^2/m_e]^{1/2}$ is the nonrelativistic electron plasma frequency at the cathode, and

$$A=a/(r_b-a) \quad (4.21)$$

is a measure of the aspect ratio of the electron layer (see Fig. 15). Other important dimensionless parameters that characterize the equilibrium are $\kappa(r_b-a)$, $\omega_{c0}(r_b-a)/c$, $(b-a)/(r_b-a)$, and

$$s_0=\omega_{p0}^2/\omega_{c0}^2 , \quad (4.22)$$

where $\omega_{c0}=eB_0/m_ec$ is the nonrelativistic electron cyclotron frequency in the vacuum magnetic field B_0. Note that $s_0=4\pi n_e^0(r=a)m_ec^2/B_0^2$ is proportional to the electron density at the cathode. Substituting Eq. (4.19) into Poisson's equation (4.5) and evaluating at $r=a$ gives

$$s_0\frac{\omega_{c0}(r_b-a)}{c}=\frac{\kappa(r_b-a)}{\cosh[\kappa(r_b-a)]} , \quad (4.23)$$

which relates the dimensionless parameters s_0, $\omega_{c0}(r_b-a)/c$, and $\kappa(r_b-a)$.

For equilibrium profiles consistent with Eqs. (4.2), (4.5), (4.6), and (4.19), the extraordinary-mode eigenvalue equation (4.11) has been solved numerically (Davidson and Tsang, 1986) to determine detailed properties of the magnetron instability for a wide range of system parameters $A=a/(r_b-a)$, $s_0=\omega_{p0}^2/\omega_{c0}^2$, $\kappa(r_b-a)$, eV/m_ec^2, etc. Typical results are summarized in Figs. 16–18 (Davidson and Tsang, 1986).

To illustrate the dependence of stability properties on

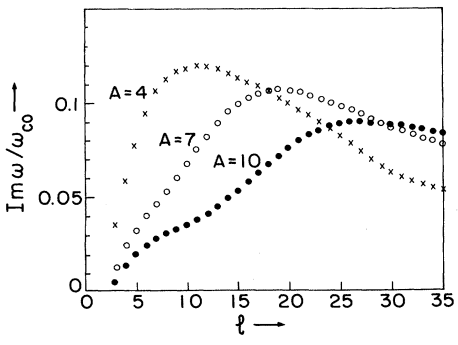

FIG. 16. Plots of $\mathrm{Im}\omega/\omega_{c0}$ vs azimuthal mode number obtained from Eq. (4.11) for $\kappa(r_b-a)=0.6931$, $(b-a)=1.5(r_b-a)$, $s_0=0.4$, $\omega_{c0}(r_b-a)/c=1.386$, and several values of layer aspect ratio $A=a/(r_b-a)$ corresponding to $A=4$ and $eV/m_ec^2=0.796$; $A=7$ and $eV/m_ec^2=0.803$; and $A=10$ and $eV/m_ec^2=0.807$.

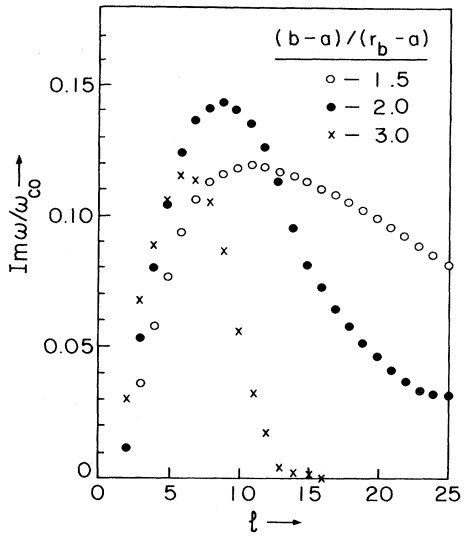

FIG. 17. Plots of $\mathrm{Im}\omega/\omega_{c0}$ vs azimuthal mode number obtained from Eq. (4.11) for $\kappa(r_b-a)=0.6931$, $s_0=0.4$, $\omega_{c0}(r_b-a)/c=1.386$, $A=a/(r_b-a)=4$, and several values of $(b-a)/(r_b-a)=\eta$ corresponding to $\eta=1.5$ and $eV/m_ec^2=0.796$; $\eta=2.0$ and $eV/m_ec^2=1.158$; and $\eta=3.0$ and $eV/m_ec^2=1.799$.

layer aspect ratio $A=a/(r_b-a)$, plots are shown in Fig. 16 of the normalized growth rate $\mathrm{Im}\omega/\omega_{c0}$ versus azimuthal mode number l for $A=4$, 7, and 10. Specifically, in Fig. 16, the layer thickness r_b-a, the cathode electron density $n_b^0(r=a)$, the applied (vacuum) magnetic field B_0, and the anode-cathode spacing $b-a$ are held fixed with $\kappa(r_b-a)=0.6931$, $s_0=0.4$, $\omega_{c0}(r_b-a)/c=1.386$, and $(b-a)=1.5(r_b-a)$. Moreover, in Fig. 16, the layer aspect ratio $A=a/(r_b-a)$ is increased from $A=4$ to $A=7$ to $A=10$ by increasing the cathode radius a. It is evident from Fig. 16 that the growth rate $\mathrm{Im}\omega$ exhibits a sensitive dependence on the layer aspect ratio A. In particular, as A is increased from $A=4$ to $A=10$, there is a decrease in the maximum growth rate. Furthermore, as A is increased from $A=4$ to $A=10$, it is clear from Fig. 16 that there is a shift in the growth rate spectrum to shorter azimuthal wavelengths (higher l values). In Fig. 16, the normalized diode voltage eV/m_ec^2 has been adjusted for each value of A to be consistent with Eq. (4.20).

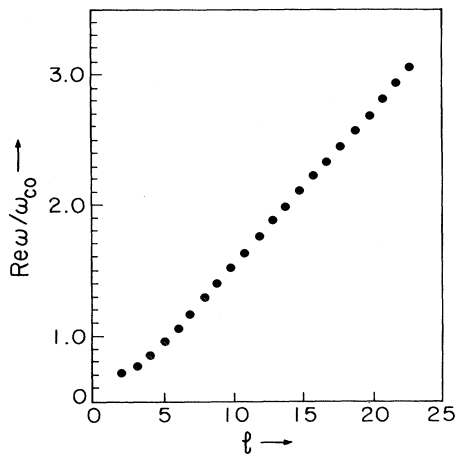

FIG. 18. Plot of $\mathrm{Re}\omega/\omega_{c0}$ vs azimuthal mode number obtained from Eq. (4.11) for $\kappa(r_b-a)=0.6931$, $s_0=0.4$, $A=a/(r_b-a)=4$, $\omega_{c0}(r_b-a)/c=1.386$, $(b-a)=2(r_b-a)$, and $eV/m_ec^2=1.158$. (See also Fig. 17.)

Detailed stability properties also exhibit a sensitive dependence on anode-cathode spacing, $b-a$, relative to the layer thickness, r_b-a. This is illustrated in Fig. 17, where $\mathrm{Im}\omega/\omega_{c0}$ is plotted versus azimuthal mode number l for fixed values of $\kappa(r_b-a)=0.6931$, $s_0=0.4$, $\omega_{c0}(r_b-a)/c=1.386$, layer aspect ratio $a/(r_b-a)=4$, and several values of $(b-a)/(r_b-a)=A(b-a)/a$ corresponding to 1.5, 2.0, and 3.0. In effect, in Fig. 17, the layer thickness r_b-a, applied (vacuum) magnetic field B_0, cathode electron density $n_b^0(r=a)$, etc., have been held fixed, and the normalized width of the vacuum region

$$\frac{b-r_b}{r_b-a}=\frac{b-a}{r_b-a}-1 \tag{4.24}$$

is increased from $(b-r_b)/(r_b-a)=1/2$ to 1.0 to 2.0. The resulting dependence of the growth rate $\mathrm{Im}\omega$ on the width of the vacuum region is evident from Fig. 17. In particular, there is a significant decrease in the instability bandwidth as $(b-a)/(r_b-a)$ is increased from 1.5 to 3.0 in Fig. 17, with a concomitant shift to lower l values. In Fig. 17, the normalized diode voltage eV/m_ec^2 has been adjusted for each set of parameters to be consistent with Eq. (4.20).

Finally, for $(b-a)=2.0(r_b-a)$ and parameters otherwise identical to Fig. 17, Fig. 18 shows a plot of the normalized real frequency $\mathrm{Re}\omega/\omega_{c0}$ versus azimuthal mode number l. As in the planar case [see, for example, Fig. 7(b)], it is found that the real oscillation frequency in Fig. 18 increases approximately linearly over the range of unstable l values.

To summarize, for prescribed equilibrium profiles, the extraordinary-mode eigenvalue equation (4.11) can be solved numerically for the eigenfunction $\Phi_l(r)$ and complex eigenfrequency ω over a wide range of system parameters. As a general remark, the numerical results show that detailed stability properties exhibit a sensitive dependence on cylindrical effects. For example, at low values of the mode number l, the properties of the eigenfunction $\Phi_l(r)$ are qualitatively different from the planar case, and from the cylindrical case for large l values. Furthermore, it is found that the instability growth rate $\mathrm{Im}\omega$ exhibits a sensitive dependence on the layer aspect ratio $A=a/(r_b-a)$, the normalized anode-cathode spacing $(b-a)/(r_b-a)$, etc., particularly when the electron flow is relativistic and centrifugal effects play an important role in modifying the equilibrium profiles.

V. RELATIVISTIC MAGNETRONS

In conventional magnetrons, voltages of a few hundred volts to tens of kilovolts are applied between the anode and a heated, thermionic cathode (Slater, 1969). Power levels from tens of watts to hundreds of kilowatts can be achieved in the decimeter and centimeter wavelength range with conversion efficiencies as high as 80%. In relativistic magnetrons, however, pulsed high-voltage diodes (operating in the several hundred kV to MV range, say) are used to generate microwaves at gigawatt power levels, although at reduced efficiencies (Bekefi and Orzechowski, 1976; Orzechowski and Bekefi, 1979; Palevsky and Bekefi, 1979; Gleizer *et al.*, 1980: Benford, 1987; Nokonov *et al.*, 1987; Benford *et al.*, 1989). In this section, we present a brief summary of the classic experiments by Palevsky and Bekefi (1979) on the so-called $A6$ relativistic magnetron (Sec. V.A). Recent particle-in-cell computer simulations (Chan *et al.*, 1990) of this magnetron configuration are then described (Sec. V.B).

A. Multiresonator magnetron experiments

Figure 19(a) shows a schematic of the cross section of the $A6$ magnetron (Palevsky and Bekefi, 1979). The cold, field-emission, graphite cathode is located at radius $a=1.58$ cm. The inside radius of the anode block is $b=2.11$ cm, and six vane-type resonators with outer radius $d=4.11$ cm are used, with angle $\psi=20°$ subtended by the resonators on axis. The axial magnetic field $B_f\hat{\mathbf{e}}_z$ prior to formation of the circulating electron layer (the so-called fill field in Sec. II.B) ranges from 4 to 10 kG in typical operation. The length of the anode block for the $A6$ magnetron is $L=7.2$ cm, and the operating voltage in the experiments is 300–400 kV. The annular interaction space between $r=a$ and $r=b$, together with the periodically spaced vanes, can be viewed as a coaxial microwave resonator. For transverse electric (TE) modes with δE perpendicular to $B_f\hat{\mathbf{e}}_z$ and δB parallel to $B_f\hat{\mathbf{e}}_z$, the vacuum electric-field pattern is illustrated in Fig. 19(b) for the $l=3$ and $l=6$ modes (the so-called π and 2π modes, respectively). The circular dashed lines in Fig. 19(b) show schematically the outer radial boundary of the electron layer prior to the onset of electromagnetic fluctuations. The $A6$ magnetron is found to oscillate preferentially in the 2π mode, which is characterized by the fact that the electromagnetic fields in all of the resonators are precisely in phase [Fig. 19(b)].

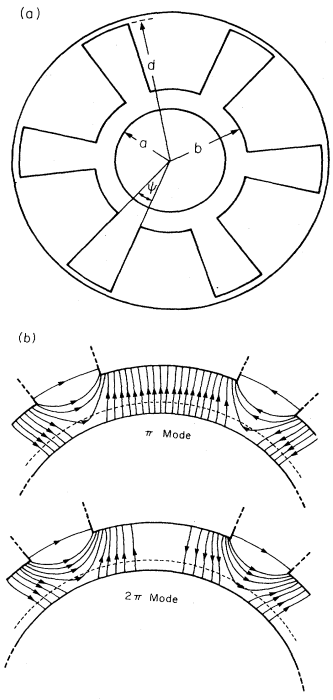

FIG. 19. Schematic of the $A6$ relativistic magnetron (Palevsky and Bekefi, 1979): (a) emitting cathode located at $a=1.58$ cm with anode located at $b=2.11$ cm; six vane-type resonators with outer radius $d=4.11$ cm subtend an angle of $\psi=20°$ at the axis; and the fill field $B_f\hat{\mathbf{e}}_z$ points into the page; (b) vacuum electric-field pattern for the so-called π and 2π modes of excitation. The outer radial boundary of the electron layer is indicated by the dashed curves.

Assuming applicability of the Brillouin flow model for magnetically insulated electron flow (see Sec. II.B), the cylindrical generalization of the Hull cutoff voltage V_H and the Buneman-Hartree threshold voltage $V_{\rm BH}$ can be expressed relativistically as (Lovelace and Young, 1985; Lau, 1987; Davidson, 1990)

$$\frac{eV_H}{m_ec^2}=\left[1+\frac{e^2B_f^2}{m_e^2c^4}\left[\frac{b^2-a^2}{2b}\right]^2\right]^{1/2}-1 \tag{5.1}$$

and

$$\frac{eV_{\rm BH}}{m_ec^2}=\frac{eB_f}{m_ec^2}\left[\frac{b^2-a^2}{2b}\right]\beta_p-[1-(1-\beta_p^2)^{1/2}]\,, \tag{5.2}$$

where β_p is the normalized phase velocity of the electromagnetic wave. Note that Eqs. (5.1) and (5.2) are identical in form to the planar expressions derived in Sec. II.B, provided we make the replacement $d\rightarrow(b^2-a^2)/2b$ in Eqs. (2.27) and (2.30), respectively. For steady Brillouin flow in a cylindrical diode with specified fill field B_f the inequality $V<V_H$ is required to ensure magnetic insulation of the electron flow from contact with the anode at $r=b$, whereas $V>V_{\rm BH}$ is required for interaction of the outermost electrons with the wave fields.

The region of experimental operation of the $A6$ magnetron is illustrated by the dashed line in Fig. 20(a), with the point corresponding to maximum microwave power (Palevsky and Bekefi, 1979). Here, the voltages V_H and $V_{\rm BH}$, calculated from Eqs. (5.1) and (5.2), are plotted versus the applied magnetic field B_f, and $V_{\rm BH}$ has been evaluated for β_p corresponding to the $l=6$ mode (2π mode) at frequency $f=\omega/2\pi=4.55$ GHz. The measured microwave power (Palevsky and Bekefi, 1979) emitted by the $A6$ magnetron is plotted versus the fill field B_f

in Fig. 20(b), where the maximum power at 7.6 kG is approximately 450 MW. Note from Fig. 20(b) that microwave emission occurs for magnetic field in the interval $4.2\ \text{kG} < B_f < 10.4\ \text{kG}$. On the other hand, the intersection points of the dashed line in Fig. 20(a) with the two curves corresponding to V_H and V_{BH} would predict that microwave emission occurs in the interval $4.9\ \text{kG} < B_f < 8.8\ \text{kG}$. Even though the vane structure was neglected in the derivation of the expressions for V_H and V_{BH} in Eqs. (5.1) and (5.2), and the numerical simulations (Chan *et al.*, 1990) of the $A6$ magnetron presented in Sec. V.B indicate that the Brillouin flow model does not accurately describe the simulation profiles (even at early times), the agreement between experiment and the operating range predicted by theory based on the Brillouin flow model is remarkably good.

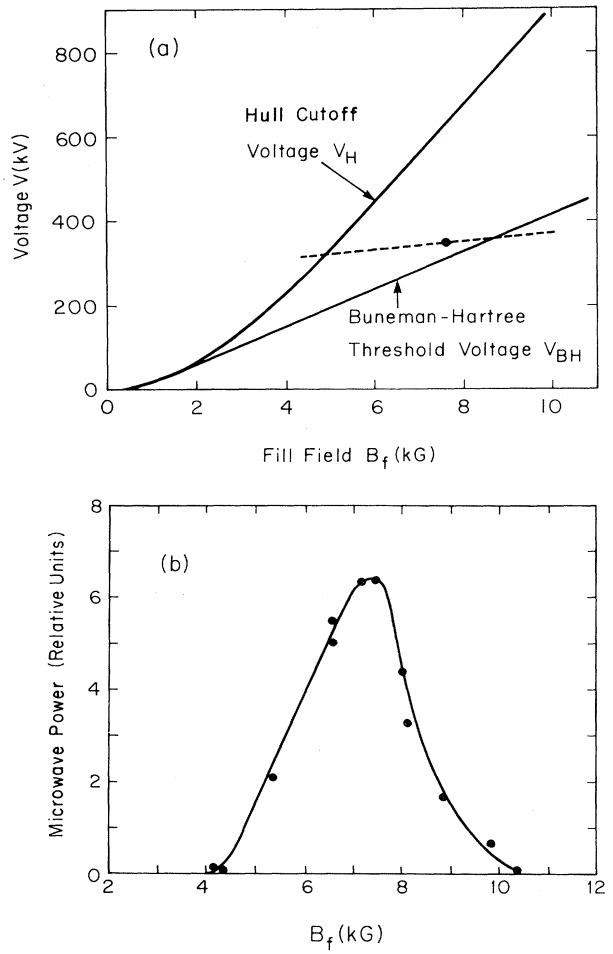

FIG. 20. Microwave generation by the $A6$ relativistic magnetron (Palevsky and Bekefi, 1979). The dashed line in (a) corresponds to the region of experimental operation, and the solid point corresponds to the maximum microwave power. The measured microwave power is plotted vs the applied magnetic field B_f in (b), where the peak rms power is ~ 0.45 GW at $B_f = 7.6$ kG.

B. Numerical simulation studies

Although magnetrons are widely used as microwave sources, a fundamental understanding of the underlying interaction physics is still being developed, particularly in the nonlinear regime (Lau, 1987). Magnetron design relies largely on two criteria—the Hull cutoff condition ($V < V_H$) for magnetic insulation of the electron layer, and the Buneman-Hartree threshold condition ($V > V_{BH}$) for the onset of magnetron oscillations. Much of the theoretical challenge in describing magnetron operation arises from the complexity introduced by the corrugated anode boundary and the fact that the electrons emitted from the cathode interact with the electromagnetic waves in the anode-cathode gap in a highly nonlinear way. This is manifest through strong azimuthal bunching of the electrons and the formation of large-amplitude "spokes" in the circulating electron density. In this regard, computer simulation studies (Yu, Kooyers, and Buneman, 1965; Palevsky, Bekefi, and Drobot, 1981; Palevsky *et al.*, 1981; Chan *et al.*, 1990) provide a particularly valuable approach to the analysis of the interaction physics and nonlinear electrodynamics in magnetrons.

In this section, we summarize recent computer simulations (Chan *et al.*, 1990) of the multiresonator $A6$ magnetron configuration (Palevsky and Bekefi, 1979) using the two-dimensional ($\partial/\partial z = 0$) particle-in-cell code MAGIC[1] (Goplen and McDonald, 1989). The code includes cylindrical effects, and relativistic and electromagnetic effects in a fully self-consistent manner. Unlike earlier computer simulations (Yu, Kooyers, and Buneman, 1965; Palevsky, Bekefi, and Drobot, 1981), the magnetron oscillations are excited from noise, i.e., without preinjection of a finite-amplitude rf signal or preferential excitation of 2π-mode or π-mode oscillations.

In the simulations (Chan *et al.*, 1990), Maxwell's equations and the particle orbit equations are solved relativistically and electromagnetically, using (typically) more than 3000 macroparticles and a nonuniform, two-dimensional grid consisting of approximately 3000 cells. In addition, the simulations assume one open resonator, which is modeled by a dispersive window placed along the dashed line in Fig. 21 at $r = d = 4.11$ cm. At the window, the boundary condition is such that most of the electromagnetic wave energy is absorbed by the window, while a small fraction of the wave energy is reflected back into the cavity. Such a window yields a finite Q factor for the system. The rf power delivered to the window (i.e., the rf power output) is given by the net flow of electromagnetic energy expressed as an area integral of the Poynting flux over the window surface. A radially nonuniform grid is used to resolve small-scale variations

[1]The MAGIC simulation code was developed by researchers at Mission Research Corporation. The simulation results presented in this paper use the code version dated 1988.

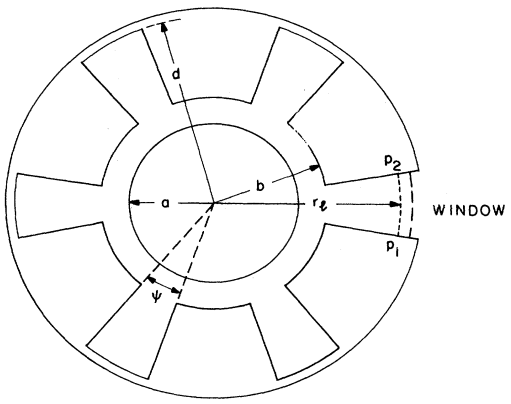

FIG. 21. Schematic of the *A*6 magnetron used in the computer simulations. The rf power is partially absorbed by the output window (dashed line) located at $r=d=4.11$ cm in the open resonator. Here, $a=1.58$ cm, $b=2.11$ cm, $d=4.11$ cm, and $\psi=20°$.

in particle velocities and positions and in field quantities, particularly in the interaction region ($a \le r \le b$). The electron emission and absorption processes in the simulations can be summarized as follows. The electrons are emitted from the cathode through a space-charge-limited emission process in which the instantaneous electric field normal to the cathode surface vanishes (at $r=a=2.11$ cm). On the other hand, electrons are absorbed by the anode or cathode whenever they strike the anode or cathode surface. Here, both the anode and cathode are treated as perfect conductors.

Another important aspect of the simulation model (Chan *et al.*, 1990) concerns the propagation of the high-voltage pulse from the power supply to the magnetron diode. Because the voltage pulse rises slowly compared with the electron cyclotron period and the rf oscillation period, the magnetic field induced by the voltage pulse is neglected. Therefore a quasistatic model is used to describe the high-voltage pulse applied to the magnetron diode. In such a model, the diode voltage is given by $V_D(t)=Z(t)V_0(t)/[Z_0+Z(t)]$, where $V_0(t)$ is the voltage pulse provided by the power supply, and $Z_0=$const and $Z(t)$ are the power supply impedance and the magnetron impedance, respectively. Here, the magnetron impedance $Z(t)$ and the diode voltage $V_D(t)$ are determined self-consistently in the simulations. For an ideal power supply ($Z_0=0$), the diode voltage is given by $V_D(t)=V_0(t)$. In the simulations, the voltage pulse $V_0(t)$ is assumed to have the form

$$V_0(t)=\begin{cases}0, & t<0\ , \\ (t/t_0)V_m, & 0\le t<t_0\ , \\ V_m, & t\ge t_0\ ,\end{cases} \tag{5.3}$$

where t_0 and V_m are the rise time and maximum value of the voltage pulse, respectively. The rise time assumed in the simulations is $t_0=4.0$ ns, corresponding to the experimental value (Palevsky and Bekefi, 1979). Although the applied high-voltage pulse is described approximately by Eq. (5.3), it should be emphasized that all extraordinary-mode rf excitations ($\delta\mathbf{B}=\delta B_z\hat{\mathbf{e}}_z$ and $\delta\mathbf{E}=\delta E_r\hat{\mathbf{e}}_r+\delta E_\theta\hat{\mathbf{e}}_\theta$) are treated fully electromagnetically in the simulations. Typical numerical results (Chan *et al.*, 1990) are presented in Figs. 22–25 for the ideal case in which the external power supply has zero impedance ($Z_0=0$).

Figure 22 shows the time history of the integrated rf field profile $V_\theta(t)=\int_{P_1}^{P_2}d\theta\, r_l\delta E_\theta(r_l,\theta,t)$ and the magni-

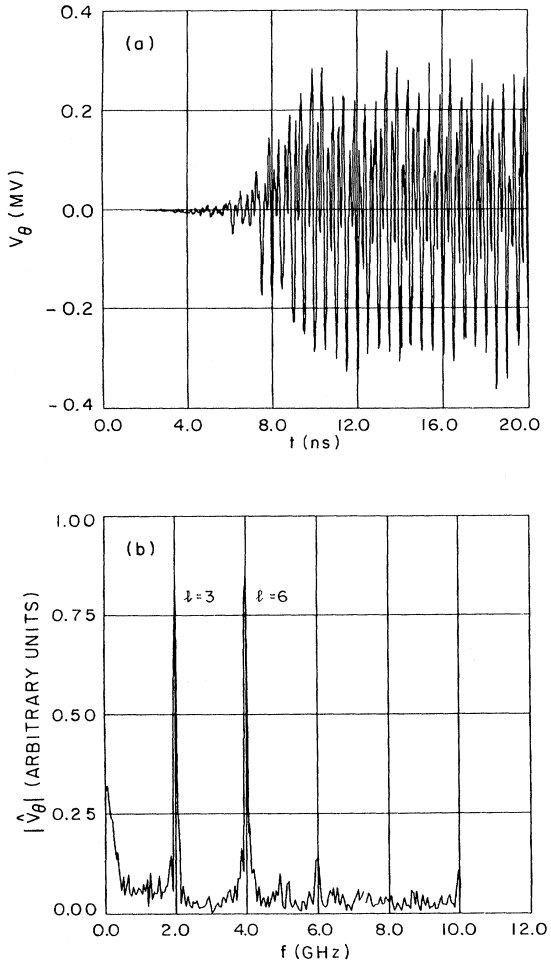

FIG. 22. (a) time history of the integrated rf field profile

$$V_\theta(t)=\int_{P_1}^{P_2}d\theta\, r_l\delta E_\theta(r_l,\theta,t)$$

obtained in the simulations at radius $r=r_l=3.7$ cm in the open resonator for the choice of system parameters $B_f=7.2$ kG, $V_m=350$ kV, $t_0=4.0$ ns, and $Z_0=0$; (b) Fourier spectrum $|\hat{V}_\theta(f)|$ of the signal in (a). The two distinct peaks at $f=2.0$ GHz and $f=4.0$ GHz correspond to π-mode ($l=3$) and 2π-mode ($l=6$) oscillations, respectively.

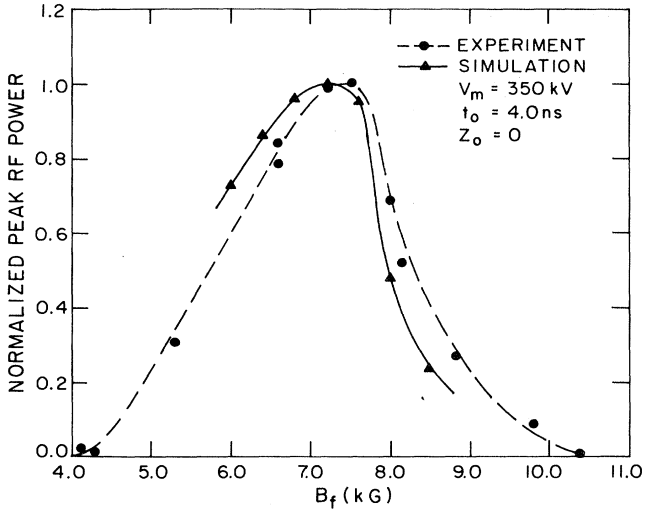

FIG. 23. Plots of the normalized rf power vs the applied magnetic field B_f. The dots correspond to the experimental results (Palevsky and Bekefi, 1979), and the triangles correspond to the simulation results for $V_m=350$ kV, $t_0=4.0$ ns, and $Z_0=0$. The maximum value of the rf power is 0.45 GW in the experiment and 0.3 GW in the simulations.

tude of the Fourier transform of $V_\theta(t)$, denoted by $|\hat{V}_\theta(f)|$, for the choice of system parameters $B_f=7.2$ kG, $V_m=350$ kV, and $t_0=4.0$ ns. Here, the integration path corresponds to the dotted line in Fig. 21 from P_1 to P_2 at $r=r_l=3.7$ cm. In Fig. 22(a), the nonlinear saturation of the magnetron oscillations occurs at $t\simeq 10$ ns,

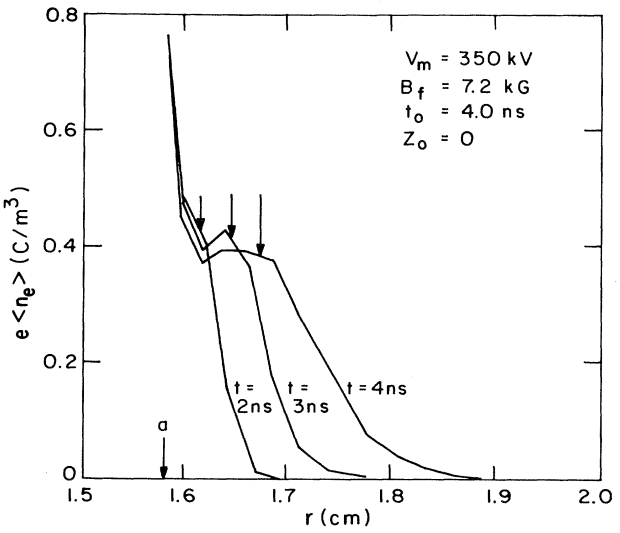

FIG. 24. Plots of the azimuthally averaged charge density $e\langle n_e\rangle(r,t)$ vs radial distance r obtained in the simulations at times $t=2.0$, 3.0, 4.0 ns for the same system parameters as in Fig. 22. Here, the arrows designate the location of the outer envelope ($r=r_b$) of the electron layer calculated from a simple Brillouin flow model. The average density profiles obtained in the simulations differ substantially from Brillouin flow conditions.

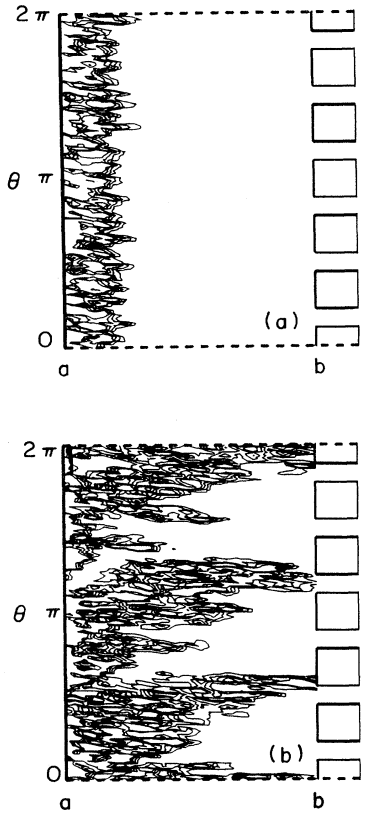

FIG. 25. Density contour plots for $n_e(r,\theta,t)$ obtained in the simulations at (a) $t=3.0$ ns and (b) $t=8.0$ ns for the same system parameters as in Fig. 22.

where the ratio of the saturated amplitude $V_{\theta s}$ and the applied diode voltage $V_D=V_m$ is $V_{\theta s}/V_D\simeq 0.85$. In Fig. 22(b), the two distinct peaks at the frequencies $f=2.0$ GHz and $f=4.0$ GHz correspond to π-mode and 2π-mode oscillations, respectively. The 2π-mode oscillation frequency $f=4.0$ GHz is 14% lower than the frequency $f=4.55$ GHz observed in the experiment (Palevsky and Bekefi, 1979), which may be due in part to the absence of finite-axial-length effects in the simulations (which assume $\partial/\partial z=0$). For example, if axial mode number $n=1$ is assumed, then a simple estimate of the (corrected) 2π-mode oscillation frequency would be $f_1=f[1+(c/2Lf)^2]^{1/2}$. Substituting $f=4.0$ GHz and $L=7.2$ cm then gives $f_1=4.5$ GHz.

By evaluating the area-integral of the outward Poynting flux $(c/4\pi)\delta E_\theta \delta B_z$ over the surface of the output window at $r=d=4.11$ cm in Fig. 21, the rf power output in the simulations is calculated for various values of the applied magnetic field B_f. The magnetic-field dependence of the normalized rf power is shown in Fig. 23. Here, the dots correspond to the experimental values, and the triangles are obtained from the simulations with $Z_0=0$. In Fig. 23, the normalization is chosen such that the maximum values of the rf power in the simulations and in the experiment are equal to unity. The actual values of the maximum rf output per unit axial length in

the simulations is 4.3 GW/m (Chan *et al.*, 1990). For the $A6$ magnetron, which has an axial length $L=7.2$ cm, this corresponds to $P=0.3$ GW, which is somewhat less than the maximum rf power $P=0.45$ GW measured in the experiment (Palevsky and Bekefi, 1979). (The values of power quoted here are rms values.) Apart from a constant scale factor between the rf powers measured in the experiments and in the simulations, it is evident from Fig. 23 that the dependence of the rf power on applied magnetic field obtained in the simulations is in very good agreement with the experimental results. The difference in scale factor may be due to the fact that a larger fraction of the rf power in the simulations is reflected back into the cavity, and the effective Q value in the simulations ($Q\sim 100$) is greater than that in the experiment ($Q\sim 20$–40). As the applied magnetic field B_f is decreased, crossing the Hull cutoff curve at the diode voltage corresponding to $V_D=350$ kV, it is found that the $5\pi/3$ mode ($l=5$) becomes the dominant rf excitation in the simulations.

Figure 24 shows radial plots of the charge density, $e\langle n_e\rangle(r,t)=(1/2\pi)\int_0^{2\pi} e n_e(r,\theta,t)d\theta$, averaged over the azimuthal angle θ, at several instants of time for the same values of system parameters as in Fig. 22. In Fig. 24, the outer radius of the electron layer [$r=r_b(t)$], designated by the arrows, is calculated from a simple Brillouin flow model (see Sec. II.B) for $B_f=7.2$ kG and diode voltages $V_D(t)=0.5V_m$, $0.75V_m$, $1.0V_m$, corresponding to $t=2.0$, 3.0, 4.0 ns. It is clear from Fig. 24 that a substantial fraction of the electrons occupy the region between $r=r_b$ and the anode ($r=b$). The existence of a long tail in the electron density profile indicates that the electron flow is significantly different from the ideal Brillouin flow model (Davidson, 1990). For the $A6$ magnetron operating at $V_m\simeq 350$ kV, cylindrical and relativistic effects are relatively mild. For example, at $t=t_0=4.0$ ns, the layer aspect ratio is $A=a/(r_b-a)\simeq 15$, and the relativistic mass factor at $r=r_b$ is $\gamma_e^0(r_b)\simeq 1.15$. We define the local self-field parameter $s_e(r)$ by

$$s_e(r)=\frac{\omega_{pe}^2(r)/\gamma_e^0(r)}{\omega_{ce}^2(r)/\gamma_e^{02}(r)} . \tag{5.4}$$

Note from Eqs. (2.13) and (5.4) that $s_e=1$ under ideal Brillouin flow conditions (in the planar approximation). In the simulations, however, it is found that $s_e(r)$ decreases considerably as r increases from $r=a$ to $r=r_b$ and beyond. For example, at $t=t_0=4.0$ ns in Fig. 24, the self-field parameter decreases from $s_e(r=a)\simeq 1$ at the cathode to $s_e(r=r_b)\simeq 0.5$ at $r=r_b$.

Although the azimuthal bunching of the electrons is relatively small for times up to 4 ns, by $t\sim 6$ ns the system begins to enter a nonlinear regime characterized by spoke formation (Chan *et al.*, 1990). Highly developed spokes are evident in Fig. 25(b), which shows density contour plots at $t=8$ ns for the choice of system parameters $B_f=7.2$ kG, $V_m=350$ kV, and $t_0=4$ ns (similar to the conditions in Figs. 22 and 24 and the maximum power simulation point in Fig. 23). As the system evolves, the spokes rotate as coherent nonlinear structures in the azimuthal direction for many circulation periods around the magnetron. In addition, by $t=7$ ns, there is current flow from the cathode to the anode. At saturation, which occurs at $t\simeq 10$ ns, the time-averaged diode current per unit axial length is $I_D\simeq 100$ kA/m, and the amplitude of the integrated rf field profile $\int_a^b dr\,\delta E_r(r,\theta,t)$ is comparable to the diode voltage $V_D\simeq V_m=350$ kV.

To summarize, with regard to the dependence of rf power on magnetic field, the simulation results (Chan *et al.*, 1990) are in very good agreement with the experiment (Palevsky and Bekefi, 1979) within a constant scale factor. Moreover, in terms of rf power output, the simulations confirm that the $A6$ magnetron oscillates with dominant excitations in the π and 2π modes. In the preoscillation regime, even under the condition of space-charge-limited emission, it is found that the electron flow differs substantially from Brillouin flow conditions. In the nonlinear regime, the saturation mechanism is dominated by the formation of a large-amplitude spoke structure in the circulating electron density. As a general conclusion, based on the results presented here, it is expected that computer simulations can be used as an effective tool for developing a fundamental understanding of the large-amplitude spoke dynamics and saturation in magnetrons, as well as for experimental magnetron design.

VI. LARGE-AMPLITUDE COHERENT STRUCTURES IN ROTATING NON-NEUTRAL PLASMA

One of the most ubiquitous properties of low-density non-neutral plasma initially subject to the diocotron instability (MacFarlane and Hay, 1950; Buneman, 1957; Levy, 1965; Davidson, 1990) is the development of long-lived, rotating vortex structures during the nonlinear evolution of the system (Prasad and Malmberg, 1986; Davidson *et al.*, 1990). This has been observed experimentally in annular electron layers (Kyhl and Webster, 1956; Pierce, 1956), in intense propagating annular electron beams (Kapetanakos *et al.*, 1973), in non-neutral plasma columns with a central conductor (Rosenthal, Dimonte, and Wong, 1987; Rosenthal and Wong, 1990) and without a central conductor (Malmberg *et al.*, 1988; Driscoll *et al.*, 1989; Fine, Driscoll, and Malmberg, 1989), and in computer simulation studies (Rosenthal and Wong, 1990). The fact that long-lived coherent structures exist in these systems for many rotation periods and thousands of cyclotron periods suggests the existence of large-amplitude solutions that are stationary in the rotating frame. In this section, use is made of a cold-fluid guiding-center model (Sec. VI.A) to investigate the properties of stationary coherent structures in a rotating non-neutral plasma column (Sec. VI.B). Particular examples of large-amplitude $l=1$ and $l=2$ vortex structures are then presented (Sec. VI.C).

A. Nonrelativistic guiding-center model

We consider a low-density non-neutral electron plasma in cylindrical geometry with

$$\frac{\omega_{pe}^2}{\omega_{ce}^2}=\frac{4\pi n_e(\mathbf{x},t)m_e c^2}{B_0^2}\ll 1\ . \tag{6.1}$$

The electrons are confined radially by a uniform axial magnetic field $B_0\hat{\mathbf{e}}_z$, and cylindrical conducting walls are located at $r=a$ and $r=b$ (Fig. 15). The case in which the central conductor is absent is treated by setting $a=0$. In the present analysis, a cold-fluid guiding-center model is adopted in which electron inertial effects are neglected ($m_e\to 0$), and the motion of a strongly magnetized electron fluid element is determined from

$$0=-en_e(\mathbf{x},t)\left[\mathbf{E}(\mathbf{x},t)+\frac{1}{c}\mathbf{V}_e(\mathbf{x},t)\times B_0\hat{\mathbf{e}}_z\right]\ . \tag{6.2}$$

In the electrostatic approximation, $\mathbf{E}(\mathbf{x},t)=-\nabla\phi(\mathbf{x},t)$. Therefore Eq. (6.2) gives

$$\mathbf{V}_e(x,t)=-(c/B_0)\nabla\phi(\mathbf{x},t)\times\hat{\mathbf{e}}_z \tag{6.3}$$

for the perpendicular motion. In cylindrical geometry, Eq. (6.3) reduces to

$$V_{re}(r,\theta,t)=-\frac{c}{B_0 r}\frac{\partial}{\partial\theta}\phi(r,\theta,t)\ , \tag{6.4}$$

$$V_{\theta e}(r,\theta,t)=\frac{c}{B_0}\frac{\partial}{\partial r}\phi(r,\theta,t)\ , \tag{6.5}$$

where $\partial/\partial z=0$ is assumed. Because $\nabla\cdot\mathbf{V}_e=0$ follows from Eq. (6.3), the continuity equation can be expressed as

$$\left[\frac{\partial}{\partial t}-\frac{c}{B_0 r}\frac{\partial\phi}{\partial\theta}\frac{\partial}{\partial r}+\frac{c}{B_0 r}\frac{\partial\phi}{\partial r}\frac{\partial}{\partial\theta}\right]n_e(r,\theta,t)=0\ . \tag{6.6}$$

Of course, Eq. (6.6) must be supplemented by Poisson's equation

$$\left[\frac{1}{r}\frac{\partial}{\partial r}r\frac{\partial}{\partial r}+\frac{1}{r^2}\frac{\partial^2}{\partial\theta^2}\right]\phi(r,\theta,t)=4\pi e n_e(r,\theta,t)\ , \tag{6.7}$$

which relates self-consistently the electrostatic potential $\phi(r,\theta,t)$ to the electron density $n_e(r,\theta,t)$.

Equations (6.6) and (6.7) constitute a fully nonlinear description of the evolution of the system in the cold-fluid guiding-center approximation with $m_e\to 0$. Although the ratio $\omega_{pe}^2/\omega_{ce}^2=4\pi n_e m_e c^2/B_0^2$ approaches zero in the limit of zero electron mass, the effective diocotron frequency defined by $\omega_D=\omega_{pe}^2/\omega_{ce}=4\pi n_e ec/B_0$ remains finite as $m_e\to 0$. Assuming that the cylinders at $r=a$ and $r=b$ are perfect conductors, it is required that

$$E_\theta(r,\theta,t)=-\frac{1}{r}\frac{\partial}{\partial\theta}\phi(r,\theta,t)=0\ ,$$

$$\text{at } r=a \text{ and } r=b\ , \tag{6.8}$$

which corresponds to zero tangential electric field at the conducting walls. Making use of $V_{re}(r,\theta,t)=-(c/B_0 r)(\partial/\partial\theta)\phi(r,\theta,t)$, it follows from Eq. (6.4) and (6.8) that

$$V_{re}(r,\theta,t)=0\ ,\quad \text{at } r=a \text{ and } r=b\ , \tag{6.9}$$

which corresponds to zero radial flow of the electron fluid at $r=a$ and $r=b$.

The nonlinear equations (6.6) and (6.7) possess certain global conservation constraints that provide important insights regarding the nonlinear evolution of the system (Davidson, 1984). In particular, it is convenient to introduce the density-weighted mean-square radius of guiding-center locations, defined by

$$U_r=\int_a^b dr\, r\int_0^{2\pi}d\theta\, r^2 n_e(r,\theta,t)\ , \tag{6.10}$$

and the generalized entropy, defined by

$$U_G=\int_a^b dr\, r\int_0^{2\pi}d\theta\, G(n_e)\ . \tag{6.11}$$

Here, $G(n_e)$ is a smooth, differentiable function with $G(n_e\to 0)=0$. Making use of Eqs. (6.6) and (6.7) and the boundary conditions in Eq. (6.8), we can readily show that

$$\frac{d}{dt}U_r=0 \tag{6.12}$$

and

$$\frac{d}{dt}U_G=0\ . \tag{6.13}$$

That is, $U_r=$const and $U_G=$const are globally conserved quantities no matter how complicated the nonlinear evolution of the system described by Eqs. (6.6) and (6.7). In this regard, note that $U_r=$const is a statement of the conservation of canonical angular momentum, $\int d^2x(m_e r V_{\theta e}-eB_0 r^2/2c)n_e=$const, in the limit of zero electron mass ($m_e\to 0$).

Not only are Eqs. (6.12) and (6.13) useful conservation relations for describing the nonlinear evolution of the system, these constraint conditions can also be used to derive a sufficient condition for azimuthally symmetric equilibria $n_e^0(r)$ to be stable to small-amplitude perturbations $\delta n_e(r,\theta,t)$. In particular, for monotonically decreasing profiles with

$$\frac{1}{r}\frac{\partial}{\partial r}n_e^0(r)\le 0,\quad \text{for } a\le r\le b\ , \tag{6.14}$$

it can be shown that the density perturbation $\delta_{n_e}(r,\theta,t)$ cannot grow without bound, and the system is linearly stable (Davidson, 1984). That is, Eq. (6.14) is a *sufficient condition for stability* to small-amplitude perturbations in the context of the cold-fluid guiding-center model based on Eqs. (6.6) and (6.7). Therefore a *necessary condition for instability* is that the density profile $n_e^0(r)$ have a maximum at some radius $r=r_M$ intermediate between $r=a$ and $r=b$. An example of a profile subject to the diocotron instability (Levy, 1965) is a sufficiently thin annular

electron layer (see Fig. 10 and Sec. III.D) in which the inner and outer radii of the layer (at $r=r_b^-$ and $r=r_b^+$, say), are not in contact with the conductors at $r=a$ and $r=b$. A smooth density profile $n_e^0(r)$ with a sufficiently large density depression $n_e^0(r=a)/n_e^0(r=r_M)<1$ is also subject to the diocotron instability (Briggs, Daugherty, and Levy, 1970; Davidson, 1985a, 1985b).

B. Nonlinear stationary structures in the rotating frame

A thorough review of the linear properties of the diocotron instability has been presented by Davidson (1990) and will not be repreated here. Rather, we focus on the application of Eqs. (6.6) and (6.7) to describe large-amplitude rotating structures in non-neutral plasma. As indicated earlier, one of the most ubiquitous properties of non-neutral plasma initially subject to the diocotron instability is the development of long-lived vortex structures during the nonlinear evolution of the system. This has been observed experimentally in annular electron layers, intense propagating annular electron beams, non-neutral plasma columns with and without central conductors, and in computer simulation studies. The fact that long-lived coherent structures exist in these systems for many rotation periods and thousands of cyclotron periods suggests that the nonlinear equations (6.6) and (6.7) support large-amplitude solutions that are stationary in the rotating frame.

To investigate this possibility, we look for solutions to Eqs. (6.6) and (6.7) that depend on θ and t solely through the linear combination $\theta-\omega_r t$, where $\omega_r=$const is the angular rotation velocity of the disturbance (Davidson *et al.*, 1990). In particular, we introduce the coordinate transformation

$$\theta'=\theta-\omega_r t \ , \quad r'=r \ , \quad t'=t \ . \tag{6.15}$$

For stationary solutions $n_e(r',\theta')$ and $\phi(r',\theta')$ with $\partial/\partial t'=0$, the continuity and Poisson equations (6.6) and (6.7) can be expressed in the rotating frame as

$$\left[-\omega_r+\frac{c}{B_0 r'}\frac{\partial\phi}{\partial r'}\right]\frac{\partial n_e}{\partial\theta'}-\frac{c}{B_0 r'}\frac{\partial\phi}{\partial\theta'}\frac{\partial n_e}{\partial r'}=0 \tag{6.16}$$

and

$$\left[\frac{1}{r'}\frac{\partial}{\partial r'}r'\frac{\partial}{\partial r'}+\frac{1}{r'^2}\frac{\partial^2}{\partial\theta'^2}\right]\phi=4\pi e n_e \ . \tag{6.17}$$

It is convenient to introduce the stream function $\psi(r',\theta')$ defined by

$$\psi(r',\theta')=\frac{c}{B_0}\phi(r',\theta')-\frac{1}{2}\omega_r r'^2 \ . \tag{6.18}$$

Equations (6.16) and (6.17) then become

$$\frac{\partial\psi}{\partial r'}\frac{\partial n_e}{\partial\theta'}-\frac{\partial\psi}{\partial\theta'}\frac{\partial n_e}{\partial r'}=0 \ , \tag{6.19}$$

$$\left[\frac{1}{r'}\frac{\partial}{\partial r'}r'\frac{\partial}{\partial r'}+\frac{1}{r'^2}\frac{\partial^2}{\partial\theta'^2}\right]\psi=\frac{4\pi ec}{B_0}n_e-2\omega_r \ . \tag{6.20}$$

Note that introducing the term $-\omega_r r'^2/2$ in the definition of the stream function $\psi(r',\theta')$ in Eq. (6.18) is equivalent to reducing the density by a constant amount $(B_0/2\pi ec)\omega_r$ in Poisson's equation (6.20).

The general stationary solution to the continuity equation (6.19) in the rotating frame is

$$n_e(r',\theta')=n_e[\psi(r',\theta')] \ , \tag{6.21}$$

where $n_e(\psi)$ is a (yet unspecified) function of ψ. Substituting Eq. (6.21) into (6.20) then gives

$$\left[\frac{1}{r'}\frac{\partial}{\partial r'}r'\frac{\partial}{\partial r'}+\frac{1}{r'^2}\frac{\partial^2}{\partial\theta'^2}\right]\psi=\frac{4\pi ec}{B_0}n_e(\psi)-2\omega_r \ . \tag{6.22}$$

It is evident from Eq. (6.22) that there is considerable latitude in determining stationary solutions that depend on both r' and θ' in the rotating frame. Once the functional form of $n_e(\psi)$ is specified, then Eq. (6.22) is solved numerically or analytically, as appropriate, for the stream function $\psi(r',\theta')=c\phi(r',\theta')/B_0-\omega_r r'^2/2$. The boundary conditions consistent with zero tangential electric field at the perfectly conducting walls in Fig. 15 are given by [see Eq. (6.8)]

$$\left[\frac{\partial}{\partial\theta'}\psi(r',\theta)\right]_{r'=a}=0=\left[\frac{\partial}{\partial\theta'}\psi(r',\theta')\right]_{r'=b} \ . \tag{6.23}$$

In addition, it is assumed that the inner and outer conductors are at a constant potential difference corresponding to $\phi(r'=a,\theta)=0$ and $\phi(r'=b,\theta)=V$, or equivalently,

$$\psi(r'=a,\theta')=-\tfrac{1}{2}\omega_r a^2 \ , \quad \psi(r'=b,\theta')=cV/B_0-\tfrac{1}{2}\omega_r b^2 \ , \tag{6.24}$$

where V is the voltage difference.

C. Examples of large-amplitude vortex solutions

Depending on the choice of $n_e(\psi)$, there is considerable latitude in determining stationary solutions to Eq. (6.22) that depend on both r' and θ' in the rotating frame. In this section, we consider a simple example that is analytically tractable and corresponds to a large-amplitude vortex solution. In particular, it is assumed that $n_e(\psi)$ is specified by the linear function

$$n_e(\psi)=\hat{n}_e(C_0+C_1\psi) \ , \tag{6.25}$$

where C_0 and C_1 are constants, and $\hat{n}_e=$const is a measure of the characteristic electron density in the interval $a\le r\le b$. By introducing the effective diocotron frequen-

cy ω_D = const defined by

$$\omega_D = 4\pi \hat{n}_e e c / B_0 \ , \tag{6.26}$$

Poisson's equation (6.22) becomes

$$\left[\frac{1}{r'} \frac{\partial}{\partial r'} r' \frac{\partial}{\partial r'} + \frac{1}{r'^2} \frac{\partial^2}{\partial \theta'^2} \right] \psi = \omega_D C_0 - 2\omega_r + \omega_D C_1 \psi \ . \tag{6.27}$$

The (linear) differential equation (6.27) can be solved exactly for $\psi(r',\theta')$ subject to the boundary conditions in Eqs. (6.23) and (6.24).

We examine solutions to Eq. (6.27) of the form

$$\psi(r',\theta') = \psi_0(r') + \psi_l(r') \cos(l\theta') \ , \tag{6.28}$$

where $l \neq 0$ is an integer. Substituting Eq. (6.28) into Eq. (6.27) then gives

$$\left[\frac{1}{r'} \frac{\partial}{\partial r'} r' \frac{\partial}{\partial r'} + k^2 \right] \psi_0(r') = \omega_D C_0 - 2\omega_r \tag{6.29}$$

and

$$\left[\frac{1}{r'} \frac{\partial}{\partial r'} r' \frac{\partial}{\partial r'} + k^2 - \frac{l^2}{r'^2} \right] \psi_l(r') = 0 \ , \tag{6.30}$$

where $k^2 \equiv -\omega_D C_1 > 0$ is assumed. The solutions to Eqs. (6.29) and (6.30) in the interval $a \leq r \leq b$ are linear combinations of $J_0(kr')$ and $Y_0(kr')$, and $J_l(kr')$ and $Y_l(kr')$, respectively. Here, $J_l(x)$ is the Bessel function of the first kind of order l and $Y_l(x)$ is the Neumann function of order l. For present purposes, we also consider the class of solutions in which the electron density is equal to zero at the outer conductor, i.e., $n_e(r'=b,\theta') = \hat{n}_e[C_0 + C_1\psi(r'=b,\theta')] = 0$. Making use of $\psi(r'=b,\theta') = cV/B_0 - \omega_r b^2/2$ [Eq. (6.24)], we can use this condition to relate the constants C_0 and $C_1 = -k^2/\omega_D$ by

$$C_0 = -C_1 \left[\frac{cV}{B_0} - \frac{1}{2}\omega_r b^2 \right] \ . \tag{6.31}$$

We solve Eqs. (6.29) and (6.30) for $\psi_0(r')$ and $\psi_l(r')$ and substitute into Eq. (6.28). Enforcing the boundary conditions in Eqs. (6.23) and (6.24) then gives the desired solutions for the electrostatic potential $c\phi(r',\theta')/B_0 = \psi(r',\theta') + \omega_r r'^2/2$ and the electron density $n_e(r',\theta') = \hat{n}_e[C_0 + C_1\psi(r',\theta')]$. In laboratory-frame variables (r,θ,t), some straightforward algebra gives (Davidson *et al.*, 1990)

$$\frac{c}{B_0}\phi(r,\theta,t) = \left[\frac{cV}{B_0} - \frac{\omega_r}{2}\left[b^2 - r^2 + \frac{4}{k^2} \right] \right] - \left[\frac{cV}{B_0} - \frac{\omega_r}{2}\left[b^2 - a^2 + \frac{4}{k^2} \right] \right] \left[\frac{J_0(kb)N_0(kr) - N_0(kb)J_0(kr)}{J_0(kb)N_0(ka) - N_0(kb)J_0(ka)} \right]$$
$$+ \frac{2\omega_r}{k^2} \left[\frac{N_0(ka)J_0(kr) - J_0(ka)N_0(kr)}{N_0(ka)J_0(kb) - J_0(ka)N_0(kb)} \right] + a_l \left[J_l(kr) - \frac{J_l(ka)}{N_l(ka)} N_l(kr) \right] \cos[l(\theta - \omega_r t)] \tag{6.32}$$

and

$$n_e(r,\theta,t) = \hat{n}_e \frac{2\omega_r}{\omega_D} \left[1 - \frac{N_0(ka)J_0(kr) - J_0(ka)N_0(kr)}{N_0(ka)J_0(kb) - J_0(ka)N_0(kb)} \right]$$
$$+ \hat{n}_e \frac{k^2}{\omega_D} \left[\frac{cV}{B_0} - \frac{\omega_r}{2}\left[b^2 - a^2 + \frac{4}{k^2} \right] \right] \left[\frac{J_0(kb)N_0(kr) - N_0(kb)J_0(kr)}{J_0(kb)N_0(ka) - N_0(kb)J_0(ka)} \right]$$
$$- \hat{n}_e \frac{k^2 a_l}{\omega_D} \left[J_l(kr) - \frac{J_l(ka)}{N_l(ka)} N_l(kr) \right] \cos[l(\theta - \omega_r t)] \ . \tag{6.33}$$

Here, a_l is a constant amplitude factor, and the parameter k is chosen to satisfy

$$J_l(kb)N_l(ka) - J_l(ka)N_l(kb) = 0 \ . \tag{6.34}$$

From Eqs. (6.32) and (6.34) it follows trivially that the electrostatic potential $\phi(r,\theta,t)$ satisfies the boundary conditions $[\phi]_{r=a} = 0$, $[\phi]_{r=b} = V$, $[\partial\phi/\partial\theta]_{r=a} = 0$, and $[\partial\phi/\partial\theta]_{r=b} = 0$, consistent with Eqs. (6.23) and (6.24). In addition, from Eqs. (6.33) and (6.34), the electron density is equal to zero at the outer conductor in Fig. 15, i.e., $n_e(r=b,\theta,t) = 0$. On the other hand, evaluating Eq. (6.33) at $r=a$ gives the steady value $n_e(r=a,\theta,t) = n_e(a)$, where

$$n_e(a) \equiv \hat{n}_e \frac{k^2}{\omega_D} \left[\frac{cV}{B_0} - \frac{\omega_r}{2}(b^2 - a^2) \right] \ . \tag{6.35}$$

Evidently, Eqs. (6.32) and (6.33) describe structured potential and density profiles that rotate azimuthally about the z axis in Fig. 15 with angular velocity ω_r = const. Note that the profiles are stationary (independent of time) in the rotating frame. Furthermore, for specified integer l, the profiles described by Eqs. (6.32) and (6.33) have azimuthal periodicity $2\pi/l$ in the rotating

frame. In particular, insofar as Eqs. (6.32) and (6.33) represent a coherent vortex structure, $l=1$ corresponds to one vortex, $l=2$ corresponds to two vortices, etc. As a further important point, for the solution in Eq. (6.33) to be physically acceptable, it is required that the electron density profile satisfy

$$n_e(r,\theta,t)\geq 0 \tag{6.36}$$

in the entire region $a\leq r\leq b$ and $0\leq\theta\leq 2\pi$ between the conducting cylinders in Fig. 15. This places restrictions on the allowed values of the dimensionless parameters kb, ω_r/ω_D, and $k^2cV/\omega_D B_0$, and the dimensionless amplitude k^2a_l/ω_D of the oscillatory (θ-dependent) term in Eq. (6.33).

Figures 26–29 illustrate properties of the solutions for ϕ and n_e in Eqs. (6.32) and (6.33) for disturbances with azimuthal mode number $l=1$ (Figs. 26 and 27) and $l=2$ (Figs. 28 and 29). Because the structures in Eqs. (6.32) and (6.33) rotate azimuthally about the z axis with angular velocity $\omega_r=$const, the information in Figs. 26–29 is displayed at time $t=0$ without loss of generality.

The choice of system parameters in Figs. 26 and 27 corresponds to $l=1$ and

$$\frac{a}{b}=0.3,\ kb=4.7058,\ \frac{\omega_r}{\omega_D}=0.2,$$
$$\frac{k^2cV}{\omega_D B_0}=2.2144,\ \frac{k^2a_l}{\omega_D}=4.4289. \tag{6.37}$$

Here, $kb=4.7058$ is the first zero of Eq. (6.34) for $l=1$ and $a/b=0.3$. Figure 26 shows plots of the equipotential contours, $\phi(r,\theta,t=0)=$const, calculated from Eqs. (6.32) and (6.37). From Eqs. (6.3)–(6.5), the flow velocity $\mathbf{V}_e=-(c/B_0)\nabla\phi\times\hat{\mathbf{e}}_z$ is tangential to the contours $\phi=$const. Therefore the local flow velocity circulates in the direction indicated by the arrows in Fig. 26. Evidently, the structure centered around $\theta=\pi$ in Fig. 26 corresponds to a large-amplitude vortex localized between $r=a$ and $r=b$. The corresponding radial dependence of the density profile $n_e(r,\theta,t=0)$ calculated from Eqs. (6.33) and (6.37) is illustrated in Fig. 27 for $\theta=0$, $\theta=\pi/2$ (or $\theta=3\pi/2$), and $\theta=\pi$. It is evident from Fig. 27 that the density compression is large at the center of the vortex at $\theta=\pi$ (compare with the density profiles at $\theta=0$ and $\pi/2$ in Fig. 27). Note also from Eq. (6.33) that the

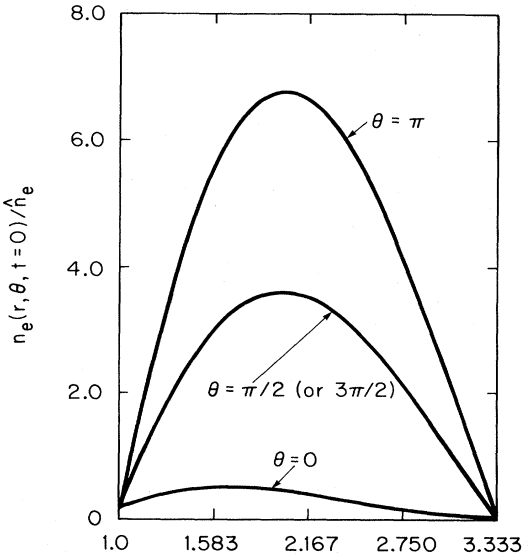

FIG. 27. Plots vs r/a of the density profile $n_e(r,\theta,t=0)$ calculated from Eq. (6.33) for $l=1$ and values of θ corresponding to $\theta=0$, $\theta=\pi/2$ (or $\theta=3\pi/2$), and $\theta=\pi$. The choice of system parameters is the same as in Eq. (6.37) and Fig. 26.

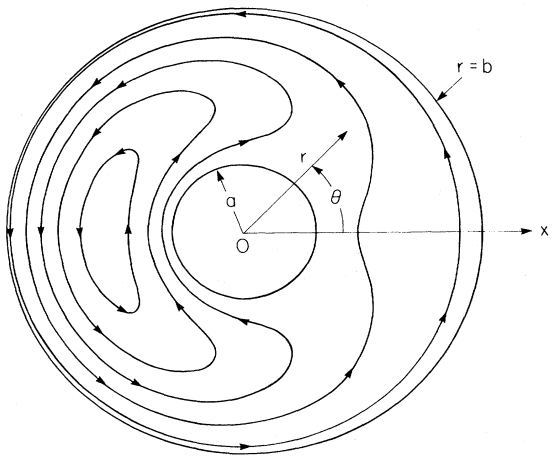

FIG. 26. Plots of the equipotential contours $\phi(r,\theta,t=0)=$const calculated from Eq. (6.32) for $l=1$ and the choice of system parameters in Eq. (6.37). The arrows indicate the direction of the circulating electron flow $\mathbf{V}_e=-(c/B_0)\nabla\phi\times\hat{\mathbf{e}}_z$.

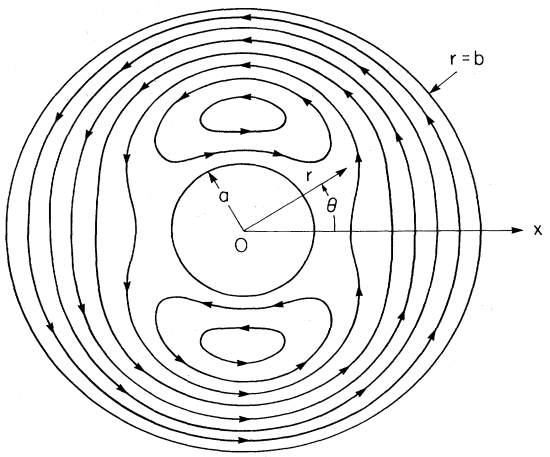

FIG. 28. Plots of the equipotential contours $\phi(r,\theta,t=0)=$const calculated from Eq. (6.32) for $l=2$ and the choice of system parameters in Eq. (6.38). The arrows indicate the direction of the circulating electron flow $\mathbf{V}_e=-(c/B_0)\nabla\phi\times\hat{\mathbf{e}}_z$.

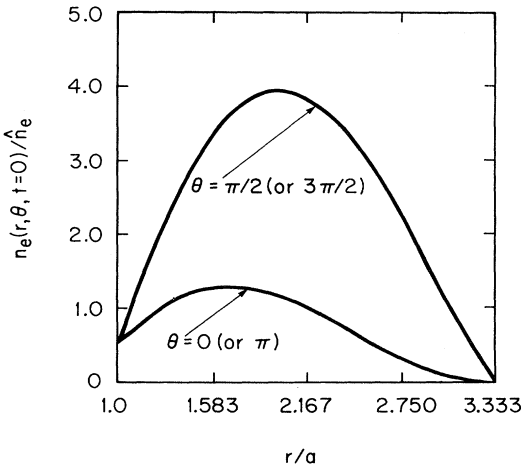

FIG. 29. Plots vs r/a of the density profile $n_e(r,\theta,t=0)$ calculated from Eq. (6.33) for $l=2$ and values of θ corresponding to $\theta=0$ (or $\theta=\pi$) and $\theta=\pi/2$ (or $\theta=3\pi/2$). The choice of system parameters is the same as in Eq. (6.38) and Fig. 28.

profile for $n_e(r,\theta=\pi/2,\ t=0)$ plotted in Fig. 27 is the same as the azimuthally averaged density profile $\langle n_e\rangle(r,t=0)=(2\pi)^{-1}\int_0^{2\pi}d\theta\, n_e(r,\theta,t=0)$.

The choice of system parameters in Figs. 28 and 29 corresponds to $l=2$ and

$$\frac{a}{b}=0.3,\ kb=5.4702,\ \frac{\omega_r}{\omega_D}=0.4\ ,\qquad \frac{k^2cV}{\omega_D B_0}=5.9847,\ \frac{k^2a_l}{\omega_D}=2.9923\ . \tag{6.38}$$

Here, $kb=5.4702$ is the first zero of Eq. (6.34) for $l=2$ and $a/b=0.3$. Figure 28 shows plots of the equipotential contours, $\phi(r,\theta,t=0)=$const, calculated from Eqs. (6.32) and (6.38). The direction of the local flow velocity is indicated by the arrows in Fig. 28. Evidently, for $l=2$, there are two large-amplitude vortices centered around $\theta=\pi/2$ and $\theta=3\pi/2$. Moreover, the density compression is large at the center of vortices. This is evident from Fig. 29, which shows the radial dependence of the density profile $n_e(r,\theta,t=0)$ calculated from Eqs. (6.33) and (6.38) for $\theta=0$ (or $\theta=\pi$) and $\theta=\pi/2$ (or $\theta=3\pi/2$).

To summarize, Figs. 26–29 and the analysis in Secs. VI.B and VI.C demonstrate that a simple cold-fluid guiding-center model of a low-density non-neutral plasma supports large-amplitude vortex solutions that are stationary in the rotating frame. What is most striking is that the coherent structures described by Eqs. (6.32) and (6.33) are very rich in detail for the case in which $n_e(\psi)$ is assumed to have a simple linear dependence on ψ with $n_e(\psi)=\hat{n}_e(C_0+C_1\psi)$. Even more structure would be present in the nonlinear case where a quadratic term is included with $n_e(\psi)=\hat{n}_e(C_0+C_1\psi+C_2\psi^2)$. Finally, it should be emphasized that the present analysis addresses only the existence of coherent structures that are stationary in the rotating frame. The question of accessibility of such solutions from prescribed initial conditions $n_e(r,\theta,t=0)$ is not addressed by the present analysis, although the constants $\omega_r/\omega_D, k^2a_l/\omega_D$, etc., occurring in Eqs. (6.32) and (6.33), can be related to the initial conditions by the global conservation constraints in Eqs. (6.10) and (6.11). In addition, the stability of such large-amplitude structures requires an analysis of the evolution of small-amplitude perturbations, δn_e and $\delta\phi$, about the solutions in Eqs. (6.32) and (6.33).

VII. CONCLUSIONS

This paper has reviewed the equilibrium and stability properties of intense non-neutral electron flow in crossed electric and magnetic fields. Following a description of equilibrium properties for magnetically insulated electron flow in planar geometry (Sec. II), we investigated extraordinary-mode stability properties for relativistic non-neutral electron flow between planar conductors, placing particular emphasis on the magnetron and diocotron instabilities (Sec. III). Detailed stability behavior was found to exhibit a sensitive dependence on the self-field intensity (as measured by $s_e=\gamma_e^0\omega_{pe}^2/\omega_{ce}^2$) as well as on the shape of the equilibrium profiles. The influence of cylindrical effects (such as the centrifugal and Coriolis accelerations of an electron fluid element) on stability behavior was then investigated for rotating electron flow in cylindrical geometry (Sec. IV). Finally, the properties of large-amplitude coherent structures were investigated, including particle-in-cell computer simulations of dense ($s_e\sim 1$) electron flow in relativistic magnetrons, which show large-amplitude spoke formation in the circulating density (Sec. V), and application of a cold-fluid guiding-center model to investigate large-amplitude vortex structures in low-density ($s_e\ll 1$) non-neutral plasma (Sec. VI). The accessibility and stability of such stationary structures (in the rotating frame) remain important topics for future investigation.

ACKNOWLEDGMENTS

This research was supported in part by the Naval Research Laboratory's Plasma Physics Division, the Department of Energy's High Energy Physics Division, the Office of Naval Research, and the National Science Foundation.

REFERENCES

Antonsen, T. M., Jr., and C. L. Chang, 1989, Phys. Fluids B **1**, 1728.

Antonsen, T. M., Jr., W. H. Miner, E. Ott, and A. T. Drobot, 1984, Phys. Fluids **27**, 1257.

Antonsen, T. M., Jr., and E. Ott, 1976, Phys. Fluids **19**, 52.

Bekefi, G., and T. J. Orzechowski, 1976, Phys. Rev. Lett. **37**, 379.

Benford, J., 1987, in *High-Power Microwave Sources,* edited by V. Granatstein and I. Alexeff (Artech House, Boston), p. 351.
Benford, J., H. M. Sze, W. Woo, R. R. Smith, and B. Harteneck, 1989, Phys. Rev. Lett. **62**, 969.
Birdsall, C. K., and W. B. Bridges, 1966, *Electron Dynamics of Diode Regions* (Academic, New York).
Bogoliubov, N. N., 1946, *Problems of a Dynamical Theory in Statistical Physics* (State Technical, Moscow).
Briggs, R. J., J. D. Daugherty, and R. H. Levy, 1970, Phys. Fluids **13**, 421.
Brillouin, L., 1945, Phys. Rev. **67**, 260.
Brillouin, L., 1951, Adv. Electron. **3**, 85.
Buneman, O., 1957, J. Electron. Control **3**, 507.
Buneman, O., 1961, in *Crossed-Field Microwave Devices,* edited by E. Okress (Academic, New York), Vol. 1, p. 209.
Buneman, O., R. H. Levy, and L. M. Linson, 1966, J. Appl. Phys. **37**, 3203.
Chan, H.-W., C. Chen, and R. C. Davidson, 1990, Appl. Phys. Lett. **57**, 1271.
Chang, C. L., D. P. Chernin, A. T. Drobot, E. Ott, and T. M. Antonsen, Jr., 1986, Phys. Fluids **29**, 1258.
Chang, C. L., E. Ott, and T. M. Antonsen, Jr., 1986, Phys. Fluids **29**, 3851.
Chernin, D., and Y. Y. Lau, 1984, Phys. Fluids **27**, 2319.
Child, C. D., 1911, Phys. Rev. **32**, 492.
Collins, G. B., 1948, Ed., *Microwave Magnetrons* (McGraw-Hill, New York).
Daugherty, J. D., and R. H. Levy, 1967, Phys. Fluids **10**, 155.
Davidson, R. C., 1971, J. Plasma Phys. **6**, 229.
Davidson, R. C., 1974, *Theory of Nonneutral Plasmas* (Benjamin, Reading, MA), reissued in the Advanced Book Classics Series (Addison-Wesley, Reading, MA, 1989).
Davidson, R. C., 1984, Phys. Fluids **27**, 1804.
Davidson, R. C., 1985a, Phys. Fluids **28**, 377.
Davidson, R. C., 1985b, Phys. Fluids **28**, 1937.
Davidson, R. C., 1990, *Physics of Nonneutral Plasma* (Addison-Wesley, Reading, MA).
Davidson, R. C., H.-W. Chan, C. Chen, and S. Lund, 1990, "Large-amplitude coherent structures in nonneutral plasmas with circulating electron flow," in *AIP Conference Proceedings on Nonlinear and Relativistic Effects in Plasmas,* edited by V. Stefan (AIP, New York), in press (MIT PFC Report PFC/JA-90-4.)
Davidson, R. C., and N. A. Krall, 1969, Phys. Rev. Lett. **22**, 833.
Davidson, R. C., and N. A. Krall, 1970, Phys. Fluids **13**, 1543.
Davidson, R. C., and K. T. Tsang, 1984, Phys. Rev. A **30**, 488.
Davidson, R. C., and K. T. Tsang, 1985, Phys. Fluids **28**, 1169.
Davidson, R. C., and K. T. Tsang, 1986, Phys. Fluids **29**, 3832.
Davidson, R. C., K. T. Tsang, and J. A. Swegle, 1984, Phys. Fluids **27**, 2332.
Davidson, R. C., K. T. Tsang, and H. S. Uhm, 1985, Phys. Rev. A **32**, 1044.
Davidson, R. C., K. T. Tsang, and H. S. Uhm, 1988, Phys. Fluids **31**, 1727.
Davidson, R. C., and H. S. Uhm, 1985, Phys. Rev. A **32**, 3554.
Davidson, R. C., and H. S. Uhm, 1989a, Laser Part. Beams **7**, 55.
Davidson, R. C., and H. S. Uhm, 1989b, Laser Part. Beams **7**, 85.
Desjarlais, M. P., 1987, Phys. Rev. Lett. **59**, 2295.
Desjarlais, M. P., 1989, Phys. Fluids B **1**, 1709.
Dreike, P. L., C. Eichenberger, S. Humphries, Jr., and R. N. Sudan, 1976, J. Appl. Phys. **47**, 85.
Driscoll, C. F., J. H. Malmberg, K. S. Fine, R. A. Smith, and X.-P. Huang, 1989, in *Plasma Physics and Controlled Nuclear Fusion Research,* Proceedings of the Twelfth International Conference on Plasma Physics and Controlled Nuclear Fusion Research—Nice, 1988, edited by the editorial staff of the IAEA (IAEA, Vienna), Vol. 3, p. 507.
Dubin, D. H. E., and T. M. O'Neil, 1988, Phys. Rev. Lett. **60**, 511.
Fine, K. S., C. F. Driscoll, and J. H. Malmberg, 1989, Phys. Rev. Lett. **63**, 2232.
Gabrielse, G., X. Fei, K. Helmerson, S. L. Rolston, R. Tjoelker, T. A. Trainor, H. Kalinowsky, J. Haas, and W. Kells, 1986, Phys. Rev. Lett. **57**, 2504.
Gilbert, S. L., J. J. Bollinger, and D. J. Wineland, 1988, Phys. Rev. Lett. **60**, 2022.
Gleizer, I. Z., A. N. Didenko, A. S. Sulakshin, G. P. Fomenko, and V. I. Tsvetkov, 1980, Sov. Tech. Phys. Lett. **6**, 19.
Goplen, B., and J. McDonald, 1989, private communication.
Granatstein, V., and I. Alexeff, 1987, Eds., *High Power Microwave Sources* (Artech House, Boston), and references therein.
Grimes, G. C., and G. Adams, 1979, Phys. Rev. Lett. **42**, 795.
Guenther, A., and M. Kristiansen, 1987, Eds., *Advances in Pulsed Power Technology* (Plenum, New York).
Hammer, D. A., and N. Rostoker, 1970, Phys. Fluids **13**, 1831.
Hull, A. W., 1921, Phys. Rev. **18**, 31.
Humphries, S., Jr., 1986, *Principles of Charged Particle Acceleration* (Wiley, New York).
Humphries, S., Jr., J. J. Lee, and R. N. Sudan, 1974, Appl. Phys. Lett. **25**, 20.
Humphries, S., Jr., R. N. Sudan, and L. Wiley, 1976, J. Appl. Phys. **47**, 2382.
Johnson, D. J., P. L. Dreike, S. A. Slutz, R. J. Leeper, E. J. T. Burns, J. R. Freeman, T. A. Mehlhorn, and J. P. Quintenz, 1983, J. Appl. Phys. **54**, 2230.
Johnson, D. J., R. J. Leeper, W. A. Stygar, R. S. Coats, T. A. Mehlhorn, J. P. Quintenz, S. A. Slutz, and M. A. Sweeney, 1985, J. Appl. Phys. **58**, 12.
Jory, H. R., and A. W. Trivelpiece, 1969, J. Appl. Phys. **40**, 3924.
Kapetanakos, C. A., D. A. Hammer, C. Striffler, and R. C. Davidson, 1973, Phys. Rev. Lett. **30**, 1303.
Kapetanakos, C. A., and P. Sprangle, 1985, Phys. Today **38(2)**, 58.
Keefe, D., 1987, Part. Accel. **11**, 187.
Kyhl, R. L., and H. F. Webster, 1956, IRE Trans. Electron Devices **ED-3**, 172.
Landau, L. D., 1946, J. Phys. (Moscow) **10**, 25.
Langmuir, I., 1923, Phys. Rev. **21**, 419.
Lau, Y. Y., 1987, in *High-Power Microwave Sources,* edited by V. Granatstein and I. Alexeff (Artech House, Boston), p. 309.
Lau, Y. Y., and D. Chernin, 1984, Phys. Rev. Lett. **52**, 1425.
Lawson, J. D., 1988, *The Physics of Charged Particle Beams* (Clarendon, Oxford).
Lee, E. P., and J. Hovingh, 1989, Fusion Technol. **15**, 369.
Levy, R. H., 1965, Phys. Fluids **8**, 1288.
Levy, R. H., 1968a, Phys. Fluids **11**, 772.
Levy, R. H., 1968b, Phys. Fluids **11**, 920.
Lewellyn, F. B., 1941, *Electron Inertia Effects* (Cambridge University, London).
Lovelace, R. V., and E. Ott, 1974, Phys. Fluids **17**, 1263.
Lovelace, R. V., and T. F. T. Young, 1985, Phys. Fluids **28**, 2450.
MacFarlane, C. C., and H. G. Hay, 1950, Proc. Phys. Soc. Lon-

don, Sect. B **63**, 409.
Malmberg, J. H., C. F. Driscoll, B. Beck, D. L. Eggleston, J. Fajans, K. Fine, X.-P. Huang, and A. W. Hyatt, 1988, in *Non-neutral Plasma Physics,* AIP Conference Proceedings No. 175, edited by C. W. Roberson and C. F. Driscoll (AIP, New York), p. 28.
Malmberg, J. H., and T. M. O'Neil, 1977, Phys. Rev. Lett. **39**, 1333.
Marshall, T. C., 1985, *Free Electron Lasers* (Macmillan, New York).
Michael, C., 1985, Proc. Astron. Soc. Austrialia **6**, 127.
Miller, R. B., 1982, *Intense Charged Particle Beams* (Plenum, New York).
Nokonov, A. G., I. M. Roife, Yu. M. Savel'ev, and V. I. Engel'ko, 1987, Sov. Tech. Phys. Lett **32**, 50.
Okress, E., 1961, Ed., *Crossed-Field Microwave Devices* (Academic, New York), Vol. 1.
Orzechowski, T. J., and G. Bekefi, 1979, Phys. Fluids **22**, 978.
Ott, E., J. M. Antonsen, Jr., C. L. Chang, and A. T. Drobot, 1985, Phys. Fluids **28**, 1948.
Ott, E., and R. V. Lovelace, 1975, Appl. Phys. Lett. **27**, 378.
Palevsky, A., and G. Bekefi, 1979, Phys. Fluids **22**, 986.
Palevsky, A., G. Bekefi, and A. T. Drobot, 1981, J. Appl. Phys. **52**, 4938.
Palevsky, A., G. Bekefi, A. Drobot, A. Mondelli, G. Graig, K. Eppley, M. Black, M. Bollen, and R. Parker, 1981, in *High-Power Beams,* edited by H. J. Doucet and J. M. Buzzi (Ecole Polytechnique, Palaiseau, France), p. 861.
Petillo, J. J., and R. C. Davidson, 1987, Phys. Fluids **30**, 2477.
Pierce, J. R., 1956, IRE Trans. Electron Devices **ED-3**, 183.
Prasad, S. A., and J. H. Malmberg, 1986, Phys. Fluids **29**, 2196.
Roberson, C. W., and C. F. Driscoll, 1988, Eds., *Non-neutral Plasma Physics,* AIP Conference Proceedings No. 175 (AIP, New York), and papers therein.
Roberson, C. W., and P. Sprangle, 1989, Phys. Fluids B **1**, 3, and references therein.
Rosenthal, G., G. Dimonte, and A. Y. Wong, 1987, Phys. Fluids **30**, 3257.
Rosenthal, G., and A. Y. Wong, 1990, "Localized density clumps and potentials generated in a magnetized nonneutral plasma," unpublished.
Rostoker, N., 1980, Comments Plasma Phys. Controlled Fusion **6**, 91.
Slater, J., 1969, *Microwave Electronics* (Dover, New York).
Sprangle, P., and C. A. Kapetanakos, 1978, J. Appl. Phys. **49**, 1.
Sudan, R. N., and R. V. Lovelace, 1973, Phys. Rev. Lett. **31**, 1174.
Surko, C. M., M. Leventhal, W. S. Crane, A. Passner, F. Wysocki, T. J. Murphy, J. Strachan, and W. L. Rowan, 1986, Rev. Sci. Instrum. **57**, 1862.
Swegle, J., 1983, Phys. Fluids **26**, 1670.
Swegle, J., and E. Ott, 1981a, Phys. Rev. Lett. **46**, 929.
Swegle, J., and E. Ott, 1981b, Phys. Fluids **24**, 1821.
Tonks, L., and I. Langmuir, 1929, Phys. Rev. **33**, 195.
Trivelpiece, A. W., 1972, Comments Plasma Phys. Controlled Fusion **1**, 57.
Tsang, K. T., and R. C. Davidson, 1986, Phys. Rev. A **33**, 4284.
Uhm, H. S., H. C. Chen, R. A. Stark, and H. Brandt, 1989, Proc. SPIE **1061**, 170.
Uhm, H. S., and R. C. Davidson, 1985, Phys. Rev. A **31**, 2556.
VanDevender, J. P., and D. L. Cook, 1986, Science **232**, 831.
Vlasov, A. A., 1945, J. Phys. (Moscow) **9**, 25.
Yu, S. P., G. P. Kooyers, and O. Buneman, 1965, J. Appl. Phys. **36**, 2550.